

# OPTICAL PROPERTIES OF COMPOSITE POLYMER MATERIALS

By

Sajad Ghatrehsamani

A THESIS SUBMITTED TO MACQUARIE UNIVERSITY  
FOR THE DEGREE OF  
DOCTOR OF PHILOSOPHY  
DEPARTMENT OF ENGINEERING, FACULTY OF SCIENCE AND ENGINEERING  
MAY 2016





Except where acknowledged in the customary manner, the material presented in this thesis is, to the best of my knowledge, original and has not been submitted in whole or part for a degree in any university.

---

Sajad Ghatrehsamani

Dedicated to

the soul of my mother, Nasrin, who has been a wonderful mother and has shown a genuine interest in and concern for my life, my work and my well-being

and

my father and brother, whose unconditional love and encouragement allowed me to start and complete this journey.



# Acknowledgments

First and foremost, I would like to express my sincere thanks to my supervisor, Professor Graham Town, who not only supported me throughout this project but also helped me to improve myself in many aspects. It was a very precious experience to work with Professor Graham Town, and I learnt valuable academic skills from his instruction. I would also like to acknowledge my co-supervisor Dr Stuart Jackson for his support. I would like to thank Professor Ole Bang at the FOTONIK Department of the Technical University of Denmark (DTU) for inviting me to be a visiting PhD student researcher. I also thank Research Fellow Dr Christos Marcos and Dr Alessio Stefani at DTU who were very supportive of my experiments and training. I would also like to acknowledge Professor Martin Koch at Phillips University in Germany, for allowing me to work with his group, and also his PhD student Stefan Busch for his help which broadened my research experience in THz measurements and applications. I would like to acknowledge the Australian National Fabrication Facility (ANFF) at the University of Sydney node and Dr Richard Lwin for technical assistance, and the Macquarie University Microscopy unit of the Biology Department. I am grateful to Dr Keith Imrie for valuable advice and useful comments that improved the written quality of this thesis. I am also thankful to the admirable staff in the Department of Engineering for their wonderful support. I wish to acknowledge Macquarie University for awarding me the International Macquarie University Research Excellence Scholarship (iMQRES), and providing financial support to attend national and international conferences, and to do off-site research at DTU and Phillips universities during my candidature. I would like to express my appreciation to my parents and my brother for their endless love and support. Last but not least, thanks to my friends for making me feel special and being there when I needed them.



# List of Publications

## Published:

1. G. E. Town , S. Ghatrehsamani, A. Stefani, O. Bang, P. U. Jepsen, “Dispersion in THz waveguides with scaled microstructure,” in 2015 CLEO, Munich, Germany, Paper CE-P-20.
2. G. E. Town, S. Ghatrehsamani , C. Markos , O. Bang, “Strain and temperature sensitivity of beatlength in a dual-core microstructured polymer optical fiber,” in 2015 CLEO, Munich, Germany, Paper CK-P-39.
3. S. Ghatrehsamani, G. E. Town, “Modeling depolarization effects in highly scattering media,” in 2014 98th FiO, Tucson, United States, Paper FM4D.4.
4. S. Ghatrehsamani, G. E. Town, “Prediction of optical gain in PMMA/ SiO<sub>2</sub>: Er<sup>3+</sup>/Yb<sup>3+</sup> nanocomposite,” in 2014 98th FiO, Tucson, United States, Paper FW5B.6.
5. S. Ghatreh-Samani, and G. E. Town, “Synthesis and optical properties of PMMA/ Silica-MPTS nanocomposite,” in 2014 ACMM and ICONN , Adelaide, Australia, Paper 212.
6. G. E. Town, S. Ghatreh-Samani, S. Busch, M. Koch, “THz diffuser using an air-polymer composite material,” 2013 38<sup>th</sup> IRMMW-THz, Mainz, Germany, pp.1-2.
7. S. Ghatreh-Samani, G. E. Town, “Modelling optical properties of polymer nanocomposites,” in 2012 ANN, Melbourne, Australia, Paper PS08.
8. S. Ghatreh-Samani, G. E. Town, “Transmittance and effective refractive index of polymer nanocomposites,” in 2012 20<sup>th</sup> AIP, Sydney, Australia, Paper 16.

**Submitted:**

1. S. Shashidharan, S. Ghatrehsamani, and G. E. Town, "Dual-core POF and its application in pressure sensing, " 2015 40<sup>th</sup> Australian Conference on Optical Fibre Technology, Adelaide, Australia.

**In Preparation:**

1. S. Ghatrehsamani, S. Busch, G. E. Town, S. Shashidharan, M. Koch, "Study of angle- and frequency- dependent THz scattering in 2-D polycarbonate microstructures," IEEE Transactions on Terahertz Science and Technology.
2. S. Ghatrehsamani, S. Busch, G. E. Town, S. Shashidharan, and M. Koch, "THz scattering in gold coated silica-polyethylene composite material," IEEE Transactions on Terahertz Science and Technology.
3. S. Ghatrehsamani, G. E. Town, S. Shashidharan, C. Markos, and O. Bang, "Strain and temperature sensing characteristics of a dual-core microstructured polymer optical fiber," Optics Letters.
4. S. Ghatrehsamani, G. E. Town, S. Shashidharan, A. Stefani, S. Busch, O. Bang, and P. U. Jepsen, "Flattened dispersion in tapered and scaled polymer THz waveguides," Optics Letters.
5. S. Ghatrehsamani and G. E. Town, "Propagation of polarized light in composite materials," Journal of the Optical Society of America A.
6. S. Ghatrehsamani and G. E. Town, "Optical gain in  $\text{P}_2\text{O}_5:\text{Er}^{3+}/\text{Yb}^{3+}$  nanoparticle-doped polymer-based waveguides," Journal of Lightwave Technology.
7. S. Ghatrehsamani, G. E. Town, S. Shashidharan, "Microstructured and nanostructured optical sensing platforms based on coupled waveguide structures," Journal of Sensors.
8. S. Ghatrehsamani and G. E. Town, "Optical and thermal properties of  $\text{SiO}_2/\text{PMMA}$  nanocomposites,".
9. S. Ghatrehsamani, G. E. Town, "Study of THz scattering in an air-polymer composite material,".
10. S. Ghatrehsamani, G. E. Town, "Controlling polarization of multiply scattered light through composite materials,".

11. S. Ghatrehsamani, G. E. Town, “Optimization of Optical Gain in PMMA/P<sub>2</sub>O<sub>5</sub>:Er<sup>3+</sup>/Yb<sup>3+</sup> Nanocomposites,”.



# Abstract

Polymer composites are materials in which nano- and/or micro-sized particles of inorganic materials (e.g. semiconductors, metal, air) are dispersed in a polymer host. Such materials are of interest to combine the optical properties of the inorganic materials with the easy processing of polymers, hence extending the functionality and properties of polymer-based optical devices. The main challenge with polymer composites is their optical loss, resulting from scattering caused by the inclusions and often also absorption due to the host and/or particles. Polymer composite materials can be either weakly or highly scattering media, and can be useful from the optical to the terahertz regimes, depending upon the size and the refractive index of inclusions and the host polymer. Although scattering is usually considered an unwanted property, it is possible to overcome and/or make use of the scattering in polymer composite materials designed for specific applications. For example, it is shown through numerical simulation and experiments that weakly scattering nanocomposites with optical gain are feasible, and highly scattering media may be useful as a THz diffuser and/or depolariser.

Modern optical telecommunication systems operate around 1.5 microns, however the loss in the polymer at these wavelengths is significantly larger than in glass-based devices. The question therefore arises how one might reduce the optical losses in polymers at telecommunication wavelengths, e.g. by introducing optical gain. A detailed model of optical gain in polymers containing highly doped glass nanoparticles was developed, taking into account the effects of scattering at both pump and signal wavelengths, and used to optimise the material parameters. It is shown that optical gain is feasible at 1.55  $\mu\text{m}$  in a poly(methyl methacrylate) host containing 10% by volume of erbium-ytterbium-doped phosphate glass nanoparticles 100 nm in diameter when pumped at 980 nm with intensity 1 mW/ $\mu\text{m}^2$ .

It is often necessary in communication and sensing systems to collect or radiate energy over a wide range of directions, though most coherent sources are highly directive. A numerical model was developed based on a Monte-Carlo algorithm which

was extended to include the effects of both losses and boundaries on the propagation of electromagnetic (EM) waves through composite materials. Moreover, we fabricated a variety of composite materials, such as air-polymer dielectric composites and two-dimensional (2-D) polymer microstructures, and investigated numerically and experimentally the scattering and diffusion of THz radiation in such materials, e.g. for use as THz diffusers. The results showed that THz polymer microstructures with an inhomogeneous structure can redistribute the incident THz radiation over a wide range of angles off-axis from the incident beam.

The numerical model was further extended to determine the effects of multiple scattering on the polarisation of EM waves escaping from the composite materials, especially at large scattering angles. The propagation of THz pulses through polyethylene containing gold-coated silica microspheres was investigated experimentally, to determine the angle- and frequency-dependent depolarisation in a medium with high scattering and low absorption loss. The results showed that depolarisation increases with angle off-axis from the incident beam at high frequencies. The prediction of Monte-Carlo modelling was found to be in good agreement with the experimental data.



# Contents

<b>Acknowledgments</b>	<b>v</b>
<b>List of Publications</b>	<b>vii</b>
<b>Abstract</b>	<b>xi</b>
<b>List of Figures</b>	<b>xvii</b>
<b>List of Tables</b>	<b>xxv</b>
<b>1 Introduction</b>	<b>1</b>
1.1 Introduction . . . . .	1
1.2 Motivation and Scope of the Thesis . . . . .	2
1.3 Background . . . . .	2
1.4 Polymer Composite Materials . . . . .	6
1.4.1 History . . . . .	6
1.4.2 Nanocomposite Materials . . . . .	7
1.5 Rare-Earth Doped Materials . . . . .	9
1.5.1 History . . . . .	9
1.5.2 Optical Gain . . . . .	11
1.6 THz Propagation in Highly Scattering Composite Materials . . . . .	13
1.6.1 THz History . . . . .	13
1.6.2 Highly Scattering Composite Materials . . . . .	17
1.7 Thesis Overview . . . . .	20
1.7.1 Structure of the Thesis . . . . .	20
1.7.2 Contributions of This Thesis . . . . .	21
<b>2 Optical Properties of Polymer Nanocomposite Materials</b>	<b>23</b>
2.1 Introduction . . . . .	23

2.2	Scattering Regimes . . . . .	24
2.2.1	Rayleigh Scattering . . . . .	24
2.2.2	Mie Scattering . . . . .	25
2.2.3	Multiple Scattering . . . . .	27
2.3	Effective-Medium Theory . . . . .	29
2.3.1	Total Differential Effective-Medium Theory . . . . .	30
2.4	Prediction of Optical Properties of Composite Materials . . . . .	31
2.5	Summary . . . . .	37
<b>3</b>	<b>Optical Gain in Polymer Nanocomposites</b>	<b>39</b>
3.1	Introduction . . . . .	39
3.2	Interaction of Light and Matter . . . . .	41
3.2.1	Basic Mechanisms of Rare-Earth Ions . . . . .	41
3.2.1.1	Spontaneous and Stimulated Emissions . . . . .	41
3.2.1.2	Radiative Transfer . . . . .	42
3.2.1.3	Non-Radiative Transfer . . . . .	44
3.2.1.4	Upconversion . . . . .	45
3.2.1.5	Quenching . . . . .	45
3.3	Rare-Earth Ion Doped Polymer Amplifiers . . . . .	46
3.3.0.6	Synthesis of Phosphate Glass Doped Nanoparticles . . . . .	49
3.3.0.7	Material Parameters . . . . .	51
3.3.1	Optical Loss and Gain . . . . .	52
3.4	Summary . . . . .	56
<b>4</b>	<b>EM Waves in Strongly Scattering Composite Materials with Boundaries</b>	<b>59</b>
4.1	Introduction . . . . .	59
4.2	EM Wave Propagation . . . . .	61
4.2.1	Electromagnetic Theory . . . . .	62
4.2.2	Radiative Transfer Theory . . . . .	63
4.3	Modified Monte-Carlo Modelling . . . . .	64
4.3.1	Reflection . . . . .	67
4.4	Discussion . . . . .	68
4.5	Experiments . . . . .	68
4.5.1	Data Analysis in THz Spectroscopy . . . . .	71
4.5.2	Dynamic Range . . . . .	72
4.5.3	Etalon Reflection . . . . .	73

4.6	THz Interaction with Composite Materials . . . . .	75
4.6.1	Measurements . . . . .	75
4.6.1.1	Sample Preparation . . . . .	75
4.6.1.2	2-D Diffusers Fabrication Process . . . . .	80
4.6.1.3	Terahertz Diffuse Scattering . . . . .	81
4.7	Summary . . . . .	88
<b>5</b>	<b>Polarisation of EM Waves in Strongly Scattering Composite Materials</b>	<b>91</b>
5.1	Introduction . . . . .	91
5.1.1	Polarisation of Plane Waves . . . . .	92
5.2	Polarisation Model for Monte-Carlo . . . . .	96
5.2.1	Polarisation . . . . .	98
5.3	Discussion . . . . .	99
5.3.1	Polarisation Dependant THz Scattering . . . . .	106
5.3.1.1	Experimental Method . . . . .	108
5.3.2	Results . . . . .	109
5.4	Summary . . . . .	114
<b>6</b>	<b>Conclusion and Future Work</b>	<b>119</b>
6.1	Summary of Results . . . . .	119
6.2	Future Work . . . . .	120
<b>A</b>	<b>Materials</b>	<b>123</b>
A.1	Properties of Materials . . . . .	123
A.1.0.1	PMMA . . . . .	123
A.1.0.2	SiO <sub>2</sub> Nanoparticles . . . . .	123
A.1.0.3	3-(Trimethoxysilyl)Propyl Methacrylate (MPTS) . . . .	124
A.1.0.4	2,2-Dimethoxy-2-phenylacetophenone (BDK) . . . . .	125
A.1.0.5	Azobisisobutyronitrile (AIBN) . . . . .	125
A.1.0.6	9-Vinylanthracene (9-VA) . . . . .	126
A.1.1	Surface Modification of Silica Nanoparticles . . . . .	127
A.1.2	In Situ Polymerisation . . . . .	128
A.1.2.1	Removal of Inhibitor . . . . .	128
A.1.2.2	Thermal Polymerisation . . . . .	128
A.1.2.3	Photo-Polymerisation . . . . .	130
A.1.3	Solution Blending . . . . .	131

---

A.1.4	Polymer Nanocomposite Thin Films . . . . .	131
<b>B</b>	<b>Mie Scattering for Infinite Cylinder</b>	<b>135</b>
	<b>List of Acronyms/Abbreviations</b>	<b>137</b>
	<b>Symbols</b>	<b>139</b>
	<b>References</b>	<b>141</b>

# List of Figures

1.1	The electromagnetic spectrum. . . . .	3
1.2	Light scattering regimes. . . . .	4
1.3	Direct writing system. . . . .	5
1.4	Nanostructures: (a) nanoparticles (0-D), (b) nanowires (1-D), (c) thin films (2-D), and (d) nanocomposites . . . . .	7
1.5	Schematic illustration of the preparation of polymer nanocomposites via in situ polymerisation or solution mixing . . . . .	9
1.6	Spontaneous emission of erbium. . . . .	10
1.7	$\text{P}_2\text{O}_5:\text{Er}^{3+}/\text{Yb}^{3+}$ nanoparticle-doped PMMA. . . . .	13
1.8	Terahertz generation by ultrafast photoconductive switches . . . . .	14
1.9	Terahertz detection by ultrafast photoconductive switches . . . . .	15
1.10	General configuration of a time-domain spectrometer. . . . .	16
1.11	Measuring THz pulses using photoconductive sampling . . . . .	17
1.12	Multiple light scattering by a random collection of microspheres. . . . .	18
1.13	Terahertz diffuse scattering from a highly scattering medium . . . . .	19
2.1	Scattered photons in (a) Rayleigh, and (b) Mie regimes. . . . .	26
2.2	The types of scattered photon that exit from a highly scattering medium. . . . .	28
2.3	The transmission of light propagating through a highly scattering medium with length $L$ , scattering coefficient of $16 \text{ cm}^{-1}$ , absorption loss of $1.5 \text{ cm}^{-1}$ . . . . .	28
2.4	(a) and (b) depict the corresponding random media used to derive the effective refractive index within the Maxwell-Garnett and Bruggeman theories. . . . .	30
2.5	Optical loss for glass nanoparticles embedded in PMMA vs particle size and volume fraction at $\lambda=1350 \text{ nm}$ . . . . .	32

2.6	Extinction coefficient spectrum for nanocomposite with 20 nm diameter titanium dioxide particles in PMMA for various volume fractions. . . .	32
2.7	Extinction coefficient spectrum of nanocomposite with 20 nm diameter air bubbles in PMMA for various volume fractions. . . . .	33
2.8	Extinction coefficient spectrum of nanocomposite with 20 nm diameter glass particles in PMMA for various volume fractions. . . . .	34
2.9	Transmission spectra through 1 cm of PMMA-SiO <sub>2</sub> nanocomposite with 10% SiO <sub>2</sub> by volume. . . . .	34
2.10	Comparison between Maxwell-Garnett and measured refractive index of different nanoparticles (SiO <sub>2</sub> , ZnO, and TiO <sub>2</sub> with 50 nm, 25 nm, and 30 nm in radius) embedded in PMMA vs volume fraction at $\lambda=750$ nm. . . . .	35
2.11	Comparison between Mie theory and measured absorption of TiO <sub>2</sub> nanoparticles embedded in PMMA with 30% volume fraction. . . . .	36
2.12	The dependence of $dn/dT$ on volume fraction in TiO <sub>2</sub> / PMMA and SiO <sub>2</sub> /PMMA. . . . .	36
3.1	Schematic of the energy state of $4f^N$ electrons. $S$ is the total spin angular momentum of all electrons in the system, and $L$ is the total orbital angular momentum. . . . .	42
3.2	Absorption, spontaneous, and stimulated emission. . . . .	42
3.3	Schematic of the cross-relaxation process. . . . .	45
3.4	The schematic of the up-conversion process. . . . .	46
3.5	P <sub>2</sub> O <sub>5</sub> :Er <sup>3+</sup> /Yb <sup>3+</sup> nanoparticle-doped PMMA. . . . .	47
3.6	Energy scheme of Er and Yb ions; arrows with dotted line indicate spontaneous emission. . . . .	47
3.7	Synthesis process of doped glass nanoparticles. . . . .	50
3.8	Size distribution of doped-glass nanoparticles into distilled water, measured using Zetasizer. . . . .	51
3.9	SEM picture of nanoparticles after filtration. . . . .	51
3.10	Dependence of the optical gain on Yb <sup>3+</sup> /Er <sup>3+</sup> concentration for a device length of $L=1$ cm and different pump intensities. . . . .	52
3.11	Optimal length obtained by maximising the gain P <sub>2</sub> O <sub>5</sub> :Er <sup>3+</sup> /Yb <sup>3+</sup> as a function of Yb <sup>3+</sup> /Er <sup>3+</sup> concentration. . . . .	53
3.12	Optical gain for various pump intensities versus the length of amplifier including 10% nanoparticles with 100 nm radius. . . . .	53

3.13	Optical gain as a function of length with pump intensity $I_p=1 \text{ mW}/\mu\text{m}^2$ and signal intensity $I_s=1 \text{ }\mu\text{W}/\mu\text{m}^2$ for nanoparticles with different radii, $r$ , and volume fraction of 10 % . . . . .	54
3.14	Signal gain versus length with launched pump intensity $I_p=1 \text{ mW}/\mu\text{m}^2$ , launched signal intensity $I_s=1 \text{ }\mu\text{W}/\mu\text{m}^2$ for different volume fractions of nanoparticles with 100 nm radius. . . . .	55
3.15	Dependence of the optical gain on pump power with launched signal intensity $I_s=1 \text{ }\mu\text{W}/\mu\text{m}^2$ and length 5 mm for different volume fractions of nanoparticles with 100 nm radius. . . . .	55
3.16	Flow chart of optimisation for maximising optical amplification in polymer nanocomposites. . . . .	57
4.1	Geometry of a multiple scattering event in an air-polymer composite material (photons are launched at a single point of entry). . . . .	61
4.2	(a) random spatial and temporal fluctuations of refractive index, (b) randomly distributed scattering and absorption scatterers. . . . .	62
4.3	Photon packet's position in the scattering medium with the direction of propagation defined by the polar and azimuthal angles. . . . .	65
4.4	A new direction of photon after being scattered. . . . .	67
4.5	Simulated light transmission from the surface of $X_1$ after propagation of a 120 GHz beam through a $Y \times X = 1 \times 10 \text{ mm}^2$ slab of air-polymer composite. Escaped photons contributed to the transmittance pattern, i.e. intensity per solid angle. . . . .	69
4.6	Simulated light transmission from the surface of $Y_1$ after propagation of a 120 GHz beam through a $Y \times X = 1 \times 10 \text{ mm}^2$ slab of air-polymer composite. Escaped photons contributed to the transmittance pattern, i.e. intensity per solid angle. . . . .	70
4.7	Experimental arrangement for measurements of angle- and frequency-dependent THz scattering in a strongly scattering medium. . . . .	70
4.8	Dynamic range is defined relative to the noise floor. . . . .	73
4.9	The Etalon effect caused by multiple reflections. . . . .	74
4.10	THz pulses transmitted through an air-polycarbonate composite material with 20 mm thickness. . . . .	74
4.11	Foamed polycarbonate materials. . . . .	76

4.12	Experimental and simulated total attenuation coefficient (absorption plus scattering) for air-polycarbonate composite material with thickness 1 mm and 5 mm. . . . .	77
4.13	Time-domain THz waveform measured with THz-TDS for samples with 14 mm diameter by 1 and 5 mm thickness. . . . .	77
4.14	The spectrum of the THz pulse transmitted by taking the Fourier transform of the time-domain THz waveform for the samples. . . . .	78
4.15	Simulated radiation pattern at 300 GHz following transmission through (a) 1 mm, and (b) 5 mm thick pucks of air-polymer composite materials, 14 mm in diameter. The radial scale is in decibels. . . . .	79
4.16	Optical images of polycarbonate microstructures: (a) microstructure fabricated by stacking microtubes, (b) magnified top view. Scale bars show 500 $\mu\text{m}$ resolution. As a result of cutting, the inner tubes appear closed. . . . .	81
4.17	Optical images of polycarbonate microstructures: (a) stacking solid rods between microtubes, and (b) magnified bottom view. Scale bars show 500 $\mu\text{m}$ resolution. As a result of cutting, the inner tubes appear closed. . . . .	81
4.18	Monte-Carlo model for polymer microstructures with infinite height, modelled using a Monte-Carlo algorithm. . . . .	82
4.19	THz waveforms transmitted through randomly distributed polymer microstructures (blue), and solid rods (red). The reference waveform (green) has been reduced by a factor of 10. . . . .	83
4.20	THz waveforms transmitted through randomly distributed polymer microstructures (red), and solid rods (blue). . . . .	83
4.21	The amplitude of the received THz pulse as a function of angle of arrival for polymer microstructures with microtubes and with solid rods. . . . .	84
4.22	The spectrum of the THz pulse transmitted by taking the Fourier transform of the time-domain THz waveform for: (a) polymer microstructures without solid rods at 0 and 60 degrees, (b) the structure with solid rods at 0 and 120 degrees. [Note the weak signal transmitted from sample (a) at obtuse angles]. The dashed lines show the noise floor. . . . .	85
4.23	Experimental and simulated total attenuation coefficient, i.e. absorption plus scattering, for polycarbonate microstructures comprised of microtubes and solid rods. . . . .	86



4.24	Measured transmission pattern following propagation of (a) a 300 GHz and (b) a 500 GHz beam through the polymer microstructures without solid rods. The sample was located in the vertical direction. -210 dB shows the noise floor. . . . .	87
4.25	The scattering radiation of (a) a 300 GHz and (b) a 500 GHz beam by a 2-D polymer microstructure with 10% solid rods. -210 dB shows the noise floor. . . . .	88
4.26	Simulated transmission pattern after propagation of (a) 300 GHz and (b) 500 GHz beams through polymer microstructures containing solid rods (NB: data are shown between -90 and 120 degrees to be comparable to measurements). . . . .	89
5.1	Helicity of circularly polarised light changes when the photon is scattered. As a possibility, the plane of $S_1$ - $S_3$ can change to $S_1$ - $S_2$ (blue signal) . . . . .	94
5.2	A series of Henyey-Greenstein functions for different anisotropy factors (g). . . . .	95
5.3	The ratio of the degree of polarisation as a function of $d/l$ , for three values of size parameter (x). . . . .	96
5.4	Poincaré sphere with the three Stokes parameters. . . . .	97
5.5	M matrix for an air bubble with radius $400 \mu\text{m}$ in polycarbonate. . . .	100
5.6	Effect of size parameter with the same volume fraction in a sample with $Y \times X = 1 \times 10 \text{ mm}^2$ dimension on DOP of linearly polarised and circularly polarised light transmitted vertically from $Y_1$ . . . . .	101
5.7	DOP statistics of the sample described in the text after propagation of circularly polarised light at 120 GHz. The light transmitted from $Y_1$ . .	101
5.8	DOP statistics of the sample described in the text after propagation of linearly polarised light at 120 GHz. The light transmitted from $Y_1$ . . .	102
5.9	The Stokes parameters of transmitted light from the surface of $X_1$ after propagation of a 120 GHz linearly polarised beam through a $Y \times X = 1 \times 10 \text{ mm}^2$ slab with randomly distributed air bubbles in polycarbonate.	103
5.10	The Stokes parameters of transmitted light from the surface of $Y_1$ after propagation of a 120 GHz linearly polarised beam through a $Y \times X = 3 \times 10 \text{ mm}^2$ slab with randomly distributed air bubbles in polycarbonate.	103

5.11	Dependence of the transmitted light for a circularly polarised beam on the transmission direction from the surface of $X_1$ after propagation of a 120 GHz circularly polarised beam through a $Y \times X = 3 \times 10 \text{ mm}^2$ slab with randomly distributed air bubbles in polycarbonate. . . . .	104
5.12	Dependence of the transmitted light for a circularly polarised beam on the transmission direction from the surface of $Y_1$ after propagation of a 120 GHz circularly polarised beam through a $Y \times X = 1 \times 10 \text{ mm}^2$ slab with randomly distributed air bubbles in polycarbonate. . . . .	105
5.13	The Poincaré sphere of transmitted light from the surface of $Y_1$ for 500 GHz circularly polarised light through a $Y \times X = 1 \times 10 \text{ mm}^2$ slab with randomly distributed air bubbles in polycarbonate. . . . .	105
5.14	Time-domain THz waveform measured with THz-TDS for the thin sample, $L=1 \text{ mm}$ , for the linear polarisation components: (a) y-polarisation, and (b) x-polarisation. . . . .	106
5.15	Intensity for x- and y-polarised light propagating through the sample ( $L=1 \text{ mm}$ ). . . . .	107
5.16	Depolarisation ratio for linearly polarised light as a function of frequency for angles of $0^\circ$ and $60^\circ$ . . . . .	108
5.17	The experimental arrangement for measurements of angle-dependent THz scattering in strongly scattering media. . . . .	109
5.18	Scattering length and total loss predicted by the developed Monte-Carlo model. The dashed line shows the diffusion regime. . . . .	110
5.19	Time-domain THz waveform measured with THz-TDS for the sample at different angles . . . . .	110
5.20	THz signals transmitted through a random medium consisting of gold coated silica microspheres at positive angles and (b) negative angles from the incident beam. The dashed lines show the noise floor. . . . .	111
5.21	THz signals transmitted through a random medium consisting of gold coated silica microspheres at negative angles from the incident beam. The dashed lines show the noise floor. . . . .	112
5.22	Phases of the Fourier transforms of the THz transmission at different angles. . . . .	113
5.23	The effective refractive index of the composite material at 0 degrees. . .	114
5.24	Scattering length as a function of frequency and angle of arrival. . . .	114
5.25	The depolarisation ratio for linearly polarised light as a function of frequency for different angles, $0^\circ$ and $45^\circ$ . . . . .	115

5.26	The THz scattering radiation of (a) 300 and (b) 500 GHz beams by the composite material. -210 dB shows the noise floor. . . . .	116
5.27	The THz radiation received in the direction orthogonal to the incident polarised light at (a) 300 and (b) 500 GHz. -220 dB shows the noise floor.	117
5.28	Flow chart of developed algorithm of the Monte-Carlo program. . . . .	118
A.1	Chemical structure of Poly(methylmethacrylate). . . . .	124
A.2	Schematic illustration of three types of Silanol groups on the surface of silica nanoparticles. . . . .	124
A.3	Molecular structure of 3-(Trimethoxysilyl)Propyl Methacrylate (MPTS). . . . .	124
A.4	Molecular structures of BDK: (a) before, and (b) after UV illumination. . . . .	125
A.5	Decomposition formula of AIBN upon heating. . . . .	126
A.6	Molecular structures of 9-Vinylnanthracene (9-VA). . . . .	126
A.7	Surface modification of silica with MPTS. . . . .	127
A.8	FTIR of unmodified and functionalised silica nanoparticles. . . . .	128
A.9	Purifying methyl methacrylate using a vacuum distillation. . . . .	129
A.10	Inhibitor remaining in the bottom of the flask. . . . .	129
A.11	Changes in the refractive index of polymer doped with BDK under UV irradiation at various exposure times. . . . .	130
A.12	FTIR of PMMA-silica nanocomposite with 5% silica. . . . .	131
A.13	Thermo gravimetric analysis (TGA) of SiO <sub>2</sub> , SiO <sub>2</sub> -MPTS, PMMA, PMMA/SiO <sub>2</sub> , and PMMA/SiO <sub>2</sub> -MPTS; TGA was performed in nitrogen at a heating rate of 10°C/min. . . . .	132
A.14	Optical loss spectra of PMMA, PMMA/SiO <sub>2</sub> , and PMMA/SiO <sub>2</sub> -MPTS. . . . .	133



## List of Tables

1.1	Rare-earth ions doped in a range of host materials. . . . .	12
1.2	Optical and transport properties of a random medium . . . . .	18
2.1	Limiting values for polymer nanocomposites with 80% $\text{cm}^{-1}$ transmittance. . . . .	35
3.1	Luminescence wavelengths of rare-earth ions. . . . .	43
3.2	Parameters used in the optical gain calculation for the $\text{P}_2\text{O}_5:\text{Er}^{3+}/\text{Yb}^{3+}$ /PMMA nanocomposite optical amplifier. . . . .	49
4.1	Values for diffuse transmittance from the top (Y) and end (X) bound- aries of an air-polymer composite slab. . . . .	69
5.1	DOP of linearly and circularly polarised light transmitted at orthogonal boundaries. Their normalized Stokes vectors are Shown in Figs 5.10 to 5.13 . . . . .	102
A.1	Tencor Data of the Prepared PMMA, PMMA/ $\text{SiO}_2$ , and PMMA/ $\text{SiO}_2$ - MPTS thin films spin-coated at 2000 rpm for 30 sec. . . . .	133



# 1

## Introduction

This chapter provides general information concerning the optical properties of polymer composite materials from the optical to the terahertz (THz) domains, from the active to the passive materials, and reviews potential optical devices based on composite materials. It separately gives an overview of the historical developments and the recent state of technology in polymer composite materials and the generation and detection of the terahertz radiation as well as the basic principles of THz time-domain spectroscopy to highlight how technologies in these fields have progressed up to now. The aims, motivation and thesis outline are also included.

### 1.1 Introduction

In recent years, there has been growing interest in the development and exploitation of new materials based on polymers for a new generation of integrated optic devices and systems [1, 2]. Compared with semiconductors, polymers have significant advantages in terms of low-temperature processing, low-cost materials, and easy fabrication with high precision [3]. However, optical components such as switches, waveguides, couplers, and filters require materials with specific properties, such as transparency, nonlinearity, and high refractive index [1–6]. Therefore, a key challenge is how to enhance the

performance and/or tune the properties of polymers to meet different application needs.

Composite materials (i.e. a substance composed of reinforcement embedded in a matrix) can be promising to add new functionalities and design new polymeric materials with tailored physical, optical and chemical properties [6–9]. A problem with polymer composite materials is their optical loss, resulting from scattering and absorption at 1550 nm. To compensate for the latter and intrinsic losses, optical amplifiers can be fabricated by incorporating active elements such as rare-earth ions [10]. However, the doping of polymers with rare-earth ions is much more complicated than that of semiconductors and glasses [11]. In terms of fabrication, highly photosensitive polymers should be employed to structure waveguides and/or to post-process optical devices.

Due to the lack of attention to the effects of scattering and also increasing attention to terahertz technology, it is also important to investigate terahertz scattering, particularly characteristics such as spatial and spectral intensity distributions. This study may lead to new components based on highly scattering media in the THz region.

## 1.2 Motivation and Scope of the Thesis

The research reported in this thesis is focused on four major themes: a) synthesis of polymer composite materials and investigation of their optical properties, b) design optimisation of optical amplifiers made using polymer nanocomposites doped with rare-earth ions, c) numerical modelling of scattering media including boundaries, and d) numerical and experimental studies of THz scattering.

## 1.3 Background

The electromagnetic spectrum (shown in Fig. 1.1) is classified into radio, microwave, terahertz, infrared, ultraviolet, X-ray and gamma rays. For certain applications, the wavelength range of interest depends on the structure of the matter and the energy of the photons. For example, most polymers (such as poly(methyl methacrylate)) are transparent at visible wavelengths, and can be used to fabricate optical devices such as, waveguides, amplifiers, optical switches, etc. [12]. At short wavelengths, Rayleigh scattering diminishes the performance of polymer optical waveguides, and in the infrared range strong molecular absorption becomes important to the efficiency of polymer-based optical devices [13]. Another interesting regime is at terahertz (THz) frequencies because it bridges the gap between electronic and photonic regimes. THz technology



has been opening new and interesting applications in the field of THz communication, sensing, non-destructive testing, and high-resolution imaging [14–17].

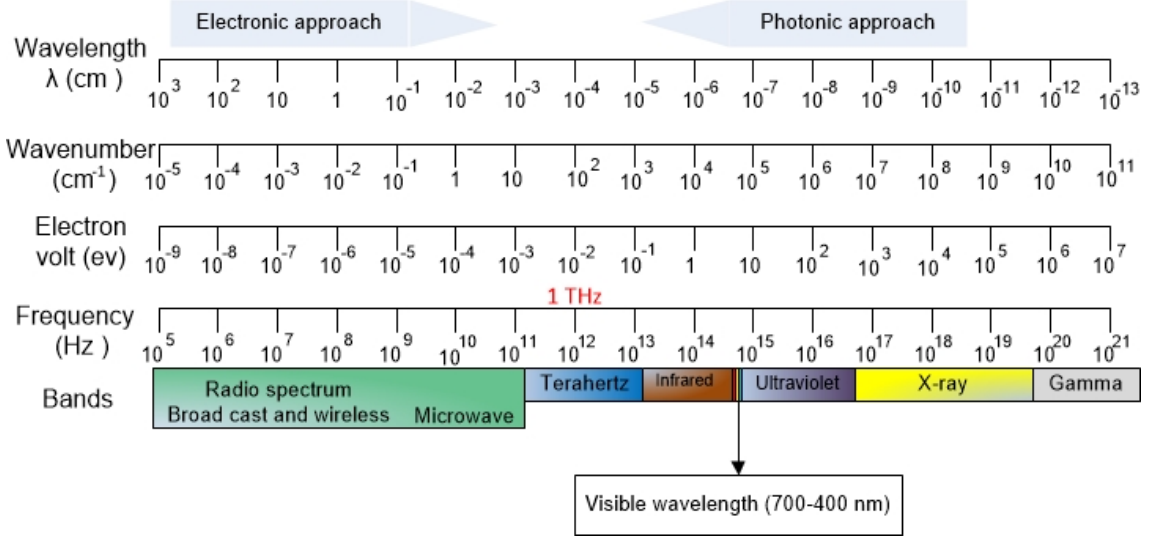


FIGURE 1.1: The electromagnetic spectrum.

It is important to be able to predict and control the optical properties of materials at the wavelength range of interest. The optical characteristics are mainly related to absorption, scattering, and transmission of electromagnetic(EM) wave propagating through a medium, and photorefractive and photosensitive mechanisms of materials. Light is absorbed by two basic mechanisms: (i) the promotion of an electron to a higher energy state if the photon energy is greater than that of the band gap, and (ii) molecular vibrations, in particular at IR wavelengths, which do not have the energy to induce an electronic transition.

Light scattering is the dispersal of an incident beam from the original direction of propagation as a result of changes in the refractive index of the propagation medium. Single scattering prevails in optically thin and weakly scattering media, as incident beams have a high probability to propagate out of the medium before being scattered again. In the case of multiple scattering, the light may undergo many changes in direction, polarisation state, phase, and amplitude as it interacts with highly scattering and weakly absorptive media [18]. The regimes of particle scattering are shown in Fig. 1.2, depending on the particle size, and the light wavelength. The scattering crosses over from the Rayleigh regime to the Mie regime when the particle size becomes larger than around 10% of the wavelength of the incident beam. In the case of multiple scattering, the latter regimes become more complicated than single scattering, depending on the optical loss resulting from both scattering and absorption, the

volume fraction of particles, and the refractive index. The transmission of EM wave propagating through a multiply scattering medium can be separated into two components: (i) ballistic photons, and (ii) diffuse photons. The ballistic photons scatter only in the forward direction. The diffuse waves comprise multiple-scattered photons, which randomise their polarisation.

In photorefractive materials, the beam interacts with a medium and produces a non-uniform space-charge configuration. The resulting carriers drift and diffuse and hence an internal electric field variation is formed which modifies the refractive index of the material through the electro-optic effect [19]. In contrast, the refractive index of photosensitive materials can be permanently changed by, for instance, UV-irradiation to fabricate waveguides and optical components such as a Bragg grating [20]. One technique to design and rapidly fabricate planar waveguides is the direct laser writing method [21], shown in Fig. 1.3.

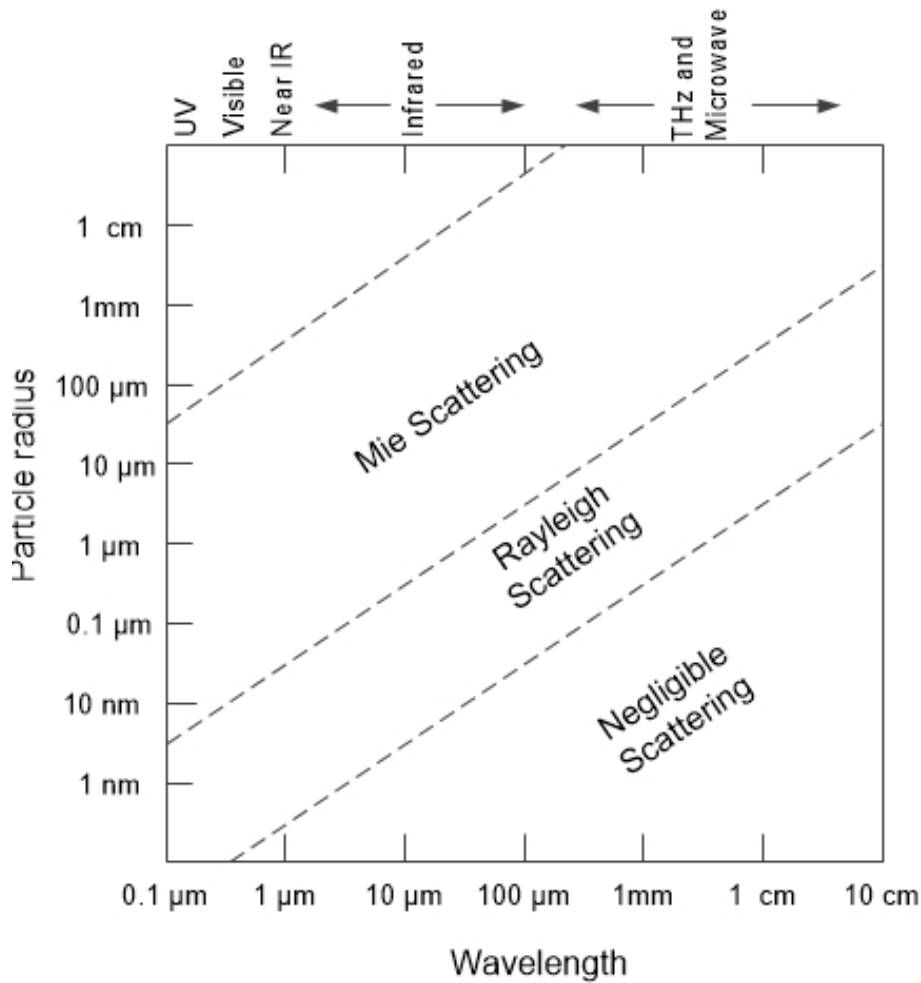


FIGURE 1.2: Light scattering regimes.

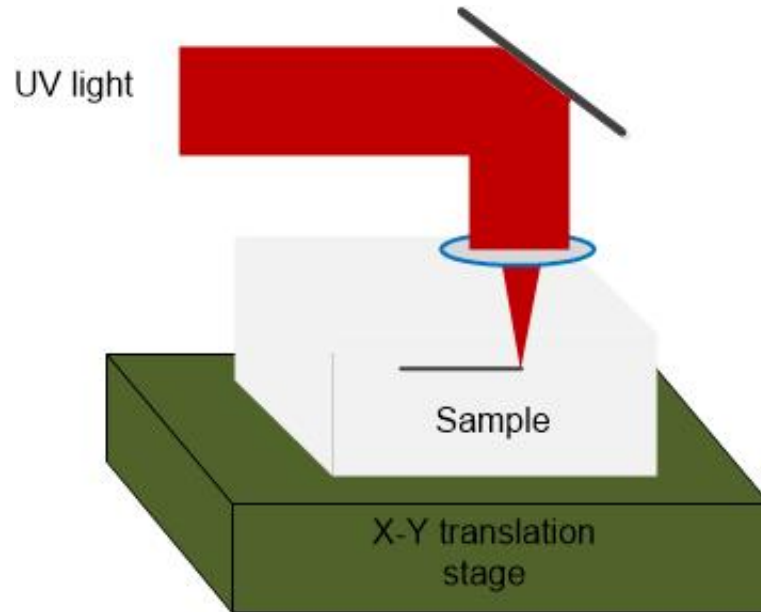


FIGURE 1.3: Direct writing system.

It is difficult to find a single and homogeneous material that possesses the required characteristics (optical, thermal, and mechanical properties) for a given application. Therefore, developing new materials with desirable properties is deemed necessary. Different materials exhibit a different dependence on the wavelength of the EM wave. Metals, for instance, are strongly absorptive throughout the entire visible spectrum but are reflective in the THz range. On the other hand, some dielectric materials are transparent in both the visible and the THz range with low and/or high refractive indices. Therefore, it seems that composite materials, including both nano- and micro-structures, are a promising new class of materials which provide a new perspective on the design of materials with optimised properties or with tailored multi-functional properties.

A composite material can be defined as a combination of two or more constituent materials with different properties, resulting in a material with characteristics unattainable by the individual components. Although many studies have focused on the preparation and the characterisation of composite materials, much progress has also been made in improving the mechanical and thermal properties of polymer materials. However, investigation of the optical properties of composite materials and study of optical devices based on polymer composite materials is still a developing area.

## 1.4 Polymer Composite Materials

### 1.4.1 History

For the first time, Carter *et al.* (1950) fabricated polymer composite materials by compounding a polymer with layered silicate [22]. They showed that the resulting product modified the hardness, modulus and tensile strength. In 1959, R. Feynman declared “there is a plenty of room at the bottom” and described the possibility to create nano-sized products [23]. In the 1960s, Nalsia studied the combination of organoclay and thermoplastic polymer matrix and provided tough solvent resistance and large tensile strength organoclay composites by irradiation-induced cross-linking [24]. Blumstein (1965) found an improvement in the thermal stability of poly(methyl methacrylate) (PMMA) by combining it with montmorillonite clay [25]. In 1974, Taniguci introduced the term of nanotechnology as a new field of science to describe semiconductor processes such as thin film deposition on the order of nanometres. In 1976, Fujiwara and Skamoto demonstrated the first organocalys hybrid polyamide nanocomposite to study the flame-retardant properties of these materials [26].

In 1981, A. Ekimove discovered nanocrystalline, semiconductor quantum dots in a glass matrix and characterised their optical and electrical properties [27]. For the first time (according to [28]), a polymer inorganic nanocomposite was reported by Ludersdorf in 1986; he showed interesting optical properties such as dichroism by coprecipitation of gum arabic and a gold salt in ethanol. In 1991, carbon nanotubes were discovered by S. Iijima. In the nineteenth and early twentieth, Faraday, Fischer, Mie and Zsigmondy realised the size-dependent properties of particles; the surface density (i.e. surface area per unit volume) in nano and micro scales is inversely proportional to the size of the particles [28]. Typical nanoparticles which are currently under investigation mainly include semiconductors (e.g. PbS, ZnO, CdSe, CdS) and metal nanoparticles (e.g. Au, Ag, Cu, Ge, Pt, Fe), oxides (e.g. TiO<sub>2</sub>, SiO<sub>2</sub>), carbon-based materials such as nanotubes, and nanowires [8, 29–36].

All mentioned nanomaterials provide their own advantages and challenges depending on their potential applications for polymer-based devices. For example, polymer nanocomposites can be used in electrical and thermal applications in which carbon nanotubes are used as nano-fillers to enhance both the electrical and thermal conductivity of the polymer matrix [34]. Such materials can be useful for electronic devices. Metal nanoparticles (e.g. gold, silver) can be used in polymers for sensor applications including gas and chemical sensors [37]. For magnetic applications, metal oxides are used as inorganic inclusions [38]. In order to achieve high-refractive-index polymers,

semiconductor nanoparticles (e.g. ZnO and TiO<sub>2</sub>) can be incorporated into the organic materials [39]. Recently, polymeric nanocomposites of gold and iron oxide nanoparticles have been frequently used for bioimaging agents [40]. High UV absorbing inclusions such as ZnO and TiO<sub>2</sub> have a long-term UV stability which makes them suitable as additives to polymers to prepare a UV protective coating [41]. In 2009, Yordanov *et al.* reported photoluminescence materials comprised of core-shell CdSe/CdS as inorganic nanofillers and poly(buthymethacrylate) as the polymer matrix [42].

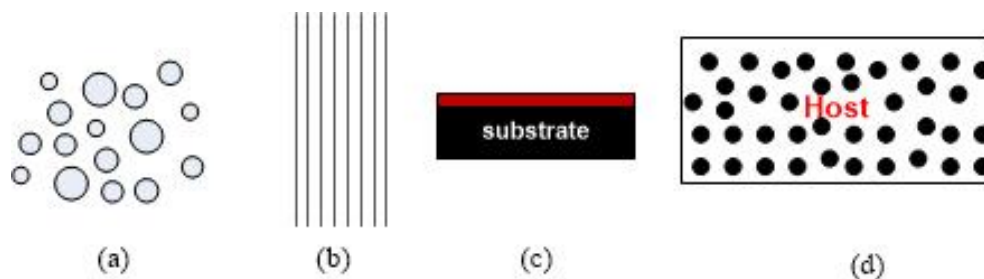


FIGURE 1.4: Nanostructures: (a) nanoparticles (0-D), (b) nanowires (1-D), (c) thin films (2-D), and (d) nanocomposites

As shown in Fig. 1.4, nanomaterials can be classified into four groups on the basis of the number of dimensions, zero- (0-D), one- (1-D), two- (2-D) and three- dimensional (3-D) nanomaterials. Zero-dimensional materials have nano dimensions in all three directions, e.g. nanoparticles. One-dimensional materials such as nanowires, nanotubes or nano rods have two dimensions in the range of nanometres. In 2-D structures, two dimensions are beyond the nanometre range, such as thin films. 3-D structures are the bulk nanomaterials which are not confined to be nanoscale in any dimension, such as nanocomposites, micro structures and mesoporous and organic-inorganic hybrids.

### 1.4.2 Nanocomposite Materials

Nanotechnology deals with characteristic lengths in the nanometre range 1-100 nanometres ( $\text{nm}=10^{-9}\text{m}$ ). Nanocomposite structures are comprised of the host (e.g. polymers) and inclusions (e.g. silica) in which their size is comparable to and/or smaller than the wavelength of the light [7]. The idea of using nanocomposites is to combine the desirable properties of the organic polymers (i.e. easy processing, flexibility) and the inorganic materials (i.e. inert, very low loss, thermal stability). A high surface-to-volume ratio of nanoparticles leads to a dramatic increase in the inter-facial region between the host and the inclusions, resulting in different optical, thermal and mechanical properties from the bulk polymers even at a relatively low volume fraction of

nanoparticles [43, 44].

A wide variety of nanoparticles can be added to tune the thermal properties of nanocomposite materials, such as the thermo-optic coefficient, and/or to change the optical properties of polymers, such as absorption, luminescence, refractive index, and electro-optic coefficient [45–49]. Therefore, such materials have the potential to further improve these properties of polymer-based optical devices, including planar waveguides, optical fibres and amplifiers, etc. The properties of polymer nanocomposites strongly depend on the size and volume fraction of the nanoparticles, the wavelength of the light, and the refractive index of inclusions and host [50].

Interactions between particles induce aggregation in which nanoparticles tend to aggregate into clusters up to several microns in size [51] and hence dramatically increase the size of inclusions; the state of the dispersion of inclusions in the host has a significant influence on the properties of nanocomposites such as the scattering loss [47]. Therefore, to optimise the effects of nanoparticles, they should be well dispersed in the polymer matrix. Moreover, the same polymer nanocomposite materials prepared using different techniques can exhibit a large variation in their properties due to the grafting densities (i.e. attaching polymer chains to the surface of nanoparticles), the type of initiators (photo and/or thermal initiators), transfer agents, and chain terminating materials. So the main challenge in the preparation of nanocomposite materials is to control the dispersion and aggregation of nanoparticles.

Polymer nanocomposites can be formed by either solution mixing or in-situ polymerisation [52, 53]. In solution mixing, first polymers are synthesised and then components are combined by blending of solutions. Although solution mixing is a relatively easy method, it has yielded low grafting densities, because polymer chains populate the surface and then it becomes hard for them to react with the surface of nanoparticles. Furthermore, this method impacts the effective size of the nanoparticles, as the dispersion of inclusions is difficult and thus they aggregate. In contrast, in the in-situ method, the surface of the nanoparticles is modified by a functional group of monomers followed by the polymerisation process, leading to an enhanced dispersion of inclusions [54]. The presence of the nanoparticle surface also contributes to the rate of chain transfer and chain termination.

Among the numerous inorganic nanoparticles, silica has attracted considerable interest for use in different applications, in particular optical devices [55]. The refractive index of silica is closely matched to that of the polymers, so that it is possible to achieve a highly transparent nanocomposite material, which is a prerequisite for a majority of

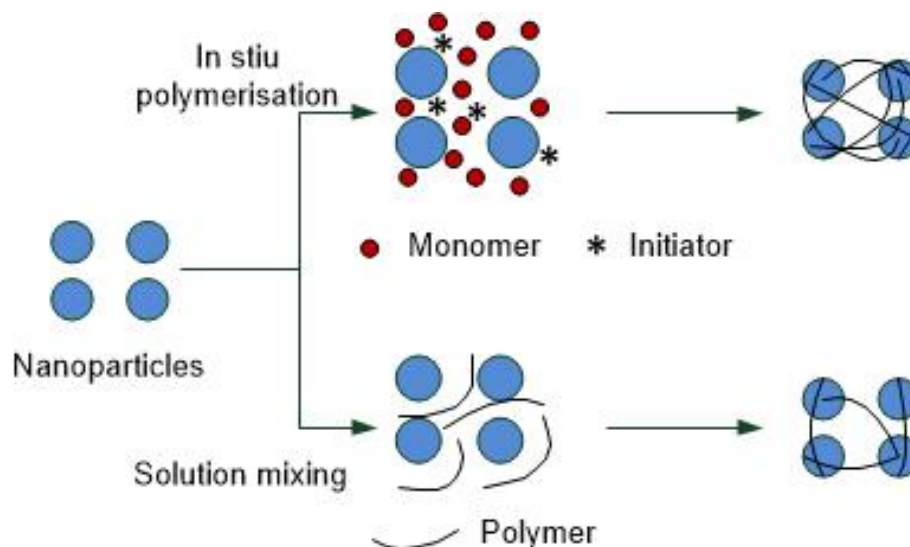


FIGURE 1.5: Schematic illustration of the preparation of polymer nanocomposites via in situ polymerisation or solution mixing

optical devices. Moreover, silica is also known to be a suitable host for the rare-earth ions, applicable in planar-waveguide amplifiers to reduce the optical loss [10]. A significant problem with polymers is their optical loss at NIR wavelengths, mainly caused by the molecular vibrations of the polymer at telecommunication wavelengths, e.g. 1.5 microns [56]. If polymers are to be useful in this wavelength range, it is important to compensate for the loss by amplifying the light. Although the nanoparticles embedded in the host result in a scattering loss due to the refractive-index mismatch between the inclusions and the host, the scattering loss can be minimised by decreasing the size of the inclusions, to significantly below the wavelength, and by refractive-index matching.

Although scientists have made remarkable progress in the preparation of polymer composites as well as in their mechanical and thermal properties, there has been limited research on the application of these materials in polymer-based optical devices. Our aim is to synthesise polymer composite materials, to investigate their optical properties.

## 1.5 Rare-Earth Doped Materials

### 1.5.1 History

The discovery of the black mineral "Ytterbite" by C. Arrhenius in 1787 was the origin of rare-earth ions, and then the J. Gadolin analysis on ytterbite yielded an unknown oxide (earth) that he called ytteria [57]. J. Berzellius obtained a white oxide from an



iron-tungsten mineral and called it ceria [58]. By 1803 there were two known rare-earth elements, yttrium and cerium. In 1839, C. Mosander separated ceria by heating the nitride and dissolving the product in nitric acid [58]. The resulting material was isolated into two new elements, lanthanum and didymium. In 1842, Monsander also separated ytteria into three oxides, ceria, terbia and erbia. In 1885, A. Welsbach showed that didymium was twin elements: neodymium and praseodymium [59]. Berlin called the earth giving pink salt erbium. In 1959, N. Bloembergen proposed a photon upconversion (UC) process in which the absorption of photons leads to the emission of light at shorter wavelengths than the excitation wavelength, as shown in Fig. 1.6 [60].

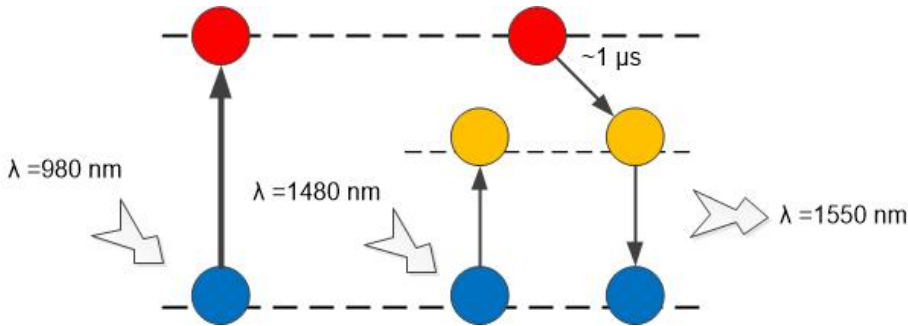


FIGURE 1.6: Spontaneous emission of erbium.

In 1963, Koester and Snitzer demonstrated the first rare-earth doped fibre amplifier using neodymium-doped fibre amplifiers with a net gain of 47 dB [61]. The first  $\text{Er}^{3+}$ -doped glass laser was also demonstrated by Snitzer and Woodcock in 1965. In 1985, neodymium-doped silica fibre was used to build a single-mode CW fibre laser. The development of semiconductor lasers in the 1980s provided sufficient light sources for fibre amplifier devices [62]. After the demonstration of Nd doped single-mode fibre amplifiers by D. Payne and *et al.* (1986), rare-earth doped optical fibres were considered to be a feasible media for making practical optical amplifier devices [63].  $\text{Er}^{3+}$  and  $\text{Nd}^{3+}$  were mostly used, as they have transitions coinciding with the low-loss telecommunications windows [64]. Although rare-earth ion doped fibre amplifiers are the most commonly used amplifier, they are incompatible with integrated optical devices due to their geometric structure which restricts their further application. The concept of integrated optics was proposed by Miller in 1969 [65]. Yajima and his colleagues demonstrated the first  $\text{Nd}^{3+}$  doped glass thin-film waveguide [66]. The waveguide operated at 1060 nm with an optical gain of 0.36 dB/cm. There then followed a continual progress and development in planar waveguides to increase the gain and reduce the loss through modifying the glass and doping with different rare-earth ions. However, the



optical communication wavelength was around 1300 nm in the early 1970s, so that the latter waveguide was not acceptable. Kitagawa *et al.* demonstrated erbium doped silica waveguides (1992) with a total gain of 21 dB in a 2.4 cm long thin film, followed by the phosphate modified silicate glass waveguide amplifiers (1993-1994) [67–69]. Since then, different materials have been studied for optical amplifiers, including glasses, crystals, and organic materials. Table 1.1 shows recent materials, with the type of preparation, and their applications.

### 1.5.2 Optical Gain

In order to achieve optical gain in a medium at a given wavelength, different types of rare-earth ions are doped into the medium. By absorbing a photon, the ion is excited from the ground state to an excited state. Electrons in the higher state can either relax spontaneously to a lower energy state by emission of a photon, or a photon may force an excited atom to decay by emitting another photon, i.e. stimulated emission. If the pump rate is large enough, population inversion between the two levels is achieved and hence stimulated emission can be a dominant factor over absorption and thus signal amplification can be obtained in the medium.

Since the position of the energy levels of the rare-earth ions is independent of the host materials, then in principle any weakly absorptive material at the pump and emission wavelengths can be used as a host. However, polymer-based optical waveguides and devices are of interest in optical communications and sensing due to their ease of fabrication and low cost. Most telecommunication systems operate at 1.5 microns, and the loss in the polymer at these wavelengths is significantly larger than in glass-based devices, and consequently optical amplification is desirable. Whilst substantial progress has been made in highly doped rare-earth inorganic materials for applications in compact amplifiers and integrated optics [88–93], relatively few materials for optical amplifiers at 1.5  $\mu\text{m}$  based on rare-earth-doped polymers have been demonstrated [11, 94–98]

The primary difficulties in achieving optical amplification in rare-earth-doped polymers are: i) the insolubility of rare-earth inorganic salts in polymers, and ii) hydrogen groups quench the radiative transitions of the rare-earth ions [97]. A promising approach to avoiding the latter difficulties is to embed rare-earth based inorganic nanoparticles into the polymer host. In this way most of the rare-earth ions are isolated from the organic host. A simple approach that we have been investigating to achieve this

TABLE 1.1: Rare-earth ions doped in a range of host materials.

Inclusions	—		
	Type	Host	application
SiO <sub>2</sub> :Er <sup>3+</sup> [70]	glass	glass	optical fibre amplifiers
Si:Er <sup>3+</sup> [71]	semiconductors	glass	
porous silicon:Er <sup>3+</sup> [72]	semiconductor	glass	
TiO <sub>2</sub> :Er <sup>3+</sup> [73]	semiconductor	glass	
GaN:Er <sup>3+</sup> [74]	semiconductor	glass	optical amplifier
GaAs:Er <sup>3+</sup> [75]	semiconductor	glass	light-emitting diodes
ZBLAN:Er <sup>3+</sup> [76]	glass	glass	laser
TeO <sub>2</sub> :Er <sup>3+</sup> [77]	crystal	glass	
PSG:Er <sup>3+</sup> [78]	glass	glass	
Al <sub>2</sub> O <sub>3</sub> :Er <sup>3+</sup> [79]	metal	metal	
LiNbO <sub>3</sub> :Er <sup>3+</sup> [80]	crystal	crystal	
YAG:Er <sup>3+</sup> [81]	crystal	crystal	
LiYF <sub>4</sub> :Yb <sup>3+</sup> , Er <sup>3+</sup> [82]	crystal	polymer	polymer waveguide
BaYF <sub>5</sub> :Yb <sup>3+</sup> , Er <sup>3+</sup> [83]	crystal	polymer	polymer waveguide
NaYF <sub>4</sub> :Yb <sup>3+</sup> , Er <sup>3+</sup> [84]	crystal	polymer	polymer waveguide
$\beta$ -NaLuYF <sub>4</sub> :Yb <sup>3+</sup> , Er <sup>3+</sup> , Tm <sup>3+</sup> , Ho <sup>3+</sup> [85]	crystal	polymer	
$\alpha$ -NaLuYF <sub>4</sub> :Yb <sup>3+</sup> , Er <sup>3+</sup> , Tm <sup>3+</sup> , Ho <sup>3+</sup> [85]	crystal	polymer	
Y <sub>2</sub> O <sub>3</sub> :Yb <sup>3+</sup> , Er <sup>3+</sup> [86]	crystal	polymer	
LaF <sub>3</sub> :Er <sup>3+</sup> , Yb <sup>3+</sup> , Eu <sup>3+</sup> , Tb <sup>3+</sup> , Ce <sup>3+</sup> [87]	crystal	polymer	polymer waveguide
NaGdF <sub>4</sub> :Eu <sup>3+</sup> , Yb <sup>3+</sup>	crystal	polymer	polymer waveguide

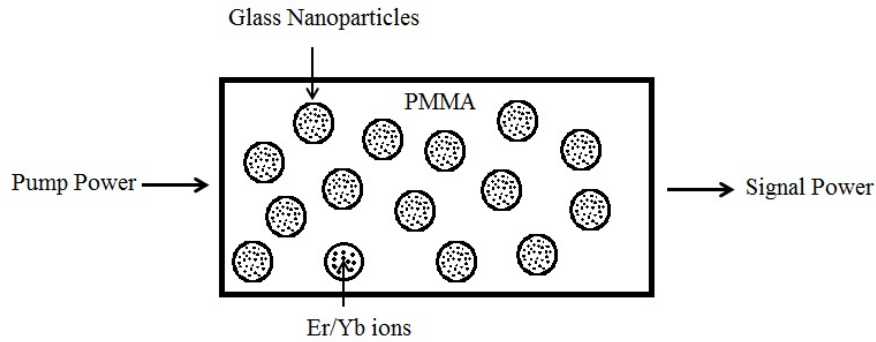


FIGURE 1.7:  $P_2O_5:Er^{3+}/Yb^{3+}$  nanoparticle-doped PMMA.

is to disperse Erbium-Ytterbium ( $Er^{+3}/Yb^{+3}$ ) co-doped glass nanoparticles into the polymer as shown in Fig. 1.7. However, a potential problem is scattering loss, which acts in addition to rare-earth absorptions in the inclusions, and loss in the polymer host. Furthermore, scattering depends strongly on the size of the inclusions relative to the wavelength, and so in an amplifier scattering will affect pump and signal intensities differently. Many parameters must therefore be taken into account in the analysis and design of nanocomposite-based optical amplifiers, including the size of the nanoparticles, their  $Er^{+3}/Yb^{+3}$  concentration, and their volume fraction within the polymer host. The values of the latter parameters are often constrained in practice (e.g. minimum size, maximum volume fraction), raising the question of whether optical gain is even possible in a given length of material with a feasible pump power.

## 1.6 THz Propagation in Highly Scattering Composite Materials

### 1.6.1 THz History

Rubens and his colleagues measured the emission spectrum of a blackbody down to the THz region [99]. The main problem was that the blackbody spectrum drops rapidly at low frequencies, except at  $T=2.7$  K. A powerful arc lamp produces enough THz light to do spectroscopy. Terahertz Fourier Transform spectroscopy was also used to produce a very broadband 0.25-30 THz source using a Hg arc lamp with bolometer at  $T=4$  K. However, as the bolometer relied on temperature, the response was very slow and also required liquid cryogenics. In 1964, Gebbie *et al.* generated terahertz gas lasers by electrical discharge [100]. In the 1970s, Hartwick used CW THz gas lasers in THz imaging systems [101]. The gas lasers can produce high-power pulses, however, their

main problems are discrete tuning, low efficiency and expensive.

As the THz regime (i.e. 300 GHz-10 THz) lies between the photonic and electronic regions, it can be generated in both ways. In the 1980s, G. Mourou *et al.* and D. Auston *et al.* fabricated photoconductive switches [102, 103]. Then, THz pulses were generated by ultrafast switches. A femtosecond (fs) pulse optically excites the gap region, producing charge carriers. The charge separation is induced by an applied bias voltage. The resulting short current pulse generates the THz pulses by coupling to an antenna as shown in Fig. 1.8. To detect the THz pulses, the semiconductor material used for antennas needs to have a short carrier life time. In 1996, Auston used a femtosecond laser to detect the THz pulses [104]. The detection is similar to the generation scheme, however the charge separation is induced by the incident THz field in which a fraction of the THz pulse separates charges and hence detects current in the order of nano amperes, shown in Fig. 1.9.

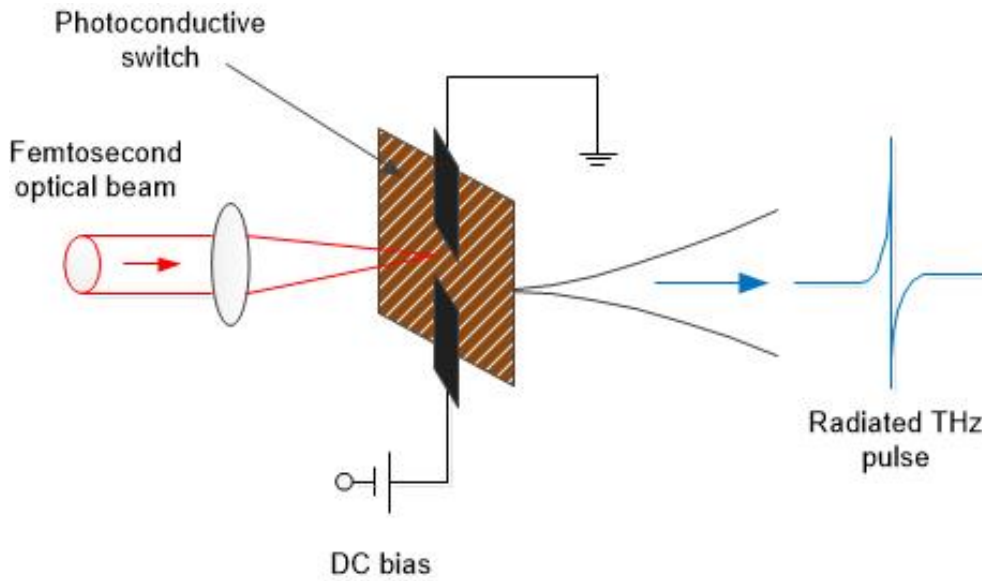


FIGURE 1.8: Terahertz generation by ultrafast photoconductive switches

The energy of the THz pulses based on photoconductive switches is only around 500 nJ. However, high energy THz ultrashort pulses are necessary for some applications such as imaging and nonlinearity terahertz spectroscopy. The crucial parameter is how to match between the optical group velocity and the THz pulse velocity, which can be achieved in some materials with an appropriate pump wavelength. The THz pulses can also be generated and detected by nonresonant nonlinear optics for optical rectification. Typical nonlinear materials used for this purpose are ZnTe, GaP, LiNbO<sub>3</sub>.

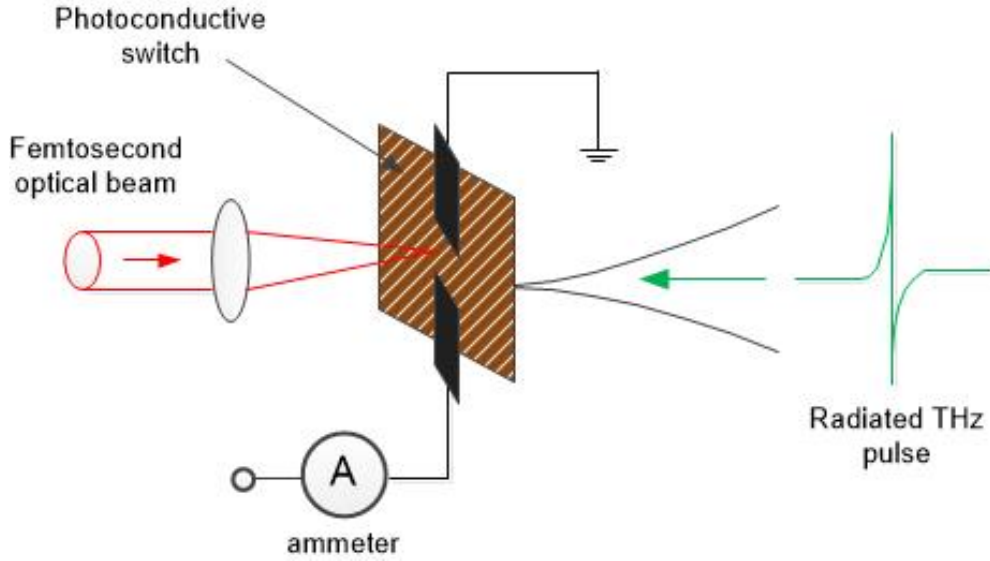


FIGURE 1.9: Terahertz detection by ultrafast photoconductive switches

In the early 1970s, Y. R. Shen *et al.* and D. H. Auston *et al.* generated THz pulses using picosecond pulses in  $\text{LiNbO}_3$  [105]. Because the process is non-resonant, the life time of the photogenerated charge carriers is not relevant. Therefore, electro-optic (EO) based THz systems have superior spectral bandwidth with high THz pulse energy compared to systems based on photoconductors. In 2007, Yeh *et al.* generated very high THz pulse energy, up to  $10 \mu\text{J}$ , using MgO doped  $\text{LiNbO}_3$  [106].

Ultraband ( $> 10 \text{ THz}$ ) combined with a very high intensity ( $\text{MV/cm}$ ) THz wave can be generated and detected using air photonic techniques, air being used as the emitter. First, single-wavelength optical excitation is used to create a plasma and then THz pulse generation is attributed to the ponderomotive force (i.e. a nonlinear force that a charged particle experiences in an homogeneous oscillating electromagnetic field) [107, 108]. Another way is to generate a second-harmonic beam by focusing a fundamental beam through a crystal such as beta barium borate. The third case is to combine the second-harmonic beam with the fundamental beam using a dichoric mirror and control the amplitude, phase, and polarisation of the beam individually. M. Clerici *et al.* in 2013 achieved high-power THz pulses up to  $4.4 \text{ MV/cm}$  by nonlinear generation in air [109]. The detection of the THz electric field (amplitude and phase) is based on the intensity of the THz-field-induced second-harmonic signal as shown in Eq. 1.1 [110].

$$I_{2\omega} \propto (\chi^{(3)} I_{\omega})^2 E_{THz} E_{DC} \quad (1.1)$$

where  $E_{THz}$  and  $E_{DC}$  are the electric-field amplitudes of the THz pulses and the DC

bias. The mentioned recent high-tech progress in THz generation and detection are really complicated and are not commercially available.

A standard THz time-domain spectroscopy (TDS) is demonstrated in Fig. 1.10 [111]. A TDS simplifies measuring the THz spectrum for a reference scan of the system without the sample present to eliminate external influences on the system. The optical detection pulse in time allows for scanning the THz pulse and sampling its electric field as a function of time, indicated in Fig. 1.11. The temporal resolution of the detected THz-induced currents is inversely related to the carrier life time. The optical delay of emitter to receiver pulse can be introduced by a motorised stage that displaces a retro mirror installed in the path of the beam directed to the receiver. It should be noted that for a coherent detection the same laser pulse generating the THz pulse has to be used for sampling. Photoconductive sampling is a coherent detection of the electric field and therefore it can be Fourier transformed to provide both the amplitude and the spectral phase. A major challenge is presented for application of THz spectroscopy at a long distance, mostly due to water vapour in the atmosphere. However this is highly frequency-dependent. For the first time, in 2014, S. Koenig *et al.* presented a wireless communication system at 237.5 GHz for transmission data over 20 m [112].

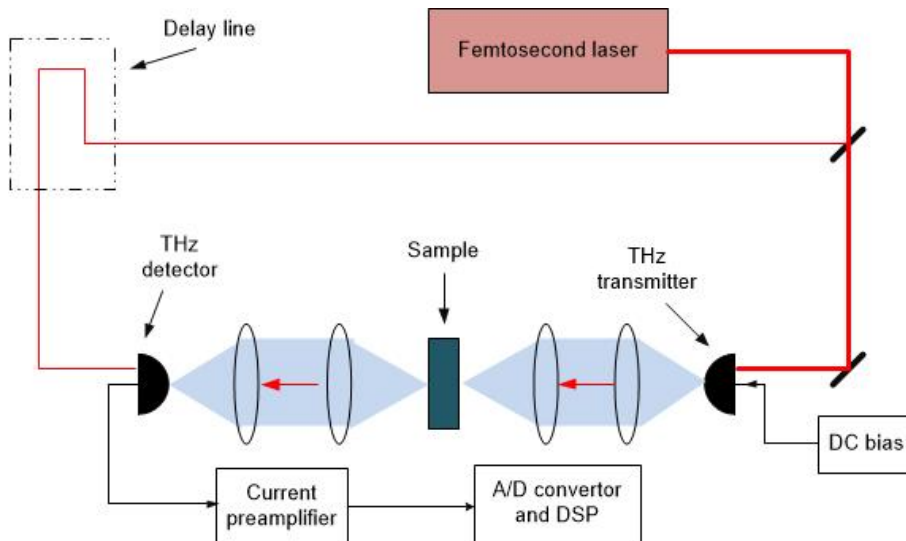


FIGURE 1.10: General configuration of a time-domain spectrometer.

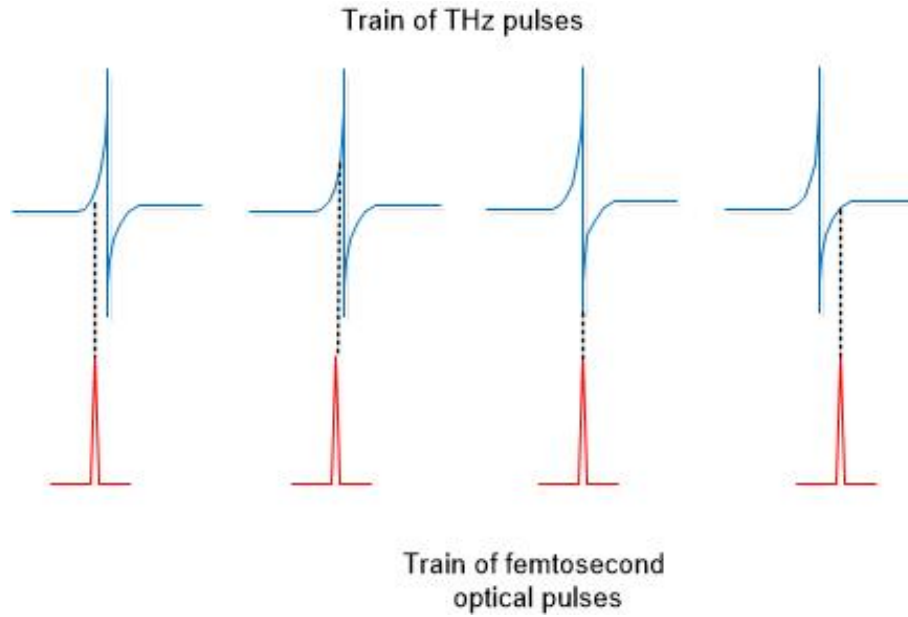


FIGURE 1.11: Measuring THz pulses using photoconductive sampling

### 1.6.2 Highly Scattering Composite Materials

According to the early sections, scattering has been considered an unwanted property in many optical applications, however it can potentially be useful for developing composite materials to introduce new functionalities which can open up new applications in telecommunication systems, sensing, imaging and spectroscopy [113–116]. Scattering in random media is known to modify the spectral content, degree of polarisation and spatial distribution of electromagnetic wave propagating through such materials [117–119]. Consequently, strongly scattering media offer new direction to light sources, imaging, and new matter-radiation interactions to explore. An example is that of a random laser obtained from porous glasses and laser crystal powders, in which photons bounce among particles long enough for amplification to occur with a duration on the scale of nanoseconds and in a narrow spectrum of about 0.1 nanometres [120]. The characteristic of most interest in the opaque materials depends upon multiple scattering (shown in Fig. 1.12), in which the distance between two scattering events is much smaller than the dimension of the medium. For example, the propagation of polarised light in highly scattering media results in a loss of initial polarisation and/or changing randomly the polarisation state of an incident wave caused by multiple scattering [121].

The transport properties based on diffusion theory can be classified into four characteristics: reduced scattering coefficient, transport mean free path, diffusion length, and optical penetration depth. The fundamental parameters describing the properties

of highly scattering media are shown in Table 1.2.

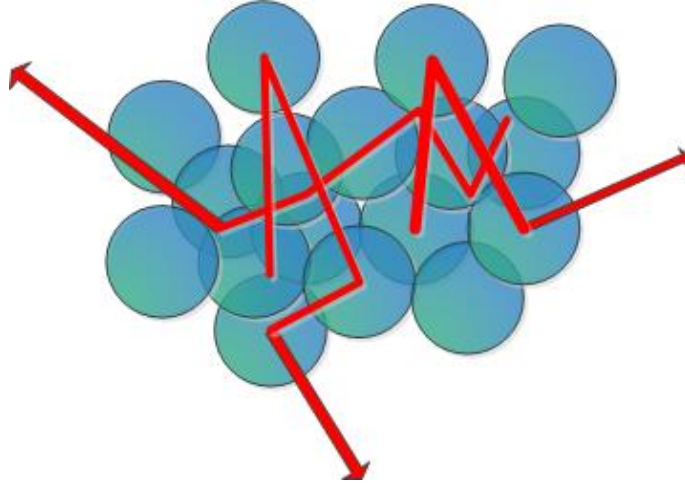


FIGURE 1.12: Multiple light scattering by a random collection of microspheres.

TABLE 1.2: Optical and transport properties of a random medium

Quantity	Symbol	units
Absorption coefficient	$\mu_a$	$\text{cm}^{-1}$
Scattering coefficient	$\mu_s$	$\text{cm}^{-1}$
Anisotropy of scattering	$g$	-
Refractive index	$n$	-
Reduced scattering coefficient	$\mu_s' = \mu_s(1-g)$	$\text{cm}^{-1}$
Transport mean free path	$l^* = 1/(\mu_s' + \mu_a)$	cm
Diffusion length	$D = l^*/3$	cm
Optical depth	$\text{Od} = \sqrt{D/\mu_a}$	cm

Although multiple scattering is a random process, its effects (such as depolarisation)



can be controlled by the specific properties of the scattering medium, i.e. the effect of boundaries, the size of particles, the volume fraction and the refractive index.

Numerous studies have investigated the degree of polarisation of the light. However, previous studies predict and evaluate the depolarisation ratio of only backscattered light in semi-infinite samples, especially at optical wavelengths [122, 123]. Highly scattering media from a foamed polycarbonate rod were fabricated; it has a simple geometry with air bubbles randomly distributed in the slab. Compared with the studies on THz scattering described in different reports, our scatterers are low-index bubbles in a high-index host, and the bubbles are inhomogeneous in size. We also fabricated different highly scattering media made by dielectrics and metals, as most of the latter materials are transparent and/or reflective at THz frequencies and may can be used in THz sensing and short-range communications. The measurements were taken using terahertz time-domain spectroscopy (THz-TDS) with a goniometer, giving both the spatial and the spectral distribution of the THz radiation transmitted through composite materials, shown in Fig. 1.13. We also measured the polarisation dependence of

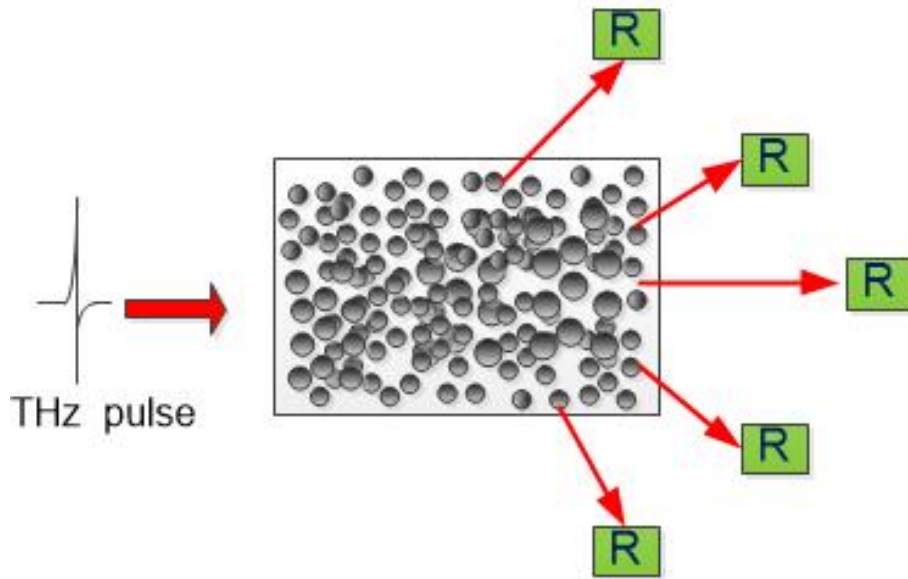


FIGURE 1.13: Terahertz diffuse scattering from a highly scattering medium

THz scattering. The results are compared to values predicted by numerical modelling, developed using a Monte-Carlo algorithm to calculate the propagation of polarised light through micro-structured materials, and to properly account for the effect of both loss and boundaries. The aim is to determine the depolarisation of linearly polarised and circularly polarised light escaping from the sample at different boundaries, especially at large scattering angles.

## 1.7 Thesis Overview

### 1.7.1 Structure of the Thesis

This thesis is organised as follows:

Chapter 1 gives an introduction to the optical properties of composite materials in both optical and terahertz ranges. It also presents a comprehensive study of recent developments in these fields.

Chapter 2 reports on detailed theoretical studies of the optical properties of PMMA containing various types of nanoparticles. Experimental work on PMMA/Silica nanocomposites is described in Appendix A, including material synthesis and characterisation.

Chapter 3 presents a detailed theoretical analysis based on a three-level system to describe the optical gain properties of polymer nanocomposites. In order to understand the luminescence properties of doped glass at the nano size scale, the doped-glass nanoparticles were made by high-energy wet-ball milling to provide useful guidance for future improvement of the gain properties of nanocomposites.

Chapter 4 describes an algorithm based on a Monte-Carlo method and its application to modelling THz scattering, including the effect of boundaries on the spectral and spatial distribution of THz pulses propagating through highly scattering composite materials. Composite materials were made by forming air bubbles in polycarbonate rods and two different types of 2-D polycarbonate microstructures, and used in experiments.

Chapter 5 describes the measurements of polarisation-dependent diffuse THz scattering in composite materials. It discusses the frequency- and polarisation-dependent spatial distribution and spectrum of THz pulses scattered with off-axis angles from the incident light, as well as the loss characteristics.

Chapter 6 summaries the conclusion of the thesis with recommended future work which can be important for the development of polymer-based optical devices, including planar waveguides, optical fibres, depolarisers, and diffusers.

### 1.7.2 Contributions of This Thesis

- A new method for obtaining optical gain at NIR wavelengths in polymers was proposed based on top-down particle synthesis and it is shown that gain is possible with practical parameters.
- Monte-Carlo modelling of highly scattering composite materials was extended to include boundary effects and it was shown that the boundaries can modify the distribution of EM radiation around scattering objects.
- The latter model was further extended to include polarisation effects off axis and shown to agree with polarisation- and angle-dependent measurements of scattering in highly scattering composite materials.



# 2

## Optical Properties of Polymer Nanocomposite Materials

In this chapter we review and present calculations of the total loss in transmission (i.e. due to absorption plus scattering) as a function of wavelength for nanocomposites with various nano-sized inclusions ( $\text{SiO}_2$ ,  $\text{TiO}_2$ , air [39, 124, 125]). The aim was to determine the practical constraints on particle size and volume fraction, and the associated change in refractive index, and the thermo-optic coefficient achievable in such nanocomposites with limited transmission loss.

### 2.1 Introduction

In the optical properties of composite materials, low loss is usually required if they are to be useful in optical applications. High transparency in polymer nanocomposite materials may be hindered by light scattering, resulting from the refractive-index ( $RI$ ) mismatch between the inclusions and the polymer matrix [39]. Refractive index is an intrinsic material property and, in general, the  $RI$  of inorganic nanofillers is greatly different from that of pure transparent polymers, causing light scattering which can result in opaqueness, even with a low nanoparticle content. However scattering effects

can be minimised by making a trade-off between particle size and refractive mismatch between the host and the inclusion.

The transparency of polymer nanocomposites may also be significantly affected by the absorption loss of the host and/or the inclusion, which restricts the range of useful wavelengths. For example, polymers such as poly(methyl-methacrylate) (PMMA) has strong optical losses caused by C-H and O-H vibrational absorption in the near infrared. The incorporation of the inorganic moiety into a polymer matrix can decrease the C-H and O-H bonding density and thus reduce the absorption loss. Besides, the large polarisability difference between the inclusions and the host moieties possibly induces an increase of the anharmonicity of the C-H and O-H bond, so that the NIR spectra could be shifted into the optical window of the used light [124, 126, 127].

## 2.2 Scattering Regimes

When a photon encounters a particle, a portion of the photon energy is scattered and/or some is absorbed by either the host or the particle. Describing the optical loss (i.e the sum of absorption and scattering) has been the subject of many text books. Here we present a summary of these descriptions in order to identify applicable theories for our modelling and to enable comprehensive analysis using wavelength, volume fraction, and size of particles as parameters.

### 2.2.1 Rayleigh Scattering

A formal solution of Maxwell's equations with appropriate boundary conditions is required to find the scattering amplitude function (i.e. the energy of the scattered wave), and the scattering cross-section (i.e. the total energy scattered in all directions to the area of the particle). Rayleigh scattering describes a type of scattering with large wavelengths and/or particles with size much smaller than the wavelength of the light [40]. The Rayleigh Law describes the transmittance (T) and the scattering cross-section ( $\sigma_s$ ) of the particles, given by:

$$T = \frac{I}{I_0} = \exp \left\{ -\frac{32\pi^2 f L r^3 n_m^4}{\lambda^4} \left[ \frac{(n_p/n_m)^2 - 1}{(n_p/n_m)^2 + 2} \right]^2 \right\} \quad (2.1)$$

$$\sigma_s = \frac{8}{3} \pi k^4 |\alpha|^2 \quad (2.2)$$

in which  $I$  and  $I_0$  are the intensities of the transmitted and incident light,  $r$  the radius of the spherical particles,  $L$  the optical path length, and  $n_m$  and  $n_p$  the refractive index of the matrix and the particles.  $k = 2\pi/\lambda$  is the wave number and  $\alpha$  is the polarisability of a sphere with radius  $r$  and volume fraction, given by:

$$\alpha = \frac{3(m^2 - 1)}{4\pi(m^2 + 2)}f \quad (2.3)$$

in which  $m$  is the refractive index of the particle relative to the host and  $f$  the volume fraction. The Rayleigh law indicates that the scattering of light propagating through composite materials is dependent on a variety of factors including i) the size of the scatterer relative to the wavelength, ii) the volume fraction of the particles, iii) the refractive index of the inclusions.

The large refractive-index mismatch can be compensated for by reducing the radius of the nanoparticles, provided particle agglomeration becomes severe and deteriorates the particle dispersion in the polymer matrix as the particle size decreases. When the size of the particle is very large compared to the wavelength, incident light upon the particle is either refracted into the particle or reflected from the surface. In this case, an area of the incident beam, equal to the geometrical cross-section of the particle, is modified by the particle due to refraction, reflection, and absorption of light. According to the Huygens-Fresnel principle, the total energy extinguished corresponds to a total cross-section of  $\sigma_t = 2\sigma_g$ , where  $\sigma_g$  is the geometrical cross-section of the particle [128].

### 2.2.2 Mie Scattering

Mie theory determines the scattered field and cross-section when the size of the scatterer is comparable to the wavelength of the light. By contrast, Rayleigh scattering is strongly wavelength dependent ( $\lambda^4$ ) and can be extended to scattering from particles with diameters up to one tenth of the wavelength of the light; moreover, the scattering intensity is almost equal in all directions as shown in Fig. 2.1, whereas large particles (Mie regime) scatter the light mostly at small scattering angles, i.e. in the forward direction. The Mie equation solves Maxwell's equations with boundary conditions for the scattering of a homogeneous sphere and can be found in books by Huffman [129] and van de Hulst [130]. The scattering amplitude functions are given by [129]:

$$S_1(\theta) = \sum_{n=1}^{\infty} \frac{2n+1}{n(n+1)} [a_n \pi_n(\cos\theta) + b_n \tau_n(\cos\theta)] \quad (2.4)$$

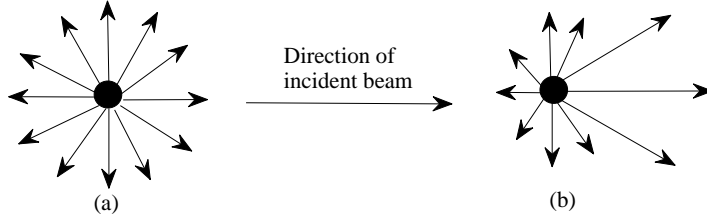


FIGURE 2.1: Scattered photons in (a) Rayleigh, and (b) Mie regimes.

$$S_2(\theta) = \sum_{n=1}^{\infty} \frac{2n+1}{n(n+1)} [b_n \pi_n(\cos\theta) + a_n \tau_n(\cos\theta)] \quad (2.5)$$

where:

$$\pi_n(\cos\theta) = \frac{1}{\sin\theta} P_n^1 \cos\theta \quad (2.6)$$

$$\tau_n(\cos\theta) = \frac{d}{d\theta} P_n^1 \cos\theta \quad (2.7)$$

and  $P_n^1 \cos\theta$  is a Legendre polynomial. As found by Wiscomb, a sufficient number  $n_{max}$  of terms is integer  $(x + x^{1/3} + 1)$  for  $x < 8$ , in which  $x$  is the size parameter, and  $x = ka$  [131]. The complex coefficients  $a_n$  and  $b_n$  are the expansion of the TE and TM modes of the scattered wave given by:

$$a_n = \frac{\Psi'_n(mka)\Psi_n(ka) - m\Psi_n(mka)\Psi'_n(ka)}{\Psi'_n(mka)\zeta_n(ka) - m\Psi_n(mka)\zeta'_n(ka)} \quad (2.8)$$

$$b_n = \frac{m\Psi'_n(mka)\Psi_n(ka) - \Psi_n(mka)\Psi'_n(ka)}{m\Psi'_n(mka)\zeta_n(ka) - \Psi_n(mka)\zeta'_n(ka)} \quad (2.9)$$

where  $m$  is the refractive index of the particles relative to the host ( $m = n_p/n_h$ , here  $n_p$ , and  $n_h$  are refractive index of the particle and host, respectively.). The functions  $\psi_n$  and  $\zeta$  are the spherical Riccati-Bessel functions, given by:

$$\Psi_n(x) = (\pi x/2)^{1/2} J_{n+1/2}(x) \quad (2.10)$$

$$\zeta_n(x) = (\pi x/2)^2 H_{n+1/2}^{(2)}(x) \quad (2.11)$$



where  $J_{n+1/2}$  and  $H_{n+1/2}^{(2)}$  are Bessel functions of the first and second kind, respectively. Using the above equations, the extinction cross-section, i.e. the total scattering and absorption cross-sections,  $\sigma_s$  and  $\sigma_a$  respectively, can be calculated by:

$$\sigma_s = \frac{2\pi}{k^2} \sum_{n=1}^{\infty} (2n+1) (|a_n|^2 + |b_n|^2) \quad (2.12)$$

$$\sigma_{ext} = \sigma_a + \sigma_s = \frac{2\pi}{k^2} \sum_{n=1}^{\infty} (2n+1) \text{Re}(a_n + b_n) \quad (2.13)$$

and the extinction coefficient  $k_{ext}$  ( $\text{cm}^{-1}$ ) can be expressed by:

$$k_{ext} = \sigma_{ext} \frac{f\pi a^2}{V} \quad (2.14)$$

where  $V$  is the volume of particles ( $\text{cm}^3$ ).

### 2.2.3 Multiple Scattering

The transport of waves through random media and/or a composite material is a subject of interest in many applications such as imaging, communication systems, and sensing [132–135]. For example, the transport of light through tissue may be used for disease diagnosis [132]. For our purpose, we are interested in composite materials, including randomly distributed particles with a high volume fraction in order to redistribute the incident wave. Randomly distributed particles in a medium can result in multiple scattering. The transport of light propagating through highly scattering materials can be characterised by three regimes: the diffusion, the absorption, and the ballistic regimes, shown in Fig. 2.2 [136, 137].

For example, Fig. 2.3 shows the transmission as a function of sample thickness along with the three scattering regimes (the model will be explained in Chapter 4). In the ballistic regime, the transmission decays exponentially, i.e. with an exponential attenuation law with a decay constant of the extinction coefficient, because of photons being scattered from the incident light direction. The decay rate defines the scattering mean free path ( $\lambda_s$ ), which is the average distance between scattering events. Diffused light propagating through a slab of length  $L$  undergoes multiple scattering and changes in direction. The contribution of the diffusion regime to the transmitted radiation is governed by a decay rate of  $1/(L + L_0)$  which is much slower than an exponential decay.

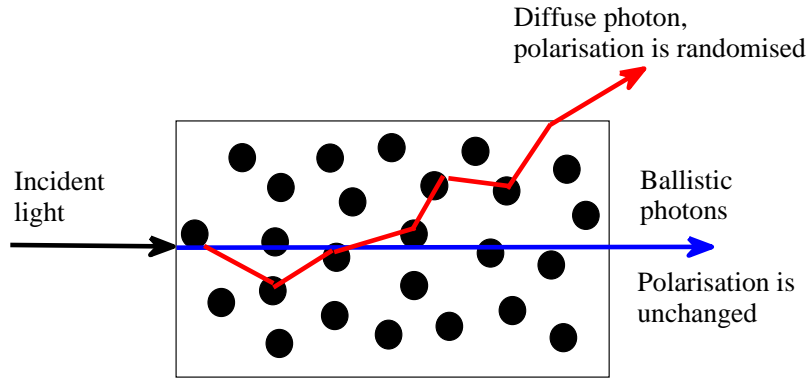


FIGURE 2.2: The types of scattered photon that exit from a highly scattering medium.

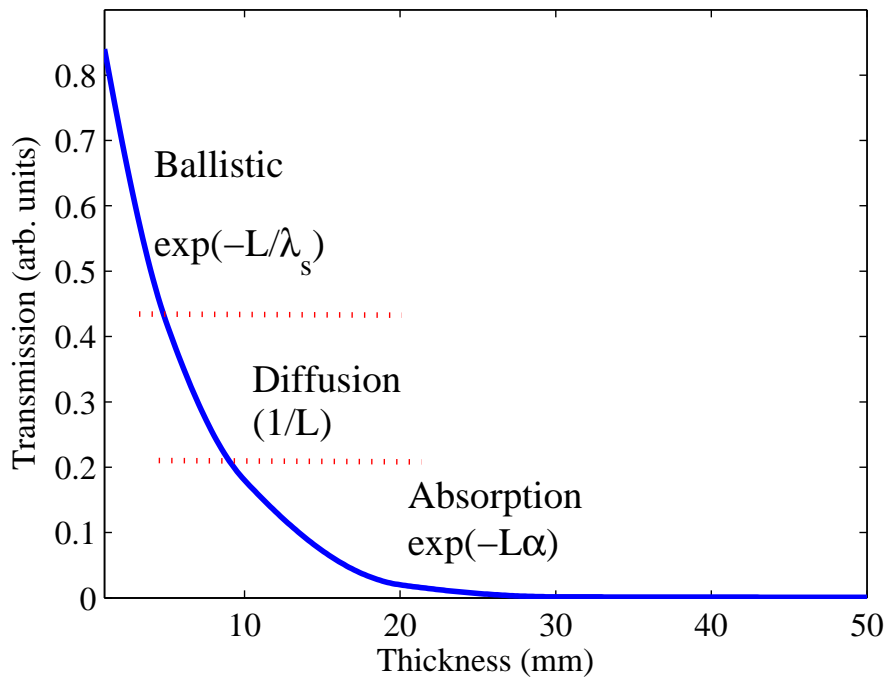


FIGURE 2.3: The transmission of light propagating through a highly scattering medium with length  $L$ , scattering coefficient of  $16 \text{ cm}^{-1}$ , absorption loss of  $1.5 \text{ cm}^{-1}$ .

The diffused component dominates when the sample thickness increases. However, it should be noted that if the wavelength is on the order of the size of the particles then forward scattering predominates. Consequently, the critical parameter is no longer the mean free path, but the transport mean free path (i.e. the distance travelled to leave

the forward direction) which can be given by [138]:

$$\lambda_{tr} = \lambda_s / (1 - \langle \cos(\theta) \rangle) \quad (2.15)$$

where  $\langle \cos(\theta) \rangle$  is the average cosine of the angle of scattering (it will be explained in Chapter 4). After further increasing the thickness, the absorption regime can be encountered, and has an exponential decay of the transmission coefficient. In terms of spherical scatterers, multiple scattering not only differs in transmission characteristics, but also changes the degree of polarisation. Multiple scattering can randomise the polarisation of light as the photons can encounter many scattering events resulting in random transformation of the polarisation.

## 2.3 Effective-Medium Theory

The optical properties of some composite materials can be described by an effective-medium theory. Examples parameters include the refractive index and dielectric behaviour, the conductivity, and the nonlinear response of composite materials. The basic definition of an effective medium is that the extinction coefficient of the composite material should be the same as if it were replaced with a material characterised by the effective dielectric constant, and hence the scattering amplitude should vanish in the forward direction ( $S(0)=0$ ). At  $\theta = 0$  equations (2.4) and (2.5) can be written as series expansions to find the appropriate effective-medium theories (it should be noted that the coefficients  $a_n$  and  $b_n$  are defined differently for different structures and different theories). Two effective-medium theories (EMT) have become particularly popular: the Maxwell-Garnett and Bruggeman theories. They are demonstrated in Fig. 2.4 and described by equations (2.16) and (2.17) [139].

$$\frac{\varepsilon_{eff} - \varepsilon_h}{\varepsilon_{eff} + 2\varepsilon_h} = f \frac{\varepsilon_p - \varepsilon_h}{\varepsilon_p + 2\varepsilon_h} \quad (2.16)$$

$$f \frac{\varepsilon_p - \varepsilon_{eff}}{\varepsilon_p + 2\varepsilon_{eff}} + (1 - f) \frac{\varepsilon_h - \varepsilon_{eff}}{\varepsilon_h + 2\varepsilon_{eff}} = 0 \quad (2.17)$$

where  $\varepsilon_p$  and  $\varepsilon_h$  are the dielectric permeabilities of the particle and the host, respectively.  $\varepsilon_{eff}$  indicates the effective dielectric permeability of a composite material. The effective refractive index can be calculated by  $n_{eff} = \sqrt{\varepsilon_{eff}}$ .

As shown in Fig. 2.4, the Maxwell-Garnett theory assumes a separated-particle structure in which particles are surrounded by a shell, i.e. host materials, so that the average volume fraction corresponds to the volume fraction of the concentric particles. The aggregate structure can be represented by the Bruggeman theory which guarantees the structural equivalence of the two constituents with probability  $f$  of being  $A$  and probability  $1 - f$  of being  $B$ . The latter theories can be affected by the size of particles and a high fill factor (i.e. more than 30%). The reason is that higher-order terms in the expansion series of  $S(0)$  begin to play a role when the particles are much larger than the wavelength and hence the theories can be extended by considering the higher terms in  $S(0)$ .

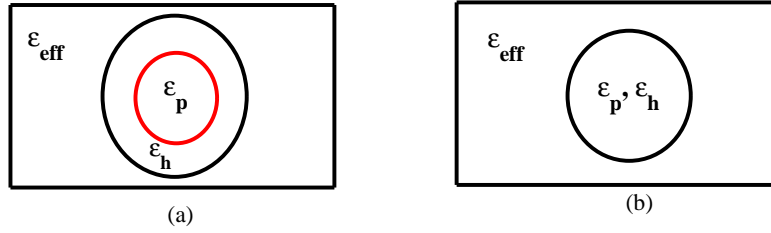


FIGURE 2.4: (a) and (b) depict the corresponding random media used to derive the effective refractive index within the Maxwell-Garnett and Bruggeman theories.

### 2.3.1 Total Differential Effective-Medium Theory

Although effective-medium expressions have been derived in many different ways, it has been also attempted to predict the differential effects of inclusions on a medium. For example, the refractive index of a polymer depends strongly on temperature, i.e. the thermo-optic effect which plays a vital role in device performance. The large thermo-optic effect of polymers enables much lower power consumption in thermo-optic switches (i.e. low switching power) and thus saves energy. On the other hand, it causes a poor of thermal stability in some devices such as waveguide gratings. Whilst silica and many other important materials show an increase in the refractive index, i.e. a positive thermo-optic coefficient, polymers exhibit a lower refractive index at higher temperatures, i.e. a negative thermo-optic coefficient. The availability of materials with opposite thermal behaviour allows for design of thermal properties of optical systems.

We considered differential-equation theory to predict thermo-optic and electro-optic coefficients of nanocomposites. The general form of the effective refractive index is:

$$n_c = F(n_p, n_h, f) \quad (2.18)$$

where  $n_c, n_h, n_i$  are the refractive indices of the composite, host and inclusion, respectively, and  $f$  is the volume fraction of the inclusion. Differentiating equation (2.18) with respect to any applied influence,  $X$ , we obtain:

$$\frac{dn}{dX} = \frac{\partial n_c}{\partial n_h} \cdot \frac{\partial n_h}{\partial n_X} + \frac{\partial n_c}{\partial n_p} \cdot \frac{\partial n_p}{\partial n_X} + \frac{\partial n_c}{\partial n_f} \cdot \frac{\partial n_f}{\partial n_X} \quad (2.19)$$

For the thermo-optic coefficient  $dn/dT$ , changes in volume fraction are taken into account using the coefficients of thermal expansion of both the host and inclusion, giving [140]:

$$\frac{df}{dT} = 3(f - f^2)(\alpha_h - \alpha_i) \quad (2.20)$$

where  $\alpha_h$  and  $\alpha_i$  are the thermal expansions of host and inclusion, respectively. The temperature variation of the refractive index results from the entangled change in polarisability of the electron cloud and the density of the material. The model here assumes that the materials do not undergo any phase changes, and neglects the effects of stress. This is applicable to inorganic inclusions in a polymer host operating below their glass transition temperature.

## 2.4 Prediction of Optical Properties of Composite Materials

We separately calculated the extinction coefficient ( $K_{ext}$ ) for spherical particles of  $\text{TiO}_2$ , air-bubbles, and  $\text{SiO}_2$  in PMMA as a function of wavelength, particle size, and volume fraction. For example, Fig. 2.5 (glass in PMMA) clearly shows that a smaller volume fraction and smaller particle size lead to lower loss. Figs 2.6-2.8 highlight the differences between the different nanocomposites studied to date, and the range of parameters which results in materials with usefully low loss. From Fig. 2.6 we see that  $\text{TiO}_2$  nanoparticles in PMMA with a volume fraction of less than 20% ensure an extinction coefficient of less than  $1 \text{ cm}^{-1}$  at wavelengths of interest. The rapid reduction in loss

with increasing wavelength in the visible region is due to reduced scattering. Loss then increases again at longer wavelengths due to absorption, e.g. on reaching a maximum value  $K_{ext}$  is  $1.8 \text{ cm}^{-1}$  when  $\lambda = 1200 \text{ nm}$  and  $f = 20\%$ .

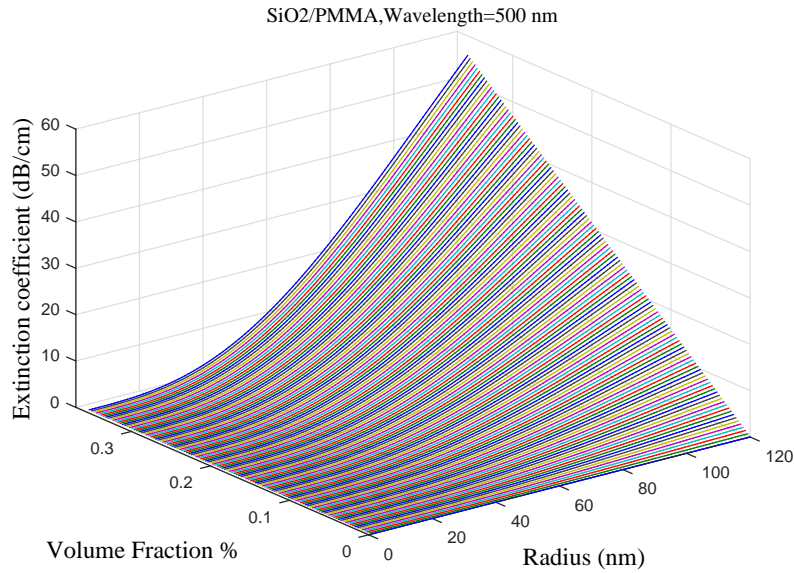


FIGURE 2.5: Optical loss for glass nanoparticles embedded in PMMA vs particle size and volume fraction at  $\lambda=1350 \text{ nm}$ .

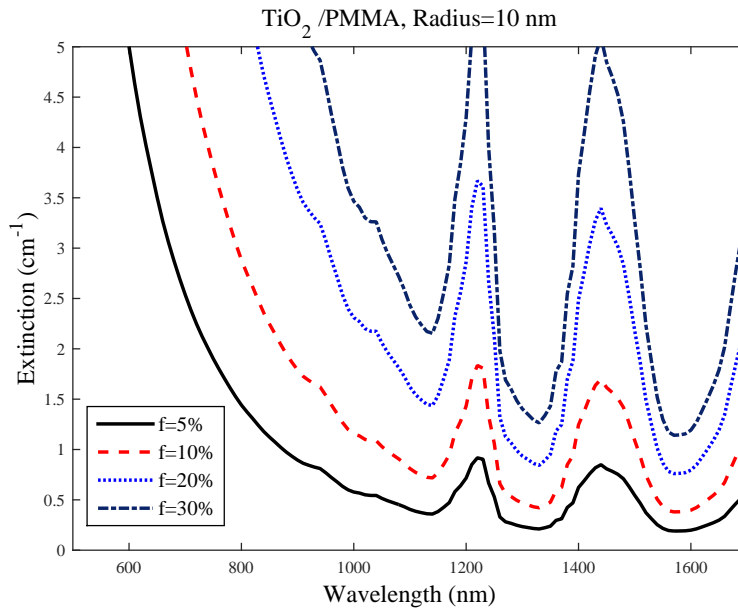


FIGURE 2.6: Extinction coefficient spectrum for nanocomposite with 20 nm diameter titanium dioxide particles in PMMA for various volume fractions.

Fig. 2.7 provides the spectral dependence of the extinction coefficient of air bubbles in PMMA; the loss is generally lower than in the  $\text{TiO}_2$  nanocomposite. For example, for the same size and volume fraction of inclusions  $K_{ext}$  is  $0.98 \text{ cm}^{-1}$  when  $\lambda = 1220 \text{ nm}$ . This difference is due to smaller refractive index mismatch between the PMMA host and air inclusions than is the case for  $\text{TiO}_2$ .

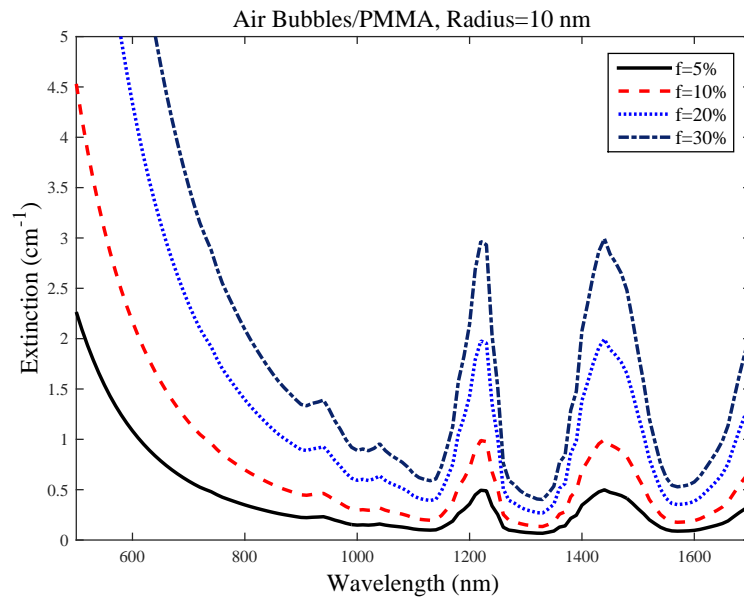


FIGURE 2.7: Extinction coefficient spectrum of nanocomposite with 20 nm diameter air bubbles in PMMA for various volume fractions.

Fig. 2.8 shows the extinction coefficient of glass nanoparticles in PMMA. For the same particle size as in the previous two examples, the scattering losses of  $\text{SiO}_2$  in PMMA are significantly lower, due to the much smaller difference in refractive index between host and inclusion, and host absorption makes a more significant contribution to the total loss. Fig. 2.9 shows the transmission spectra of a glass-PMMA nanocomposite for various particle sizes with a 10% volume fraction. The latter calculations were repeated over a range of particle sizes and volume fractions to identify limiting values of the inclusion parameters resulting in nanocomposites with useful optical properties with transmittance of at least  $80 \text{ cm}^{-1}$ . The results are summarised below in Table 2.1.

Some studies have shown the relation between the refractive index and volume fraction of inclusions [141, 142]. Fig. 2.10 shows a comparison between Maxwell-Garnett

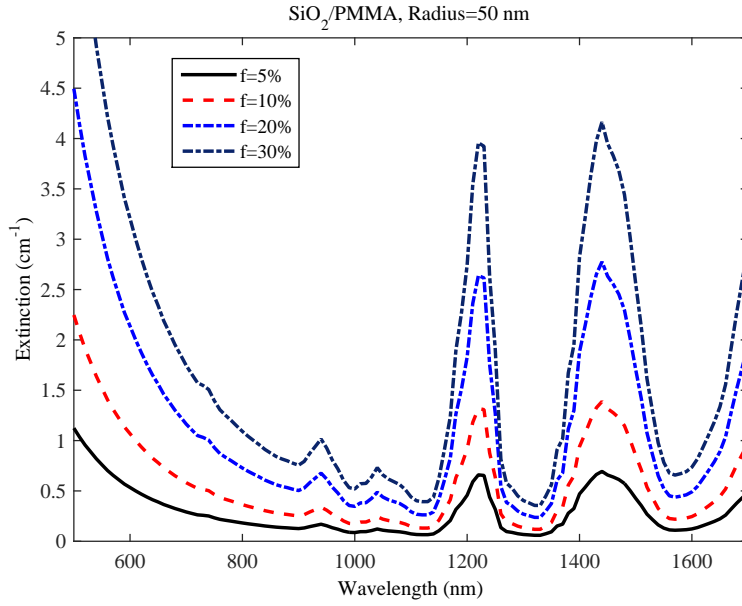


FIGURE 2.8: Extinction coefficient spectrum of nanocomposite with 20 nm diameter glass particles in PMMA for various volume fractions.

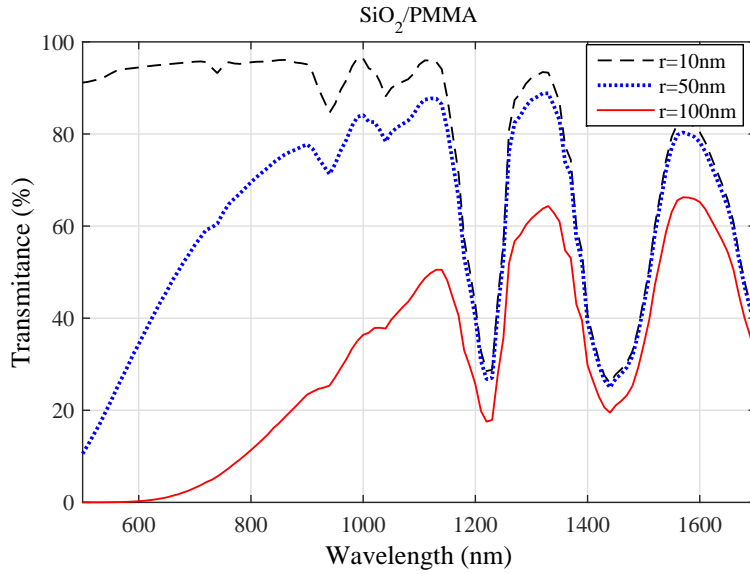


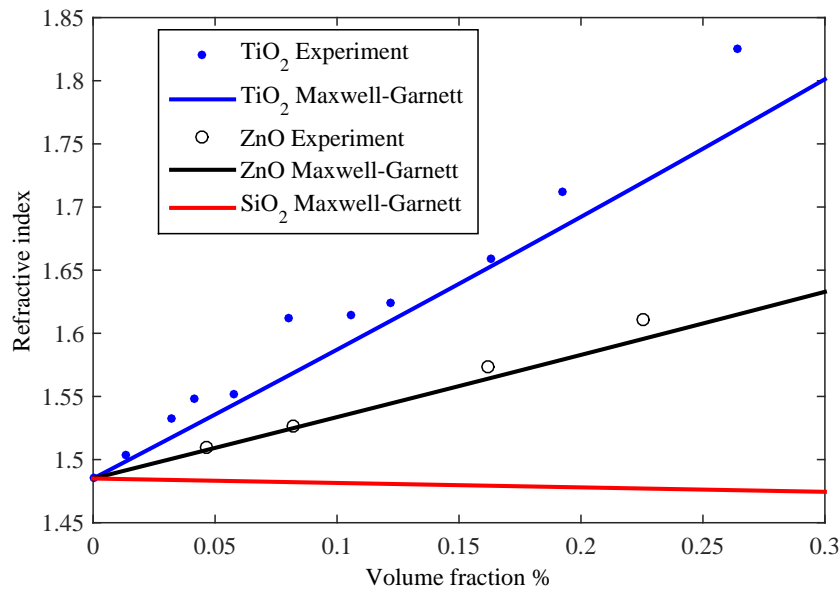
FIGURE 2.9: Transmission spectra through 1 cm of PMMA-SiO<sub>2</sub> nanocomposite with 10% SiO<sub>2</sub> by volume.

and previous studies to verify our prediction for SiO<sub>2</sub> refractive indices [143, 144]. TiO<sub>2</sub> nanocomposites have a higher effective index than a PMMA host, whilst glass reduces the effective index. The range of volume fraction achievable with limited loss depends on the refractive index of the inclusion and the particle size, as demonstrated above.



TABLE 2.1: Limiting values for polymer nanocomposites with 80%  $\text{cm}^{-1}$  transmittance.

Inclusions	Limiting Values for Inclusions		
	$f$	$r$ (nm)	$\lambda$ (nm)
$\text{SiO}_2$	10%	10-50	800-1140, 1270-1350, 1570
$\text{TiO}_2$	5%	$< 10\%$	1330, 1580
Air-bubbles	5%	$< 10\%$	900-1180, 1250-1380, 1520-1670

FIGURE 2.10: Comparison between Maxwell-Garnett and measured refractive index of different nanoparticles ( $\text{SiO}_2$ ,  $\text{ZnO}$ , and  $\text{TiO}_2$  with 50 nm, 25 nm, and 30 nm in radius) embedded in PMMA vs volume fraction at  $\lambda=750$  nm.

Consequently the maximum change in effective refractive index that can be realised with minimal loss, even with relatively small inclusions, is limited to volume fractions of less than approximately 10%. Hence polymer nanocomposites may have their refractive index changed by up to approximately 3% before scattering losses significantly limit the transmittance. To investigate the accuracy of our calculations, we compared experimental results [145] with the simulations shown in Fig. 2.11. The results show that the theoretical values are in good agreement with the experimental values, except that the predicted absorption spectrum of PMMA/ $\text{TiO}_2$  is slightly different from its experimental value.

The effective index of the nanocomposites studied was typically limited to the range 1.43-1.58, with a relative index change of up to 3%. The predicted thermo-optic coefficient of some composites with a PMMA host is shown as a function of volume

fraction in Fig. 2.12. Note that, although the thermo-optic coefficient of a 90:10 glass:PMMA composite would theoretically be zero, it would be difficult to realise such a large volume fraction in practice.

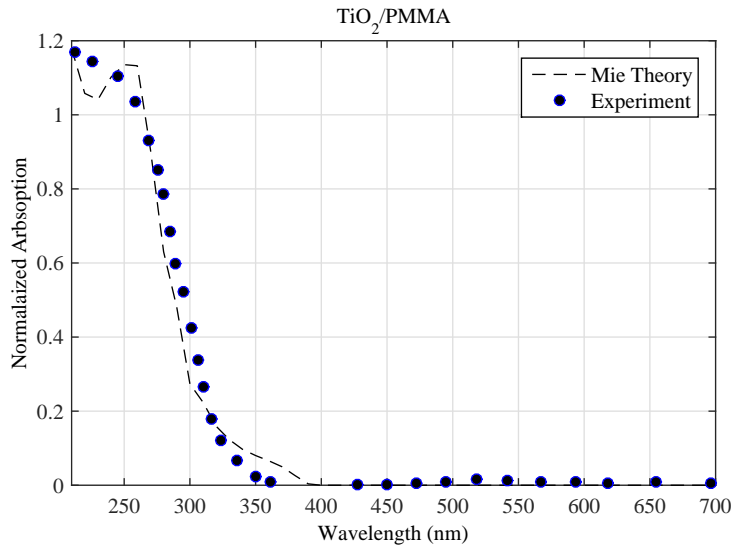


FIGURE 2.11: Comparison between Mie theory and measured absorption of  $\text{TiO}_2$  nanoparticles embedded in PMMA with 30% volume fraction.

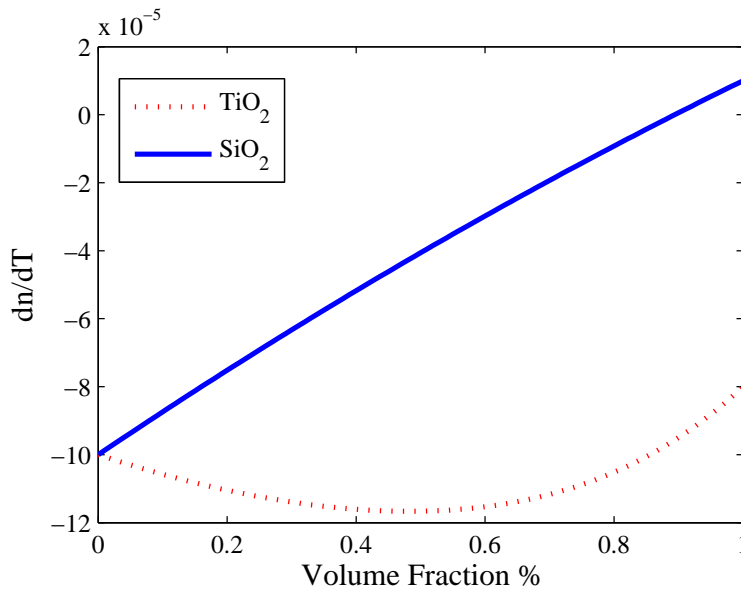


FIGURE 2.12: The dependence of  $\text{dn/dT}$  on volume fraction in  $\text{TiO}_2/\text{PMMA}$  and  $\text{SiO}_2/\text{PMMA}$ .

## 2.5 Summary

The optical loss coefficient and effective refractive index of three different polymer nanocomposites have been calculated using Mie theory and Maxwell-Garnett theory, respectively. Calculations were performed for a wide range of parameter values to assess suitable and/or limiting parameter values for the inclusions to keep loss within useful limits whilst also maximising the change in effective refractive index of the nanocomposite relative to the host material. Scattering losses were found to dominate the total loss coefficient, except for glass-polymer composites in which the polymer absorption dominated the loss. It was also found that to ensure 80%  $\text{cm}^{-1}$  transmittance at wavelengths of interest required inclusions smaller than 10 nm (or 50 nm for silica), and/or volume fractions less than 5% (or 10% for silica). Consequently the effective index of the nanocomposites studied was typically limited to the range 1.43-1.58, with a relative index change of up to 3%.



# 3

## Optical Gain in Polymer Nanocomposites

In this chapter we report the results of extensive numerical investigations in which the total small-signal optical gain of the nanocomposite material (i.e. Er/Yb-doped glass nanoparticles dispersed in PMMA) was calculated as a function of distance for a variety of launched pump intensities. In particular, we identify the optimal device length to maximise the optical gain in nanocomposites with practically feasible parameters.

### 3.1 Introduction

Polymer-based devices are potentially important and useful components in integrated optical applications, with many applications in optical communications and sensing at around  $1.5\ \mu\text{m}$  [146]. Although many polymers are attractive candidates for fabrication of optical devices because of their advantageous material properties - such as ease of processing, tunability and low cost-, they suffer from loss at  $\lambda = 1.5\ \mu\text{m}$  which is significantly larger than glass-based devices. Thus, some improvements through the optimisation of polymer-based materials are deemed necessary to lower the limit for optical losses, for example, by introducing optical gain into the polymer.

Whilst developments continue to be made on optical materials based on rare-earth doped inorganic materials, such as silica and ceramics [88, 147–149], there has been

relatively little progress on solution-processible organic-inorganic hybrid materials for optical amplifiers, such as rare-earth doped polymers [97, 149]. The primary problem is how to incorporate the rare-earth ions into organic hosts. Compared to inorganic host materials, there are two key obstacles to the development of optical amplifiers based on polymers: (i) it is relatively difficult to dissolve the rare-earth ions into polymers as they come in the form of inorganic salts, and (ii) hydrogen groups in the polymer partly quench the radiative transitions of rare-earth ions at around  $1.5\ \mu\text{m}$  [11, 150].

A variety of organic-inorganic hybrid materials have been investigated in attempts to incorporate rare-earth ions into polymer whilst minimising quenching interactions [97], including encapsulating the rare-earth ions in a poly-dentate cage-like complexes [150], or embedding the ions in colloidal silica [11]. Rare-earth doped sol-gel materials showed some early promise and planar waveguides with optical gain were demonstrated [151, 152]. Waveguide amplifiers incorporating rare-earth organic complexes and fabricated by solution processing have also been reported [96, 153, 154]. More recently optical amplifiers fabricated from doped nano-crystals dispersed in sol-gel or polymer have been coming to the fore [84, 87, 95, 155–158]. For example, Zhao *et al.* reported an optical gain of 10.4 dB gain in an 11 mm long SU-8 waveguide containing Er:Yb-doped BaYF nano-crystals [84].

In the latter approaches the doped nano-crystals were chemically synthesized, and hence were quite small (typically 10 nm in diameter), offering a relatively large surface-to-volume ratio for a given concentration of dopant ions. Here we propose a potentially simpler approach which is to break down bulk glass with a high concentration of rare-earth ions and then disperse the resulting nano-particles (typically 100 nm in diameter) into the polymer in solution before standard wet-processing and printing to fabricate thin-film waveguides for optical amplifiers.

As in the doped nano-crystals, the doped glass nano-particles serve to isolate the rare-earth dopants from the polymer host, however the larger nano-particles produced by top-down processing will offer a lower surface-to-volume ratio. Consequently, when the glass nano-particles are dispersed into the polymer host a lower proportion of the rare-earth ions will be exposed to quenching by the polymer, but on the other hand the larger particles may increase scattering losses within the composite.

In calculating the optical gain achievable in such materials one must therefore take into account not only the concentration of rare-earth ions in the particles and their volume fraction within the polymer host, together with the absorption loss of the host at both pump and signal wavelengths, but also the size and refractive index of the nano-particles and associated scattering losses.

Furthermore, it should be recognised that the scattering losses will affect the pump and signal wavelengths quite differently; scattering is strongly dependent on the refractive index mismatch between the inclusions and the host, and on the size of the nano-particles relative to wavelength. Lastly, the material parameters will often be constrained in practice (e.g. minimum particle size, maximum volume fraction), raising the question of whether optical gain is even possible in a given length of material with realisable dopant concentration, particle size, volume fraction of inclusions, and pump power.

## 3.2 Interaction of Light and Matter

When matter is exposed to light, in principle, the interaction may yield either radiative or non-radiative processes, depending on whether the light encounters a single ion and/or between two or more ions, the structure of the matter, and on the wavelength of the light. In the case of radiation, interaction occurs via absorption or emission processes, while the non-radiative process describes a phonon-assisted transition.

### 3.2.1 Basic Mechanisms of Rare-Earth Ions

#### 3.2.1.1 Spontaneous and Stimulated Emissions

In the rare-earth ions, a number of energy states is included in the  $4f^N$  configuration with the ground states (the lowest energy level) and excited states (higher energy states). The  $4f^N$  level is split into many sublevels due to atomic interaction and a crystal field environment, shown in Fig. 3.1 [10, 159]. The working principle of optical amplifiers is based on population inversion, in which the number of electrons in the higher energy level is more than the number of electrons in the terminal state. When a photon is absorbed by an ion, electrons are excited to a higher energy level. Afterwards two processes can happen: (i) they can release their energy and relax to the ground states automatically, called spontaneous emission, (ii) another photon forces excited electrons to relax to the terminal state, resulting in releasing another photon with the same energy as the passing photon, known as stimulated emission. These processes are shown in Fig. 3.2.

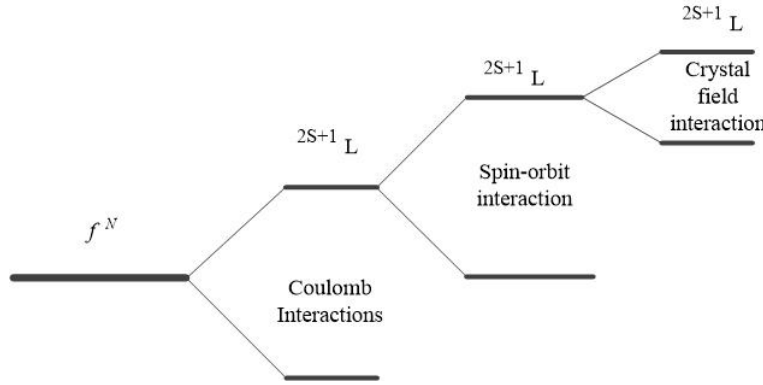


FIGURE 3.1: Schematic of the energy state of  $4f^N$  electrons.  $S$  is the total spin angular momentum of all electrons in the system, and  $L$  is the total orbital angular momentum.

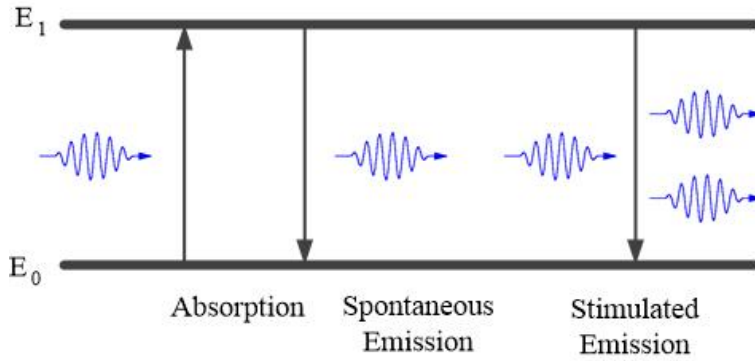


FIGURE 3.2: Absorption, spontaneous, and stimulated emission.

### 3.2.1.2 Radiative Transfer

Rare earth ions are classified into two groups on the periodic table: lanthanides (elements 57-71) and actinides (elements 89-103). Their optical properties (e.g. luminescence properties) are characterised by the partially filled  $4f$  shell which is well shielded by the  $5s^2$  and  $5p^6$  orbitals. Using optical pumping, the ions are excited to a higher level energy and hence a large number of transitions between the different energy levels is possible. The electrons in the  $4f$  levels can only be excited inside the  $4f$  states and they weakly interact with the electrons in other ions due to the parity selection rule; the energy levels of the  $4f$  shell have equal parity and electric dipole transitions are forbidden. The  $f$ - $f$  transitions yield sharp lines in the optical spectra. Table 3.1 provides the luminescence wavelength of different rare-earth ions.

The characterisation of ions with a  $4f$  configuration is based on the transition probabilities which related to the Judd-Ofelt intensity parameters ( $\Omega_2$ ,  $\Omega_4$ ,  $\Omega_6$ ). The Judd-Ofelt theory can be used to calculate and predict the oscillator strength for each



TABLE 3.1: Luminescence wavelengths of rare-earth ions.

Rare-earth ions	Radiative transition	Luminescence wavelength (nm)
Er <sup>3+</sup>	$^4I_{13/2} \rightarrow ^4I_{15/2}$	1550
Yb <sup>3+</sup>	$^2F_{5/2} \rightarrow ^2F_{7/2}$	1020
Tm <sup>3+</sup>	$^3H_4 \rightarrow ^3H_6$	1900
Nd <sup>3+</sup>	$^4F_{3/2} \rightarrow ^4F_{9/2}$ , $^4F_{3/2} \rightarrow ^4I_{11/2}$ , $^4F_{3/2} \rightarrow ^4I_{13/2}$	880, 1060, 1330
Eu <sup>3+</sup>	$^5D_1 \rightarrow ^7F_3$	615

transition as follows [160, 161]:

$$f = \frac{4\varepsilon_0 mc^2}{3h n^2 e^2 \lambda (2J + 1)} (\chi_{ed} S_{ed} + \chi_{md} S_{md}) \quad (3.1)$$

where  $S_{ed}$  and  $S_{em}$  are the strengths of the electric dipole and magnetic dipole transitions, and  $\chi_{ed} = n(n^2 + 2)^2/9$  and  $\chi_{md} = n^3$ .  $c$  is the velocity of light,  $e$  and  $m$  charge and mass of electrons,  $h$  Planck's constant,  $J$  the angular momentum,  $N_0$  the density of ions, and  $n$  the refractive index of the host materials. The electric dipole and magnetic dipole transitions are defined as [162, 163]:

$$S_{ed} = e^2 \sum_{t=2,4,6} \Omega_t \left| \langle \alpha \| U^{(t)} \| b \rangle \right|^2 \quad (3.2)$$

$$S_{md} = \left( \frac{eh}{4\pi mc} \right)^2 \left| \langle \alpha \| L + 2S \| b \rangle \right|^2$$

Using Weber [164] the reduced matrix ( $\left| \langle \alpha \| U^{(t)} \| b \rangle \right|^2$ ) can be calculated.  $\left| \langle \alpha \| L + 2S \| b \rangle \right|^2$  can be determined by Carnall [165]. The experimental strength of the band can be calculated using the integrated absorption cross-section of the transition between different states using the following equation:

$$S_{meas} = \frac{27chn(2J+1)}{8\pi^3 \lambda e^2 N_0 (n^2 + 2)^2} \int \alpha(\lambda) d\lambda \quad (3.3)$$

where  $\alpha$  is the absorption coefficient at a wavelength of  $\lambda$ . Combining  $S_{meas}$  and

equations 3.3 and 3.2, the intensity parameters can be obtained. From S, the individual radiative transition rate from the excited state ( $J'$ ) to state ( $J$ ) can be expressed as follows:

$$A(J' \rightarrow J) = \frac{16\pi^3}{3\varepsilon_0 h \lambda^3 (2J' + 1)} (\chi_{ed} S_{ed} + \chi_{md} S_{md}) \quad (3.4)$$

The radiative time life is given by:

$$\tau_{rad} = \frac{1}{A(\sum J' \rightarrow J)} \quad (3.5)$$

The fluorescence branching ratio can be expressed by:

$$\beta = A(J' \rightarrow J) \tau_{rad} \quad (3.6)$$

### 3.2.1.3 Non-Radiative Transfer

In a non-radiative process, rare-earth electrons relax to the next lower lying level by emitting multiple phonons, which is an undesirable process for application as amplifiers. Radiative transitions are sensitive to the host materials due to  $f - f$  transitions; rare-earth ions can interact with vibration of the host material, resulting to emission of phonons. A non-radiative process includes ion-ion interactions and multi-phonon emission depending on the number of phonons required to bridge the energy gap. In the case of phonon emission, multiphonon relaxation theory can be given for both glasses and crystals as follows [10]:

$$W_{mp} = B(n(T) + 1)^p \exp(-\alpha \Delta E) \quad (3.7)$$

and

$$n(T) = \frac{1}{\exp(h\omega/kT) - 1} \quad (3.8)$$

where B is the Bose-Einstein occupation number,  $\Delta E$  the energy gap between two electronic states,  $\alpha = -\ln/\hbar\gamma$  is correlated with the coupling constant with interaction  $\gamma$ .  $\hbar$  is the reduced Planck constant,  $h/2\pi$ , K Boltzmann constant,  $\omega$  the phonon angular frequency. p is the phonon number required to bridge the energy gap, given by:

$$p = \frac{\Delta E}{h\omega} \quad (3.9)$$

In practice,  $p$  and  $\alpha$  are usually used to describe non-radiative decay and can be obtained by fitting equation 3.7 to experimental data for variety of measurements. The ion-ion interactions also reduce the quantum efficiency (i.e. the ratio of radiative to non-radiative transitions) of amplifiers which depend on rare-earth ion concentrations and energy transfer between the same rare-earth ions or different ions. The energy transfer between the same types of rare-earth ions is expressed as cross-relaxation process. In this case, an excited ion transfers a proportion of its energy to a nearby ion and then relaxes to a lower level, followed by a decay to the ground state nonradiatively (shown in Fig. 3.3).

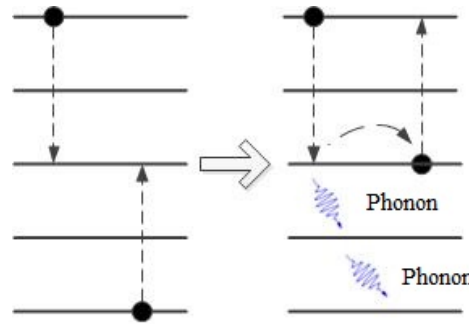


FIGURE 3.3: Schematic of the cross-relaxation process.

#### 3.2.1.4 Upconversion

Besides the transitions between energy levels due to absorption and stimulated emission, two or more photons can be absorbed sequentially rather than simultaneously. Electron is excited to a higher level and a second photon then promotes it to an even higher level. Therefore, it can lead to the emission of photon at shorter wavelength than the excitation wavelength. This process is defined as upconversion, shown in Fig. 3.4.

#### 3.2.1.5 Quenching

Quenching in amplifiers is associated with different factors including: (a) energy transfer between ions as a result of high rare-earth ion concentrations, particularly when

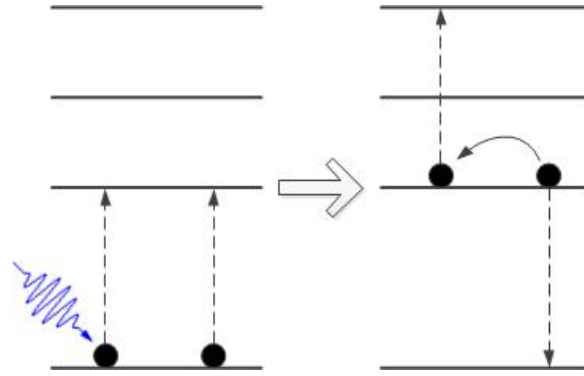


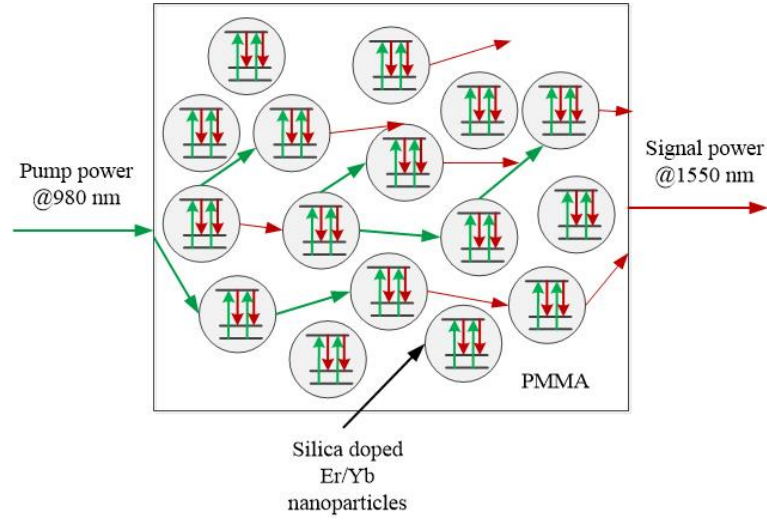
FIGURE 3.4: The schematic of the up-conversion process.

clustering of ions occurs, (b) temperature quenching caused by multiphonon transition to lower electronic levels, (c) quenching process resulting from host molecules such as C-H and O-H groups. To reduce the quenching process at high concentration, rare-earth ions should be isolated properly from each other.

### 3.3 Rare-Earth Ion Doped Polymer Amplifiers

Photon absorption and emission cross-sections of a medium are dependent on the host material in which the rare-earth ions are doped, and mainly dependent on the rare-earth ions. Among various rare-earth ions,  $\text{Er}^{3+}$  and  $\text{Yb}^{3+}$  ions have high absorption and emission at 1550 nm and 980 nm, respectively, making them one of the most promising active dopants for optical amplifiers in telecommunication systems. As shown in Fig. 3.5, the proposed nanocomposite material has the advantage of glass as a host for the rare-earth ions and the polymer as a host for phosphate glass. In order for the amplification, erbium-ytterbium ions are suitable active dopants for the optical amplifiers as erbium ions provide emission at around  $1.5 \mu\text{m}$  and ytterbium ions increase pump absorption and allow the absorbed energy to be transferred to erbium ions. In this work, we focus on PMMA as a host material because the refractive index of phosphate glass is close to PMMA. Consequently, a higher rare-earth concentration can be achieved by larger nanoparticles with small changes in the scattering loss. Mie theory was used to calculate the scattering and absorption cross-sections, and hence optical extinction of the glass nanoparticles in PMMA as a function of wavelength and fill factor [129].

In the theoretical description of optical amplification of  $\text{P}_2\text{O}_5:\text{Er}^{3+}/\text{Yb}^{3+}$  in PMMA, a model of the Er/Yb system was used to calculate the pump and signal evolution along the direction of propagation, taking into account scattering and absorption by the host

FIGURE 3.5:  $\text{P}_2\text{O}_5:\text{Er}^{3+}/\text{Yb}^{3+}$  nanoparticle-doped PMMA.

and doped particle inclusions at both the pump and signal wavelengths. We use 3-level rate equation model, which  $\text{Yb}^{3+}$  ions on the level  $^2\text{F}_{7/2}$  absorb the energy of the pump and transit up to the excited level  $^2\text{F}_{5/2}$ , and then quickly transfer their energy to nearby  $\text{Er}^{3+}$  ions on the fundamental level  $^4\text{I}_{15/2}$  to promote them to excited level  $^4\text{I}_{11/2}$ . Since this excited level  $^4\text{I}_{11/2}$  is unsteady,  $\text{Er}^{3+}$  ions decay to the metastable level  $^4\text{I}_{13/2}$ . We neglect back transfer process from erbium to ytterbium ions due to very small life time of the  $^4\text{I}_{11/2}$  and the channel for energy transfer is the one where an excited electron in  $\text{Yb}^{3+}$  gives its energy to an electron in the ground state of  $\text{Er}^{3+}$ . Energy-level diagram of the Yb-Er is shown in Fig. 3.6.

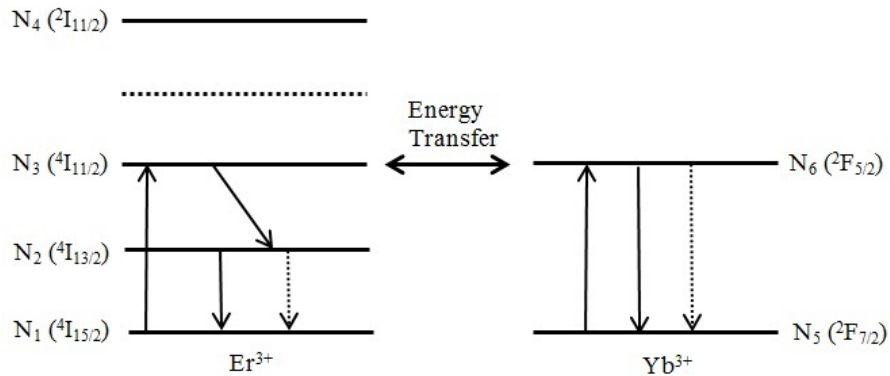


FIGURE 3.6: Energy scheme of Er and Yb ions; arrows with dotted line indicate spontaneous emission.

On the basis of the energy level diagram, the rate equations for  $\text{Er}^{3+}$  and  $\text{Yb}^{3+}$

population densities are given by [166–169]:

$$\frac{\partial n_1}{\partial t} = -W_{12}n_1 - W_{13}n_1 + A_{21}n_2 + W_{21}n_2 - C_{cr}n_1n_4 - C_{cr}n_1n_6 + C_{up}n_2^2 + C_{up}n_3^2 \quad (3.10)$$

$$\frac{\partial n_2}{\partial t} = W_{12}n_1 - A_{21}n_2 - W_{21}n_2 + A_{32}n_3 + 2C_{cr}n_1n_4 - 2C_{up}n_2^2 \quad (3.11)$$

$$\frac{\partial n_3}{\partial t} = W_{13}n_1 - A_{32}n_3 + A_{43}n_4 + C_{cr}n_1n_6 \quad (3.12)$$

$$n_1 + n_2 + n_3 + n_4 = N_{Er} \quad (3.13)$$

$$\frac{\partial n_4}{\partial t} = W_{56}n_5 - A_{65}n_6 + W_{65}n_6 + C_{cr}n_1n_6 \quad (3.14)$$

$$n_5 + n_6 = N_{Yb} \quad (3.15)$$

$$W_{ij} = \frac{\sigma_{ij}}{h\nu_{s,p}A_{eff}}P_{s,p} \quad (3.16)$$

where  $n_1$ ,  $n_2$ ,  $n_3$ , and  $n_4$  are the population of  $\text{Er}^{3+}$  levels  $^4\text{I}_{15/2}$ ,  $^4\text{I}_{13/2}$ ,  $^4\text{I}_{11/2}$ , and  $^4\text{I}_{9/2}$ , respectively, and  $n_5$ ,  $n_6$  the population  $\text{Yb}^{3+}$  levels  $^2\text{F}_{7/2}$  and  $^2\text{F}_{5/2}$ , respectively. The  $W_{ij}$  terms represent stimulated transition rates between level  $i$  and  $j$ ,  $A_{21}$  and  $A_{56}$  are spontaneous transition rates,  $A_{32}$  and  $A_{65}$  nonradiative relaxation rates,  $C_{cr}$  the cross-relaxation coefficient governing the energy transfer between  $\text{Er}^{3+}/\text{Yb}^{3+}$ ,  $N_{Er}$  and  $N_{Yb}$  erbium and ytterbium concentrations, and  $h$  Planck's constant.  $\sigma_{ij}$  is the pump absorption cross-section or the signal absorption and emission cross-sections.  $A_{eff}$  is the effective area, and  $P_{s,p}$  represents the signal and pump powers, respectively. The intensity can be defined as:

$$I_{p,s} = \frac{P_{s,p}}{A_{eff}} \quad (3.17)$$

in which  $I_p$  and  $I_s$  are the pump and signal power intensities. Table 3.2 lists the parameters used in the optical gain/loss calculation in the nanocomposite polymer amplifiers [170, 171]. The following coupled signal and pump differential equations are

TABLE 3.2: Parameters used in the optical gain calculation for the  $P_2O_5:Er^{3+}/Yb^{3+}$ /PMMA nanocomposite optical amplifier.

Emission and Absorption Cross Sections	$\sigma_{Er21}(\lambda_s = 1550 \text{ nm}) = 9 \times 10^{-25} \text{ m}^2$ $\sigma_{Er12}(\lambda_s = 1550 \text{ nm}) = 6.5 \times 10^{-25} \text{ m}^2$ $\sigma_{Er13}(\lambda_p = 980 \text{ nm}) = 2.58 \times 10^{-25} \text{ m}^2$ $\sigma_{Yb56}(\lambda_p = 980 \text{ nm}) = 1 \times 10^{-25} \text{ m}^2$
Cross Relaxation	$C_{cr} = 0.7 \times 10^{-22} \text{ m}^3 \text{ s}^{-1}$
Upconversion Coefficients	$C_{up} = 1 \times 10^{-22} \text{ m}^3 \text{ s}^{-1}$
Lifetime	$\tau_{21} = 10 \times 10^{-3} \text{ ms}$ , $\tau_{65} = 2 \times 10^{-3} \text{ ms}$

numerically integrated through a Runge-Kutta algorithm:

$$\frac{dp_p}{dz} = -p_p (\sigma_{Er13} n_1 + \sigma_{Yb56} n_5) - \alpha_p p_p \quad (3.18)$$

$$\frac{dp_s}{dz} = -p_s (\sigma_{Er13} n_2 + \sigma_{Er12} n_1) - \alpha_s p_s \quad (3.19)$$

Finally, equation 3.19 can be defined in terms of the normalized signal gain,  $s(z)=P_s(z)/P_s(0)$  (here  $P_s(0)$  is the launched signal power), and the gain function along the direction of propagation can be expressed as:

$$\frac{dg(z)}{dz} = -\alpha_s - (n_1)\sigma_{Er12} + n_2\sigma_{Er21} \quad (3.20)$$

The gain calculated using equation 3.20 determines the signal gain, according to  $g(z)=\ln[s(z)]$ , here  $s(z)$  is the signal gain.

A flow chart of optimisation of optical amplification in polymer nanocomposites is shown in Fig. 3.16.

### 3.3.0.6 Synthesis of Phosphate Glass Doped Nanoparticles

Synthesise of specific nanoparticles, in particular, doped inclusions by a simple and low cost has been a great challenge. Various bottom-up approaches, such as sol-gel process, have been developed. In our experiment, we used a high energy ball mill, i.e.

a top-down approach, to break highly doped glass into nanoparticles with mean radius of 50 nm. The final size of nanoparticles depends on the size and size distribution of the balls, dry or wet milling and the duration of milling. For example, dense packing of balls reduces the mean free path of the ball motion, resulting in maximising collision frequency. The bulk commercial available phosphate glass doped rare-earth [172] ions was first milled in a ball mill with a stainless steel ball of 2 cm in diameter at 200 rpm milling speed for 10 min to make the powder with size of 1 micron. Doped  $P_2O_5$  powder and distilled water were sealed in a stainless steel vial with balls to mixture weight ratio of 25:1. For the optimisation of the milling conditions, the size of stainless steel balls was varied between 5 mm and 1 mm, and the rotation speed varied between 400 and 600 rpm, depending on the size of balls. The ball milling process was carried out for 40 hours, running for 5 minutes followed by 2 minutes break. After milling, the color of them changed from white into green as shown in Fig. 3.7. We also replaced water with ethanol as ball-milling dispersant for the surface functionalisation of the nanoparticles using monomers such as MPTS.



FIGURE 3.7: Synthesis process of doped glass nanoparticles.

The average particle size was measured by Dynamic Light Scattering system (DLS) using nano-Zetasizer at 25°C under a scattering angle of 175° at the wavelength of 633 nm. Fig. 3.8 shows a wide size distribution with a proportion of particles over 100 nm; the maximum density of particles with a size of less than 100 nm is around 20%. To purify the nanoparticles, the dispersion diluted with distilled water and centrifuged at 4000 rpm for 1 hour. Then the solution was passed through a 0.1  $\mu\text{m}$  filter to separate nanoparticles with diameter in the range of 70-100 nm. Although Fig. 3.9 shows that the particles aggregated, they can be well dispersed in monomer using high-energy ball milling and/or using ultrasonic bath.



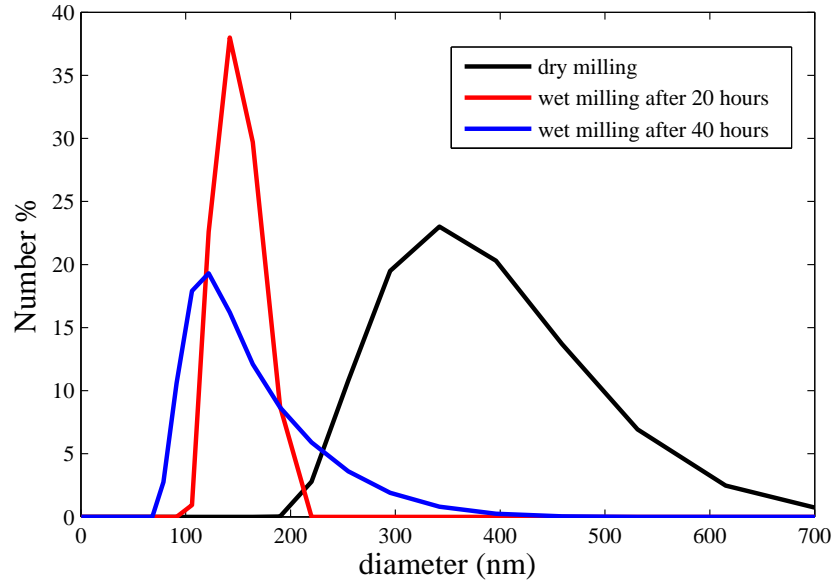


FIGURE 3.8: Size distribution of doped-glass nanoparticles into distilled water, measured using Zetasizer.

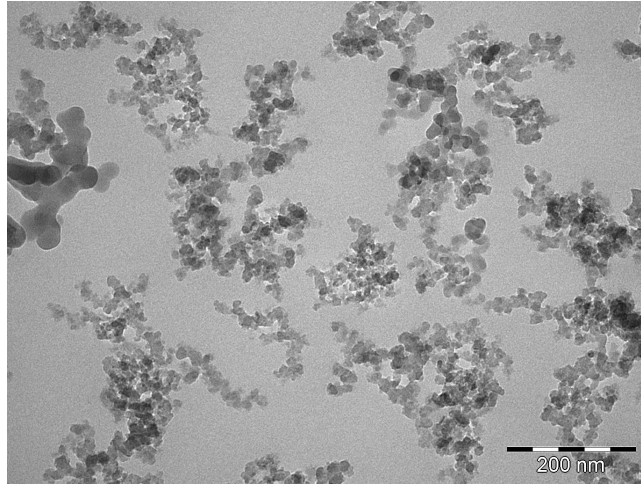


FIGURE 3.9: SEM picture of nanoparticles after filtration.

### 3.3.0.7 Material Parameters

We considered effective medium theory to calculate and predict the effective dopant concentration in the glass doped nanoparticles, which is the glass concentration multiplied by the fill fraction. Mie theory was then used to calculate the scattering cross-section of the inclusions and the absorption coefficients of the host and inclusions, and hence optical extinction of the glass nanoparticles in PMMA as a function of wavelength and fill factor.

### 3.3.1 Optical Loss and Gain

In the following section we analyse the optical gain at  $1.55 \mu m$  in an Er/Yb-doped glass nanocomposite with PMMA host pumped at  $980 \text{ nm}$  for a parameter space. The first aim is to calculate the optical gain as a function of Er/Yb concentration to identify the limiting values of the particle size and the volume fraction resulting in a necessary rare-earth concentration to obtain gain. The second is a trade-off between the scattering loss caused by nanoparticles and the optical gain by an appropriate choice of the inclusion parameters and the optimal length. Other than optical losses, the energy transfer between the gain materials plays an important role for optical gain. To identify this condition, the strong influence of the Yb/Er concentration on gain and optimal length can be understood in Fig. 3.10 and 3.11. Fig. 3.10 indicates that

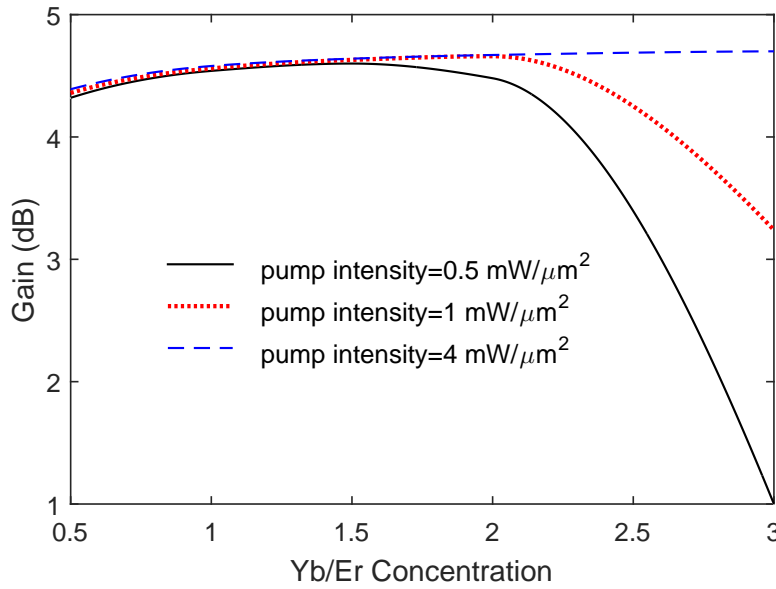


FIGURE 3.10: Dependence of the optical gain on  $\text{Yb}^{3+}/\text{Er}^{3+}$  concentration for a device length of  $L=1 \text{ cm}$  and different pump intensities.

gain is considerably sensitive to variation of the Yb/Er concentration at very low pump intensity for a length of  $5 \text{ cm}$ . The rapid reduction in optical gain at  $0.4 \text{ mW}/\mu m^2$  is due to inefficient energy transfer between  $\text{Yb}^{3+}$  to  $\text{Er}^{3+}$  because the pump light is scattered and absorbed by doped nanoparticles as it travels through the amplifier. However, the dependence of gain on length allows the amplifier to be designed for a maximum gain even at a low pump intensity for a wide range of the Yb/Er concentration as shown in Fig. 3.11. Fig. 3.12 shows the gain for different pump intensities; the gain reduces

rapidly with length for the pump intensity less than  $1 \text{ mW}/\mu\text{m}^2$ . For the highest gain the radius must be enough to include a proper Er/Yb concentration.

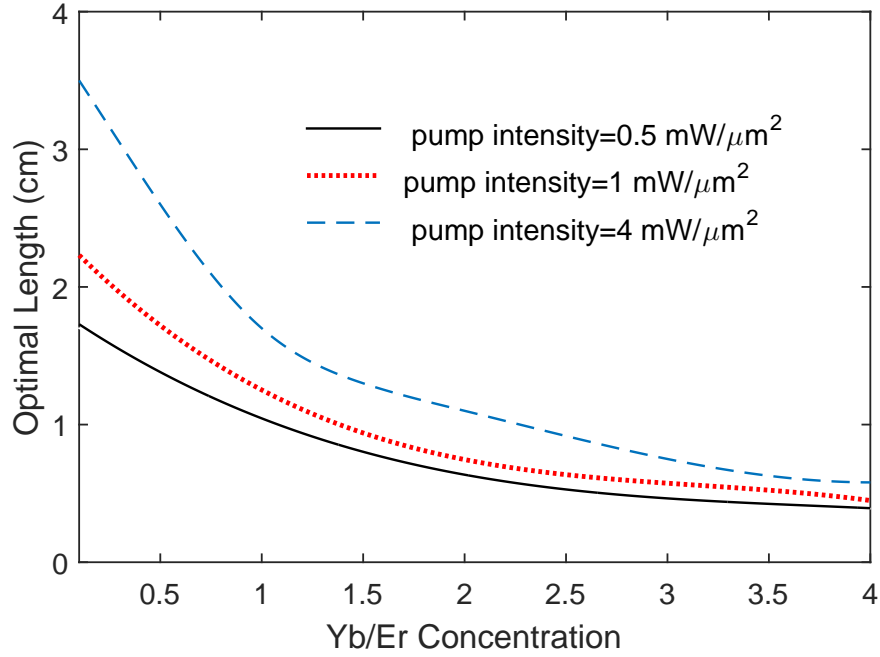


FIGURE 3.11: Optimal length obtained by maximising the gain  $\text{P}_2\text{O}_5:\text{Er}^{3+}/\text{Yb}^{3+}$  as a function of  $\text{Yb}^{3+}/\text{Er}^{3+}$  concentration.

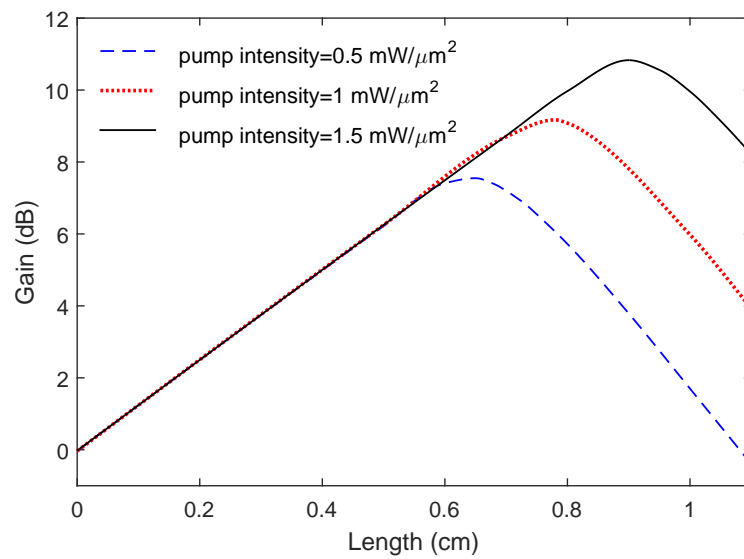


FIGURE 3.12: Optical gain for various pump intensities versus the length of amplifier including 10% nanoparticles with 100 nm radius.

Numerical calculation of gain for different radius shown in Fig. 3.13, confirms that the high gain can be obtained by operating at the pump intensity of  $1 \text{ mW}/\mu\text{m}^2$  and the radius less than 50 nm. However, for nanoparticles with radius larger than 50 nm, the rare-earth concentration is higher but the scattering loss dominates over short-range interactions. The optical gain was calculated as a function of fill fraction, amplifier length, and launched pump power for phosphate glass nanoparticles with 100 nm radius and doped bulk glass with Er and Yb concentration of  $10^{26} \text{ m}^{-3}$  and  $5 \times 10^{26} \text{ m}^{-3}$ , respectively. The latter parameters were chosen based on commercially available highly-doped bulk glass [172] and the typical particle size achievable by wet ball milling. Variations of the optical gain versus the nanocomposite polymer amplifier

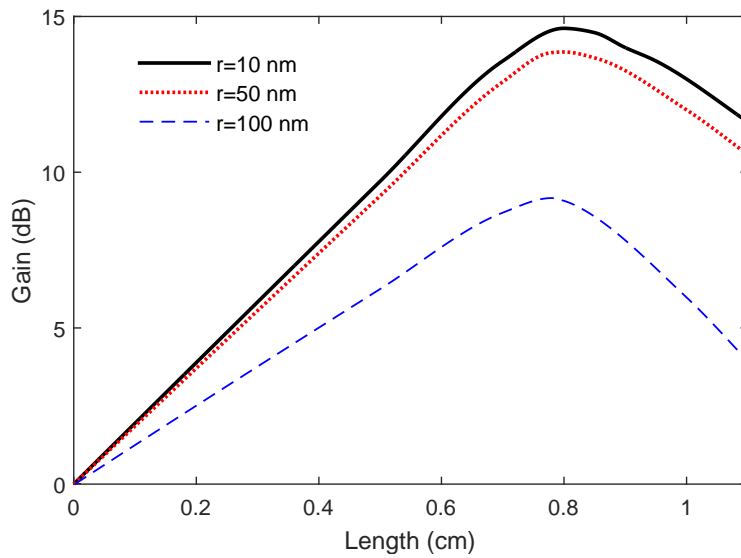


FIGURE 3.13: Optical gain as a function of length with pump intensity  $I_p=1 \text{ mW}/\mu\text{m}^2$  and signal intensity  $I_s=1 \text{ }\mu\text{W}/\mu\text{m}^2$  for nanoparticles with different radii,  $r$ , and volume fraction of 10 % .

length are shown in Fig. 3.14 for three values of the volume fraction,  $f=5\%$ ,  $10\%$ , and  $15\%$ . The range of Er/Yb concentration achievable with limited loss depends on the particle size and volume fraction. So, the optical gain increases faster as the volume fraction increases. The reduction in optimal length is due to increasing optical loss. Fig. 3.15 shows the dependence of the optical gain on the pump power for the same value of volume fraction and calculated optimum length; the saturated gain decreases as the volume fraction increases.

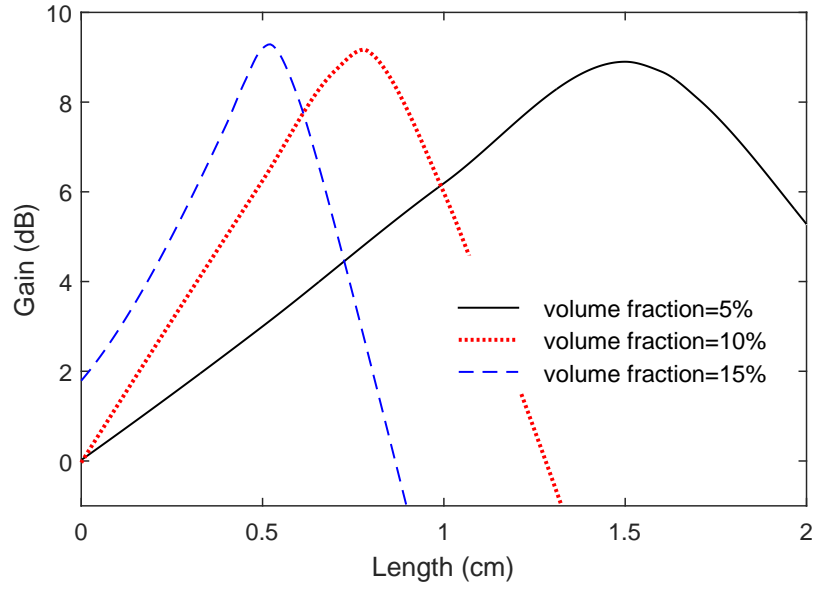


FIGURE 3.14: Signal gain versus length with launched pump intensity  $I_p=1 \text{ mW}/\mu\text{m}^2$ , launched signal intensity  $I_s=1 \text{ }\mu\text{W}/\mu\text{m}^2$  for different volume fractions of nanoparticles with 100 nm radius.

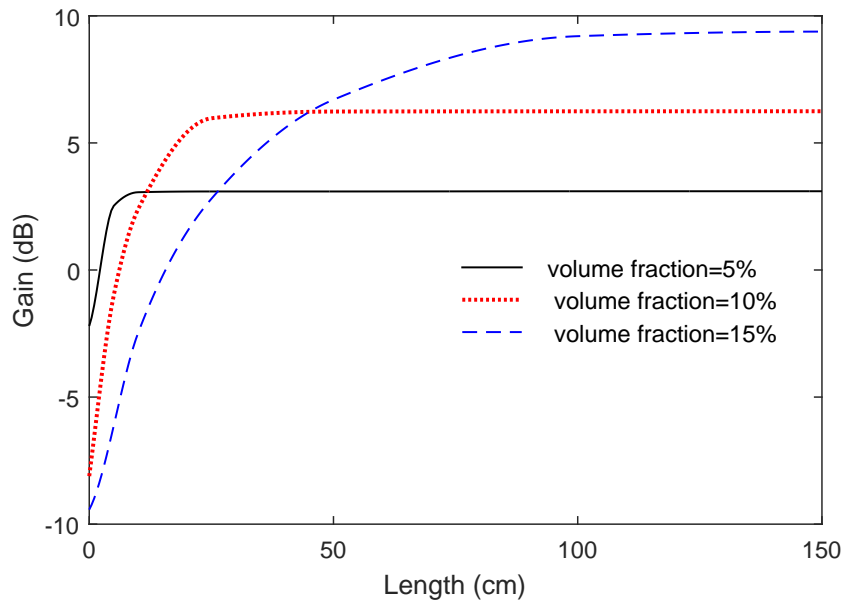


FIGURE 3.15: Dependence of the optical gain on pump power with launched signal intensity  $I_s=1 \text{ }\mu\text{W}/\mu\text{m}^2$  and length 5 mm for different volume fractions of nanoparticles with 100 nm radius.

### 3.4 Summary

We have proposed a novel way to overcome the insolubility of rare-earth ions into polymer based on a polymer nanocomposite material. We have then demonstrated the possibility of optical gain in polymer-based amplifiers incorporating doped phosphate glass as gain material. The gain of the proposed material depends strongly on the scattering loss caused by nanoparticles and often also absorption due to the host and/or particles. A detailed model for the optical gain of such materials incorporating the effects of scattering loss was described, and used to determine optimal material and device parameters within practically achievable ranges. It was predicted that useful optical gain is achievable in such materials.

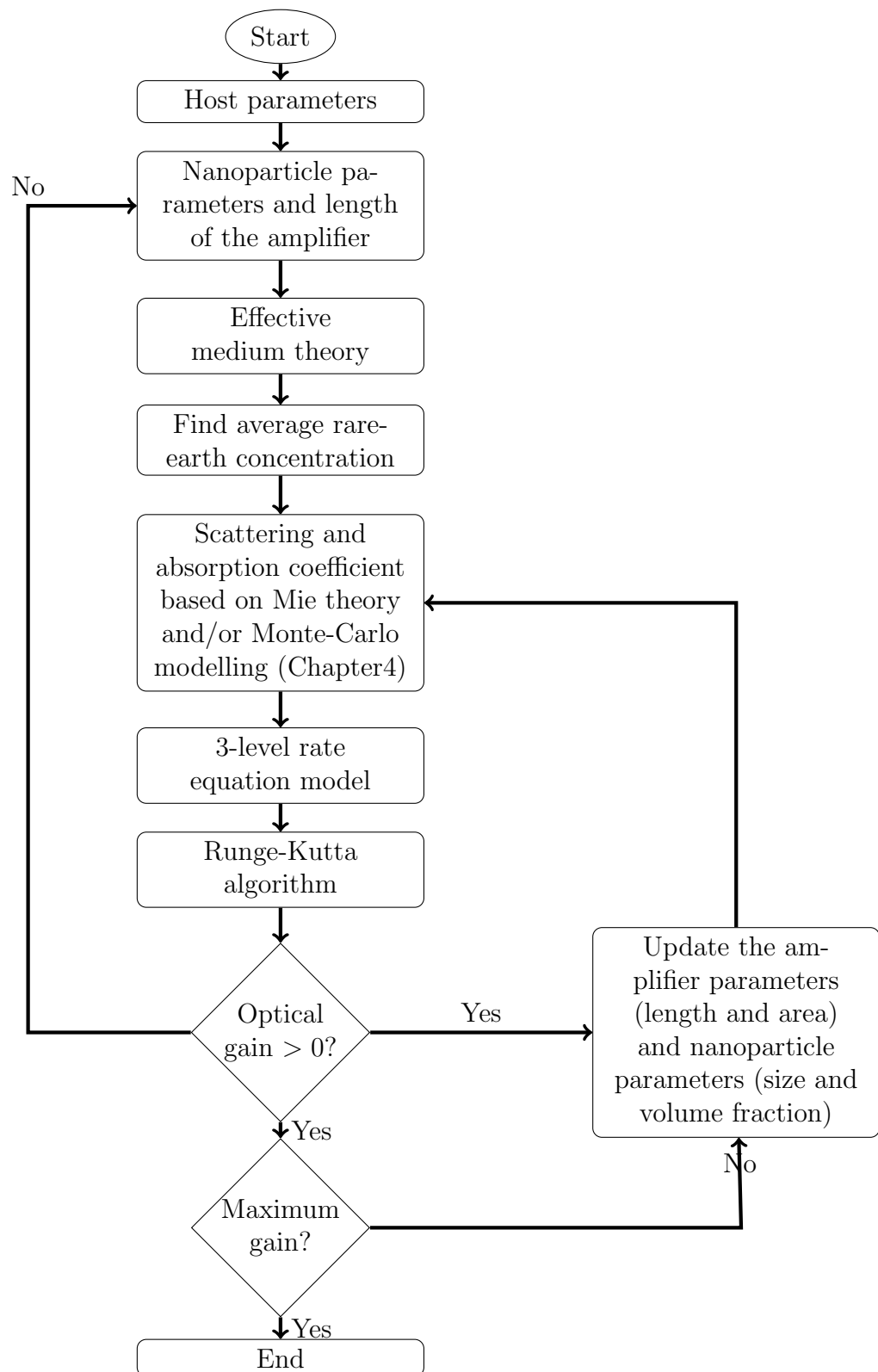


FIGURE 3.16: Flow chart of optimisation for maximising optical amplification in polymer nanocomposites.





# 4

## EM Waves in Strongly Scattering Composite Materials with Boundaries

A question addressed in this Chapter is to explore the extent to which the effects of multiple scattering can be controlled by the specific properties of the scattering medium, i.e. the size (relative to wavelength), relative refractive index and volume fraction of scatterers, and also the shape and effects of boundaries to convert a directional beam to an isotropic source.

### 4.1 Introduction

The study of light propagating through a highly scattering medium is of interest for a wide range of applications such as optical communications, material identification, spectroscopic measurements, biomedical diagnostics, etc. [118, 173–175]. In such media, characteristics such as depolarisation, attenuation are affected by multiple scattering [173, 174]. Although the multiple scattering distorts the propagating wavefront of an incident wave, it also modifies the spatial and spectral distribution of transmitted light [118, 119, 175, 176]. The design of components with tailored scattering properties is facilitated by numerical modelling tools which take into account properties such

as the size and the volume fraction of scatterers, relative refractive index, and etc. [113, 177, 178].

In the field of biology, Wilson *et al.* applied a Monte-Carlo algorithm to study photon transport in turbid tissues [179]. It has since been widely used to simulate the behaviour of light in tissue [178, 180]. Moreover, a variety of experimental techniques have been used to investigate scattering-induced effects in random media [173–175, 181–184]. In previous reports, the THz scattering impacts have mainly been studied in on-axis THz transmission and/or in the backscattering direction in semi-infinite samples. The latter measurements were taken to determine the properties associated with multiple scattering, including ballistic transport, statistics of the amplitude and phase distribution of the diffuse wave, and depolarisation of the light. These effects are of great interest to obtain information on the nature of the random medium, applicable in imaging and/or structural identification.

For example, Pearce *et al.* [181] studied on-axis transmission through thin slabs of mono-dispersed Teflon spheres to determine the scattering mean free path in a random medium. The same authors measured the diffusion of the THz pulses focused into a random medium at an angle of  $90^\circ$  to describe the statistics of multiple-scattered THz pulses [185]. Recently, THz scattering from rough surfaces has been examined in the context of indoor and short-range THz communications [186–189]. For example, Jansen *et al.* demonstrated communication channels at THz frequencies using diffuse scattering from randomly rough surfaces [186]. Priebe and Kurner represented the stochastic modelling of THz indoor channels based on specular reflection for future THz communication links [187]. In some other work, authors tried to address the problem of scattering, for example using a wavefront shaping technique to guide light through dense media [190].

THz scattering at angle off-axis THz transmission have not been studied. These measurements could be useful in THz sensing and telecommunications in which signals must be detected and/or measurements progress independent of the direction of the incoming THz radiation. Highly scattering materials can be used to purposely scatter light many times in order to generate a light-driven random walk; the light becomes diffuse. Therefore, multiple scattering could modify the spectral content and spatial distribution of the electromagnetic wave scattered out of such materials [119].

First, we have developed a numerical modelling tool using Monte-Carlo simulation of scattering events that also takes into account propagation loss and reflection and refraction at boundaries of finite samples. The aim is to determine ways in which to

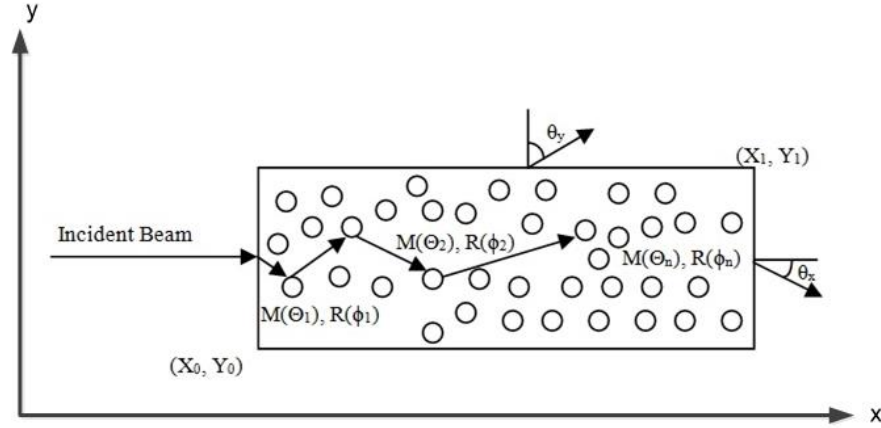


FIGURE 4.1: Geometry of a multiple scattering event in an air-polymer composite material (photons are launched at a single point of entry).

apply control over the spectral, and spatial distribution of light escaping from strongly scattering but weakly absorbing composite materials. We have applied the tool to the modelling and design optimisation of simple scattering objects, such as a slab of polymer containing a random array of air bubbles as shown schematically in Fig. 4.1 (photons are launched at a single point of entry). Using the tool we are able to determine the intensity of highly scattered photons escaping from the object as a function of wavelength and direction.

The measurements were taken using a time-domain spectrometer with a goniometer. Our method offer advantages over other experimental techniques, including the detection of the THz scattering at angle off-axis from the incident beam, giving both the spectral and spatial distribution of the THz radiation. With these results, we can evaluate how the effect of multiple scattering contributed to the redistribution of the THz pulses. Moreover, the measurements provide the possibility to discriminate the absorption and the scattering effects which is an important factor in some applications such as imaging and/or material identification.

## 4.2 EM Wave Propagation

Various aspects of electromagnetic wave propagation in highly scattering media have been studied by numerous modelling and theoretical studies. The choice of the appropriate model to assess light propagation in such media depends on the structure of the medium, including a medium with continuous or discrete scatterers as shown in Fig. 4.2, type of light (e.g. polarised), type of scattering, and absorption coefficient (weakly

or strongly absorptive). In this section a brief overview of the major approaches is presented.

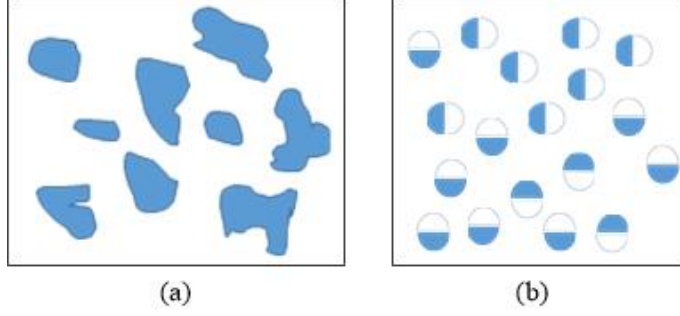


FIGURE 4.2: (a) random spatial and temporal fluctuations of refractive index, (b) randomly distributed scattering and absorption scatterers.

#### 4.2.1 Electromagnetic Theory

The propagation of electromagnetic wave through a medium can be described using Maxwell's equations. In the framework of electromagnetic theory, reflection, absorption and transmission can be described when the scattering is low (wavelengths are much greater than particle diameters). However, for an inhomogeneous structure where the size of the particles is comparable to the wavelength, the propagation of light in a multiply scattering medium in terms of Maxwell's equations becomes complex because the medium permittivity experiences random fluctuations. Therefore, this theory provides the characteristics of a medium with uniform absorption and scattering parameters, or a non-scattering medium with random and discrete scatterers. In an isotropic and nondispersive medium with a permittivity  $\varepsilon + \varepsilon_1(r)$ , the average electromagnetic energy can be written as:

$$\langle U(r) \rangle = \int Q(r, s) d\Omega \quad (4.1)$$

where  $Q$  is the angular component of the average energy in the direction  $s$ . The energy which is transferred across a surface element  $dA$  onto the solid angle  $d\Omega$  in a time  $dt$  is expressed by:

$$dW = I(r, s) (s \cdot n) dA d\Omega dt \quad (4.2)$$

where  $n$  is the unit normal to  $dA$  and  $I$  is the radiance, expressed by:

$$I(r, s) = vQ(r, s) \quad (4.3)$$

where  $v$  is the propagation speed in the medium.

### 4.2.2 Radiative Transfer Theory

In radiative transfer theory, light propagation is considered as a flow of discrete photons. Although power and intensity are considered, the phase and amplitude are ignored. The propagation of photons in a turbid medium is formalised by the radiative photon transport equation (RTE). The RTE relates the gradient of the radiance to losses resulting from absorption and scattering:

$$\begin{aligned} \frac{1}{v} \frac{\partial}{\partial t} I(r, \Omega, t) + \Omega \cdot \nabla_r I - \sigma_s \int_{4\pi} p(\Omega', \Omega) I(r, \Omega', t) d\Omega' + \\ \sigma_t I(r, \Omega, t) = F(r, \Omega, t) \end{aligned} \quad (4.4)$$

where  $I$  is the radiance,  $\sigma_t$  the total loss,  $\mu_s$  the scattering coefficient,  $p$  the phase function, and  $F$  the source of power generated at  $r$  in direction  $s$ . One way to find a solution for the RTE is to represent it as a pair of coupled differential equations by approximating the radiance with a function series. This method is known as the Diffusion approximation.

$$\begin{cases} \frac{1}{v} \frac{\partial \phi(r, t)}{\partial t} + \nabla J(r, t) + \mu_a \phi(r, t) = S(r, t) \\ \frac{1}{v} \frac{\partial J(r, t)}{\partial t} + \frac{1}{3} \nabla \phi(r, t) + \mu_t J(r, t) = 0 \end{cases} \quad (4.5)$$

where  $\phi$  and  $J$  are the fluency rate and flux rate at  $(r, t)$ , respectively.  $S(r, t)$  represents the photon source given by:

$$\begin{aligned} \phi(r, t) &= \oint_{4\pi} I(r, s', t) d\Omega' \\ J(r, t) &= \oint_{4\pi} S' I(r, s', t) d\Omega' \\ S(r, t) &= \oint_{4\pi} Q(r, s', t) d\Omega' \end{aligned} \quad (4.6)$$

The radiance in the diffusion approximation is defined as follows:

$$I(r, s, t) = \frac{1}{4\pi} \phi(r, t) + \frac{3}{4\pi} J(r, t) s \quad (4.7)$$

A number of solutions for the RTE can be found in the literature such as Adding-Doubling, and Flux theory [191, 192]. However the main problem is that the latter

methods assume that the internal radiation is nearly isotropic, hence they are inaccurate when scattering is comparable with absorption. Statistical methods, such as the Random Walk and Monte Carlo methods, are alternatives to model the propagation of light in a randomly scattering medium. In the latter methods, the interaction between individual photon and random scatterers is simulated. In the case of the Random Walk theory, the statistical behaviour of photons in a medium is described within a cubic lattice consisting of adjacent points. The photon step size is inversely proportional to the scattering coefficient and the propagation of photons is isotropic (good agreement with the Diffusion approximation). However the Random Walk approach is restricted to the multi-layered structures and the number of possible photon directions. By contrast, the Monte-Carlo method calculates intensity with index mismatching and anisotropy of scattering. Moreover, it is a flexible method which allows for: (i) following the optical path of photon transport in a medium, (ii) intensity beam distribution, (iii) 3D representation of the medium, (iv) a multi-layered scattering medium with inhomogeneities, and (v) calculating the actual parameters of the medium such as absorption, scattering, and refractive index.

### 4.3 Modified Monte-Carlo Modelling

The model reported here is generally applicable, however, for the purpose of demonstration we consider its application to THz scattering. The sample is described by the following parameters: the thickness, the length, and the refractive index ratio of inclusions to host ( $m$ ).

- Launching Photons

A coordinate system is defined to represent the position of a photon packet,  $r(x,y,z)$ , and the direction of the photon propagation as shown in Fig. 4.3. The components of the vector  $a$  is expressed by:

$$a = \sin\theta\cos\varphi\hat{a}_x + \sin\theta\sin\varphi\hat{a}_y + \cos\theta\hat{a}_z \quad (4.8)$$

The initial polar angle  $\theta$  and azimuthal angle  $\varphi$  define the current direction of the incident photons. Each photon is also initially assigned a weight ( $w$ ). The interaction point between a photon and scatterers is defined by probability density function (PDF). If  $x$ , for instance, is a random variable characterising the

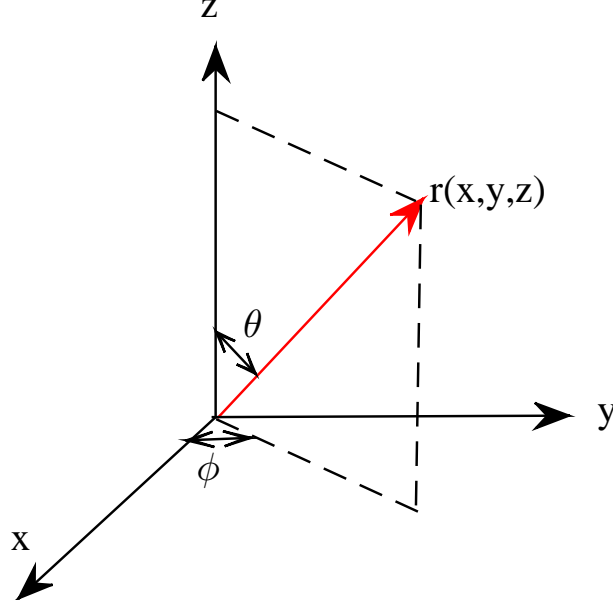


FIGURE 4.3: Photon packet's position in the scattering medium with the direction of propagation defined by the polar and azimuthal angles.

interaction, the PDF  $p(x)$  is given by:

$$F(x) = P(x \leq a) = \int_{-\infty}^a p(x) dx \quad (4.9)$$

where  $F(x)$  is the cumulative probability function (CPF). A random sample can be obtained from  $P(x \leq a)$  using a random number,  $\varsigma$ , distributed between 0 and 1.

- Scatterer Specifications

The absorption coefficient  $\mu_a$  ( $\text{cm}^{-1}$ ) and the scattering coefficient  $\mu_s$  ( $\text{cm}^{-1}$ ) of the sample are calculated using Mie theory and/or Rayleigh scattering, depending on the size of the scatterers and the wavelength. The scattering anisotropy ( $g$ ) factor indicates forward directed scattering ( $0 < g < 1$ ), backscattering ( $g=0$ ) and isotropic scattering ( $-1 < g < 0$ ), given by:

$$g = \frac{\int_0^\pi S_{11}(\theta) \cos(\theta) 2\pi \sin(\theta) d\theta}{S_{11}(\theta) 2\pi \sin(\theta) d\theta} \quad (4.10)$$

where  $S_{11}(\theta)$  is the scattered intensity from the inclusions. The scattering anisotropy

factor ( $g$ ) can be calculated using Mie theory as follow:

$$g = \langle \cos\theta \rangle = \frac{4\pi a^2}{x^2 \sigma_s} \left[ \sum_n \frac{n(n+2)}{n+1} \text{Re} \{a_n a_{n+1}^* + b_n b_{n+1}^*\} + \sum_n \frac{2n+1}{n+1} \text{Re} \{a_n b_n^*\} \right] \quad (4.11)$$

- Moving Photon

A photon is launched at an initial position. Before being scattered, the photon moves to the new position with a path length. The photon path length distribution can be expressed by:

$$p(s) = \mu_t e^{-\mu_t s} \quad (4.12)$$

where  $\mu_t$  is the total loss that is sum of scattering and absorption. By substituting equation 4.12 into 4.9, the free path length is calculated by:

$$s = -\frac{\ln(\varsigma)}{\mu_t} \quad (4.13)$$

Once the photon has taken a step in the sample, it drops part of its energy by:

$$\Delta w = w \times \frac{\mu_a}{\mu_t} \quad (4.14)$$

- Photon Scattering

The probability distribution of the scattering angle described by the Henyey-Greenstein function, equation 4.15, was used to determine each photon's direction following each scattering event.

$$p(\cos\theta) = \frac{1}{4\pi} \frac{1 - g^2}{(1 + g^2 - 2g\cos\theta)^{3/2}} \quad (4.15)$$

The polar and azimuthal angles can be obtained by taking the inverse Fourier Transform from equation 4.9 as follows:

$$\cos(\theta) = \begin{cases} \frac{1}{2g} \left\{ 1 + g^2 - \left[ \frac{1-g^2}{(1-g+2g\zeta)} \right]^2 \right\} & \text{if } g \neq 0 \\ 2\zeta - 1 & \text{if } g = 0 \end{cases} \quad (4.16)$$

$$\varphi = 2\pi\xi \quad (4.17)$$



- New Position

The new position of photon after it has been scattered depends on whether the photon has reached the boundary along the x, y, and z axes. So, the updated position is:

$$\begin{bmatrix} x' \\ y' \\ z' \end{bmatrix} = \begin{bmatrix} x \\ y \\ z \end{bmatrix} \pm s \begin{bmatrix} \sin(\theta')\cos(\varphi') \\ \sin(\theta')\sin(\varphi') \\ \cos(\theta') \end{bmatrix} \quad (4.18)$$

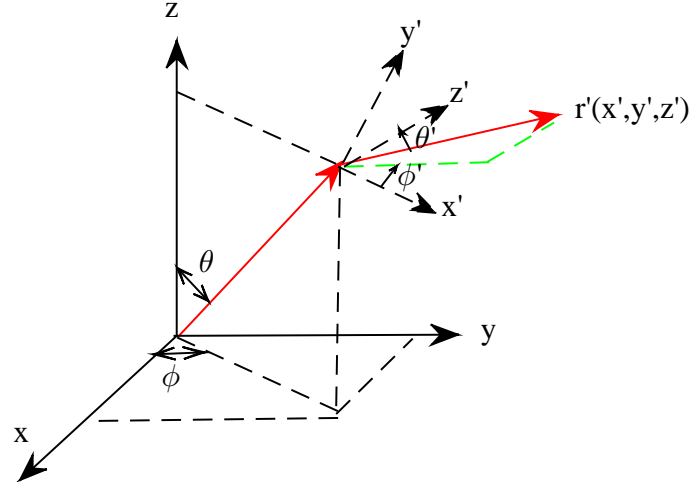


FIGURE 4.4: A new direction of photon after being scattered.

### 4.3.1 Reflection

Tests are performed to ascertain whether a ray has reached the boundaries ( $X_0, X_1, Y_0, Y_1$ ). If it has, the incident angle will be calculated using the position of the photon ( $X, Y$ ) and be compared with the critical angle determined by Snell's law. If it is internally reflected, the reflection will be determined by the Fresnel function (equation 4.19), otherwise it is recorded as a transmitted photon.

$$R(\alpha_i) = \frac{1}{2} \left[ \frac{\sin^2(\alpha_i - \alpha_t)}{\sin^2(\alpha_i + \alpha_t)} + \frac{\tan^2(\alpha_i - \alpha_t)}{\tan^2(\alpha_i + \alpha_t)} \right] \quad (4.19)$$

$$R = \frac{(n_2 - n_1)^2}{(n_2 + n_1)^2} \quad \text{if} \quad \alpha_i = 0 \quad (4.20)$$

where  $\alpha_i$  is the angle of incidence, and  $\alpha_t$  the angle of transmission given by:

$$n_i \sin \alpha_i = n_t \sin \alpha_t \quad (4.21)$$

where  $n_i$  and  $n_t$  are the refractive indices of the medium that the photon is incident from and transmitted to, respectively. To determine whether the photon escapes the sample or is internally reflected, the internal reflectance is compared with the random number, i.e. if  $\zeta \leq R(\alpha_i)$ , then the photon is internally reflected, otherwise it escapes the medium. All photons are tracked until absorbed (i.e. the photon weight falls below a minimum threshold) or they cross one of the boundaries. Escaped photons contribute to the transmittance. Upon reaching a boundary, the diffuse transmittance ( $T_d$ ) is incremented by the weight of the escaping photon:

$$T_d = T_d + w \quad (4.22)$$

## 4.4 Discussion

After a certain value of the dimension, the boundaries affect the shape of the light distribution as the incident light can be scattered at different directions due to the multiple scattering. Table 4.1 summarises the results for increasing slab thickness  $Y_1$ - $Y_0$  (the length,  $X_1$ - $X_0$ , remained 10 mm). As the medium became thicker than 3 mm the diffuse transmittance from the top boundary ( $Y_1$ ) decreased. The results also show that the angle of strong scattering from the direction of the incident beam is generally higher than in thick samples. Fig. 4.5 and Fig. 4.6 show strong scattering of the incident photons in a 1 mm-thick sample from the  $Y_1$  and  $X_1$  boundaries over approximately 60 and 15 degrees, respectively.

## 4.5 Experiments

In order to understand how scattering and boundaries can affect the spatial distribution of the light, we measure a fibre coupled THz-TDS set up with a goniometer to investigate the angular and frequency dependence of the THz scattering. The receiving antenna was placed on a goniometer arm, allowing angle-dependent measurements. To

TABLE 4.1: Values for diffuse transmittance from the top (Y) and end (X) boundaries of an air-polymer composite slab.

Sample Dimensions (Y×X mm <sup>2</sup> )	Photons Transmitted From Y <sub>1</sub>	Angle of Main Lobe Transmitted at Y <sub>1</sub> (i.e. $\theta_y$ Shown in Fig. 4.1)	Photons Transmitted From X <sub>1</sub>	Angle of Main Lobe Transmitted at X <sub>1</sub> (i.e. $\theta_x$ Shown in Fig. 4.1)
1×10	30.3%	$0 < \theta < 60^\circ$	2.38%	$0 < \theta < 15^\circ$
2×10	33.3%	$5 < \theta < 45^\circ$	5.58%	$0 < \theta < 30^\circ$
3×10	40.5%	$5 < \theta < 30^\circ$	22.24%	$0 < \theta < 45^\circ$
4×10	21%	$25 < \theta < 60^\circ$	18.67%	$0 < \theta < 65^\circ$
5×10	12.2%	$35 < \theta < 70^\circ$	25.91%	$0 < \theta < 70^\circ$

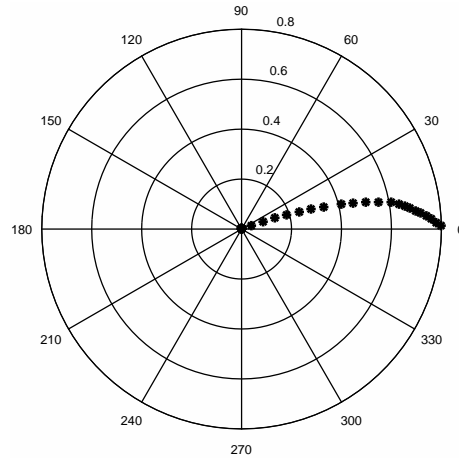


FIGURE 4.5: Simulated light transmission from the surface of X<sub>1</sub> after propagation of a 120 GHz beam through a Y×X= 1×10 mm<sup>2</sup> slab of air-polymer composite. Escaped photons contributed to the transmittance pattern, i.e. intensity per solid angle.

suppress the measurement of cross-polarised radiation, two wire-grid polarisers were placed in front of both the receiver and transmitter antenna. Fig. 4.7 shows the measurement principle. The diffuse scattering was measured at different angles between -90 to 120 degrees.

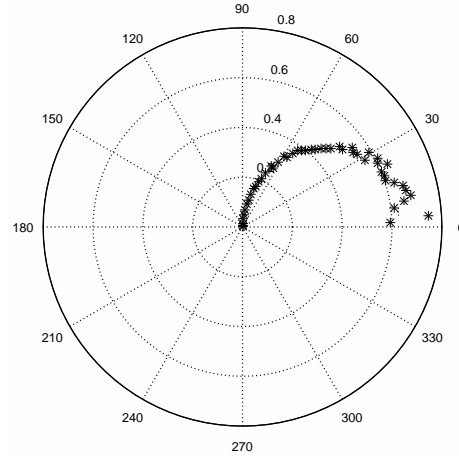


FIGURE 4.6: Simulated light transmission from the surface of  $Y_1$  after propagation of a 120 GHz beam through a  $Y \times X = 1 \times 10 \text{ mm}^2$  slab of air-polymer composite. Escaped photons contributed to the transmittance pattern, i.e. intensity per solid angle.

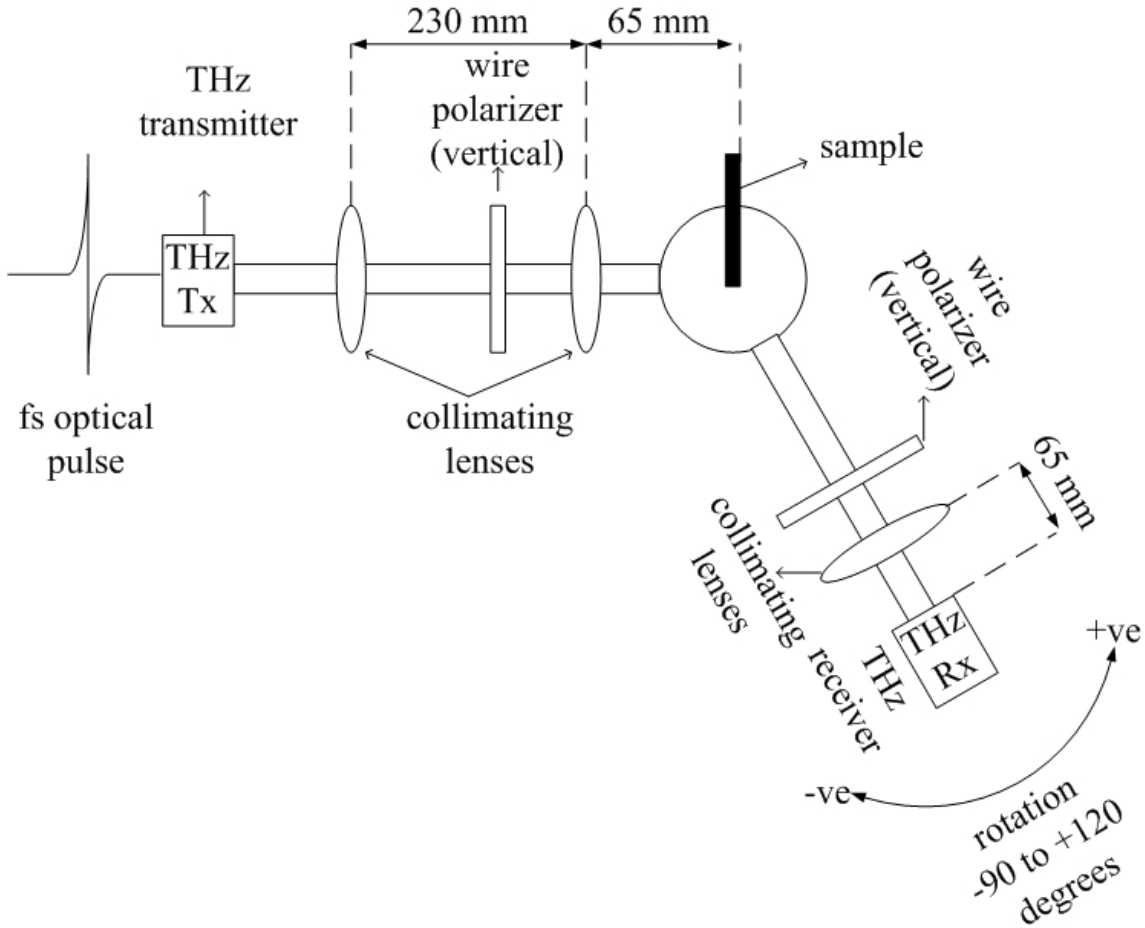


FIGURE 4.7: Experimental arrangement for measurements of angle- and frequency-dependent THz scattering in a strongly scattering medium.

### 4.5.1 Data Analysis in THz Spectroscopy

A THz-TDS spectrometer permits to determine the temporal waveforms of the THz pulses by measuring the field strengths of the short electromagnetic pulse in time domain. The temporal shape of the THz pulse changes during propagation through a sample material. This change depends on the linear response of materials associated with the optical properties of the materials; complete information of the dielectric function can be determined. The detailed frequency dependence of optical properties can be obtained by Fast Fourier Transformation (FFT), and a comparison of this pulse with a reference pulse. Consider a plane wave with angular frequency  $\omega$  propagating through a medium in  $z$  direction:

$$E(z, t) = E_0 \exp\left(i \frac{n\omega}{c} z\right) \exp\left(-\frac{k\omega}{c} z\right) \quad (4.23)$$

To get the frequency information, we take Fourier transform of equation 4.23:

$$\begin{aligned} E(\omega) &= \frac{1}{2\pi} \int_{-\infty}^{\infty} e^{-i\omega t} E(t) dt \\ &= E_0(\omega) \exp\left(i \frac{n(\omega)\omega}{c} z\right) \exp\left(-\frac{k(\omega)\omega}{c} z\right) \end{aligned} \quad (4.24)$$

where  $n$  and  $k$  are real and imaginary part of the refractive index. When the THz pulse passes through a sample, there are some reflection losses at the medium boundaries. The Fresnel equations can be used to calculate the reflection and transmission amplitude of normal incident without scattering at each interface as follows:

$$T = T_{air \rightarrow sample} \cdot T_{sample \rightarrow air} = 4 \frac{n(\omega)}{(n(\omega) + 1)^2} \quad (4.25)$$

For the reference pulse, the pulse only propagates through an empty spectrometer:

$$E_{ref}(\omega) = E_0(\omega) \exp\left(i \frac{\omega z}{c}\right) \quad (4.26)$$

The transfer function (i.e. the relative amplitude and phase of the sample and the reference wavefronts) of the system determines the complex transmission coefficient of

the system, given by:

$$H(\omega) = \frac{E_{sam}}{E_{ref}} = \frac{4n(\omega)}{(n(\omega) + 1)^2} \exp\left(i \frac{n(\omega) - 1}{c} \omega z\right) \exp\left(-\frac{k(\omega)}{c} \omega z\right) \quad (4.27)$$

The transfer function is a complex number which can be written as:

$$H(\omega) = |H| e^{i\phi(\omega)} \quad (4.28)$$

Therefore the THz-TDS provides both the phase and the amplitude. Consequently, the index of refraction can be extracted from the phase as:

$$n(\omega) = 1 + \frac{\phi c}{\omega d} \quad (4.29)$$

where  $d$  is the sample thickness. The complex index and the absorption coefficient can be evaluated from the frequency dependent amplitude and phase:

$$\begin{aligned} k(\omega) &= -\frac{c}{\omega d} \ln\left(\frac{(n(\omega)+1)^2}{4n(\omega)} |H|\right) \\ \alpha(\omega) &= 2 \frac{k(\omega)\omega}{c} \end{aligned} \quad (4.30)$$

### 4.5.2 Dynamic Range

Jepsen *et al.* have described a quantitative method to identify the fundamental limits of the measurable absorption coefficient in transmission and reflection of THz-TDS [193]. Due to the typical single-cycle nature of the THz pulse, the amplitude is strongly frequency dependent; at high frequencies the spectrum exhibits intensity dependent roll-off, before reaching to the noise floor. It should be noted that fluctuations in the THz pulse are caused by laser intensity fluctuations, whilst the noise floor is normally independent of frequency and corresponds to an electronic nature. Fig. 4.8 shows the dynamic range (DR) that is the signal above the noise floor where the noise floor level is set to 1, giving an upper limit to the detectable absorption coefficient of samples. Jepsen showed the largest absorption coefficient that measured with a given dynamic range and sample thickness  $d$ :

$$\alpha_{max}(\omega) = \frac{2}{d} \ln\left(DR \frac{4n}{(n+1)^2}\right) \quad (4.31)$$

The absorption features above the value of  $\alpha_{max}$  can not be detected and are saturated by the value of  $\alpha_{max}$ .

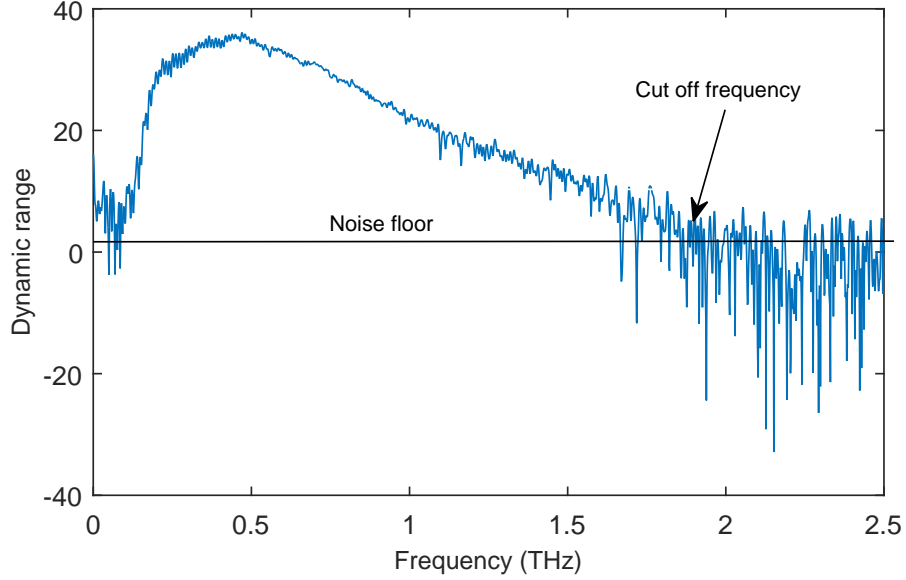


FIGURE 4.8: Dynamic range is defined relative to the noise floor.

### 4.5.3 Etalon Reflection

When a THz beam with the wavelength comparable to the size of the sample penetrates the interface between two media, multiple reflections can happen; a part of beam refracted into the medium reaches the interface, and hence it again undergoes reflection and refraction as shown in Figs 4.9 and 4.10. Therefore, the multiple reflection within the sample splits the wave into a number of intermediate paths. The phase retardation associated with each intermediate component can be given by:

$$\Delta\phi = \frac{2d_1n\omega}{c} \quad (4.32)$$

In the case of  $\Delta\phi = \pi$ , the signal attenuates due to a negative interference. The signal loss can be determined by the maximum absorption observed at phase velocity (equation 4.33) and its odd multiples.

$$v = \frac{c}{4\pi d_1 n} \quad (4.33)$$

The multiple reflection effects leads to a periodic structures in the frequency domain.

The Etalon echoes in the data can corrupt the extracted optical constants, in particular, in thick samples with high absorption. To avoid the etalon features, the data in time domain can be simply cut off without losing significant information to remove unwanted responses in the frequency domain.

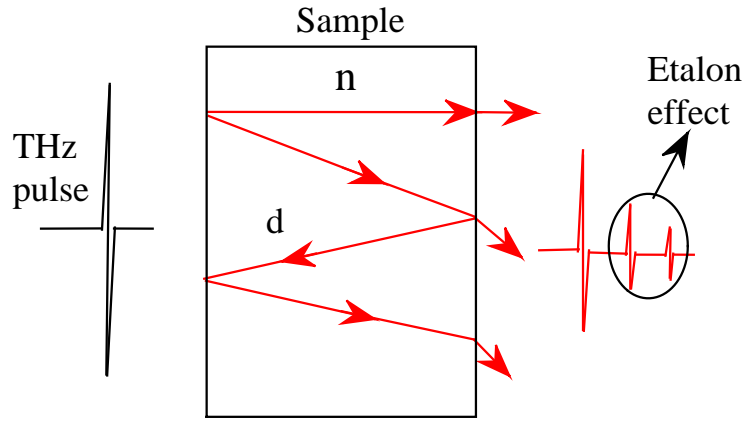


FIGURE 4.9: The Etalon effect caused by multiple reflections.

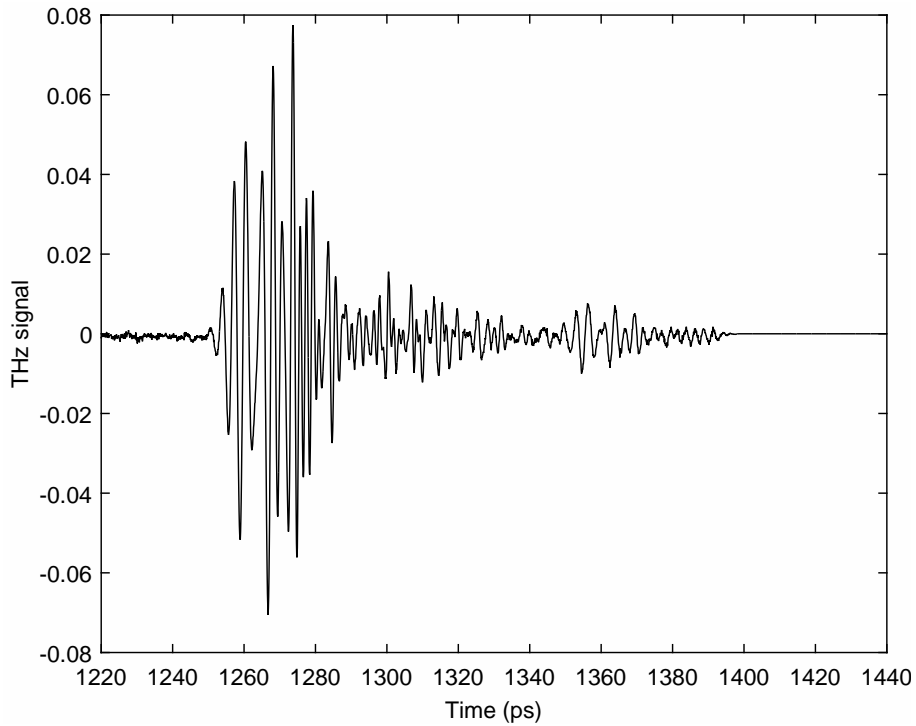


FIGURE 4.10: THz pulses transmitted through an air-polycarbonate composite material with 20 mm thickness.



## 4.6 THz Interaction with Composite Materials

We study the frequency-dependent THz scattering and transmission loss due to the combined effects of scattering and absorption in foamed or porous air-polycarbonate composite materials and 2-D polymer microstructures which are strongly scattering, but only moderately absorptive, at THz wavelengths.

### 4.6.1 Measurements

#### Air-Polycarbonate Composite Materials:

##### 4.6.1.1 Sample Preparation

As indicated in Fig. 4.11, we fabricated a highly scattering composite material of air bubbles in polycarbonate to evaluate its performance at THz frequencies, and to predict its behaviour in the presence of THz absorption and scattering losses. Polycarbonate is a proper material for our study as its absorption coefficient is quite low at terahertz frequencies. The bubbles were formed by thermal processing of the polymer (i.e. randomly distributed) and estimated to have a diameter of 200  $\mu\text{m}$  with a fill-factor of 50%. The size of inclusion can be controlled by the temperature, time, and vacuum. For our purpose, the size of scatterers needs to be comparable to the wavelength of THz radiation to incur enough scattering events and exhibit Mie effects in the frequency spectra. It is well known that many polymers absorb moisture, e.g. from the atmosphere. If the moisture is not removed from the polymer prior to thermal processing then bubbles may form in the material as the polymer softens and the water boils. So, heating commercially supplied polycarbonate (PC) resulted in a dense array of small bubbles distributed randomly in both size and position throughout the polymer. We baked the solid polymer for approximately 1 hour at 180  $^{\circ}\text{C}$  to form air bubbles inside the polymer.

A fiber-coupled THz-TDS setup was used to measure the transmission of a collimated broadband THz beam through “foamed” polycarbonate (PC) pucks (i.e. 14 mm diameter by 1 or 5 mm thick). The resulting material was estimated to have scattering and absorption loss coefficients of 0.5  $\text{mm}^{-1}$  and 0.1  $\text{mm}^{-1}$ , respectively, at 300 GHz. Fig. 4.12 shows the total loss coefficient in transmission as a function of frequency for the two pucks. There was good agreement between the experiment and numerical calculations of the loss coefficient, independent of sample thickness, especially at low



FIGURE 4.11: Foamed polycarbonate materials.

THz frequencies where scattering was relatively weak. Differences between the measurements and simulations above 800 GHz were likely because the scatterers (i.e. the bubbles) in the polycarbonate were not monodisperse in size.

The path length for the ballistic photons equals the sample thickness and consequently for thin samples (i.e. with thickness similar to or less than the inverse of the scattering coefficient, as in the 1 mm thick puck) loss will primarily be due to absorption. Conversely, as the sample thickness increases, scattering is expected to dominate in the transmission loss, with radiation being redirected into off-axis directions relative to the incident beam. Whilst it is difficult to differentiate the ballistic and scattered components in the time-domain signals shown in Fig. 4.13, they are clearly evident in the frequency domain spectra shown in Fig. 4.14. At low frequencies ( $\sim 200$  GHz) the loss is dominated by absorption, consistent with simulation results shown in Fig. 4.12, and increases as one would expect with sample thickness. At high frequencies ( $> 500$  GHz), the attenuation due to scattering dominates, with most of the short wavelength components of the incident pulse being scattered away from the direction of incidence. Consequently the apparent bandwidth of the THz signal is reduced to 1.1 THz and 700 GHz as the sample thickness increases from 1 mm to 5 mm, respectively. The scattering out of high frequency components is also partially evident in the time-domain signal, as the signal transmitted through 5 mm sample appears broader in time (i.e. low-pass filtered) with respect to the signal transmitted through the 1 mm sample and

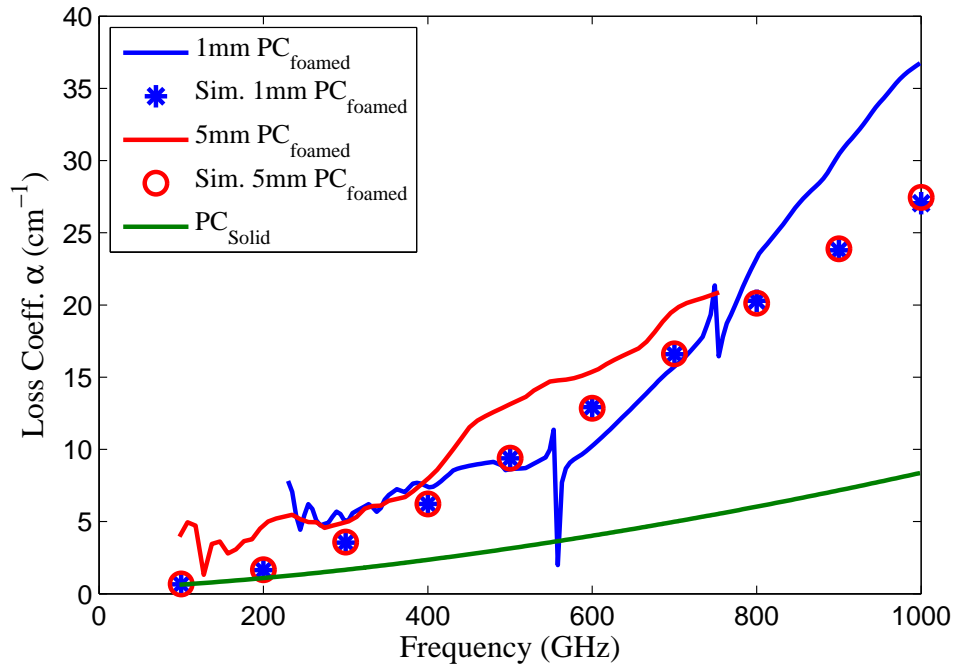


FIGURE 4.12: Experimental and simulated total attenuation coefficient (absorption plus scattering) for air-polycarbonate composite material with thickness 1 mm and 5 mm.

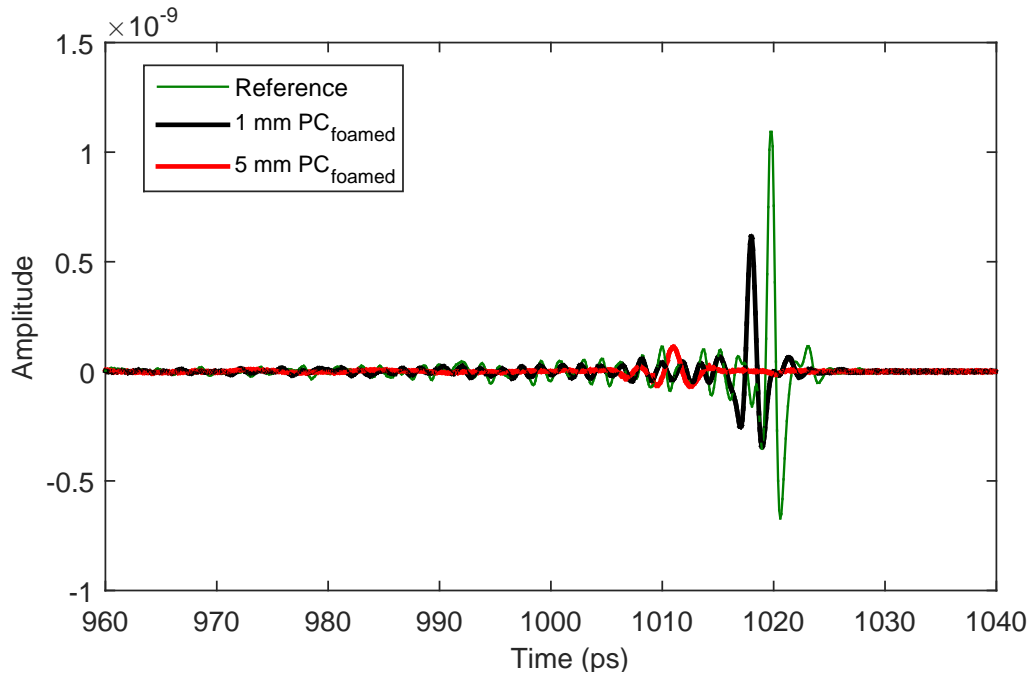


FIGURE 4.13: Time-domain THz waveform measured with THz-TDS for samples with 14 mm diameter by 1 and 5 mm thickness.

the reference signal.

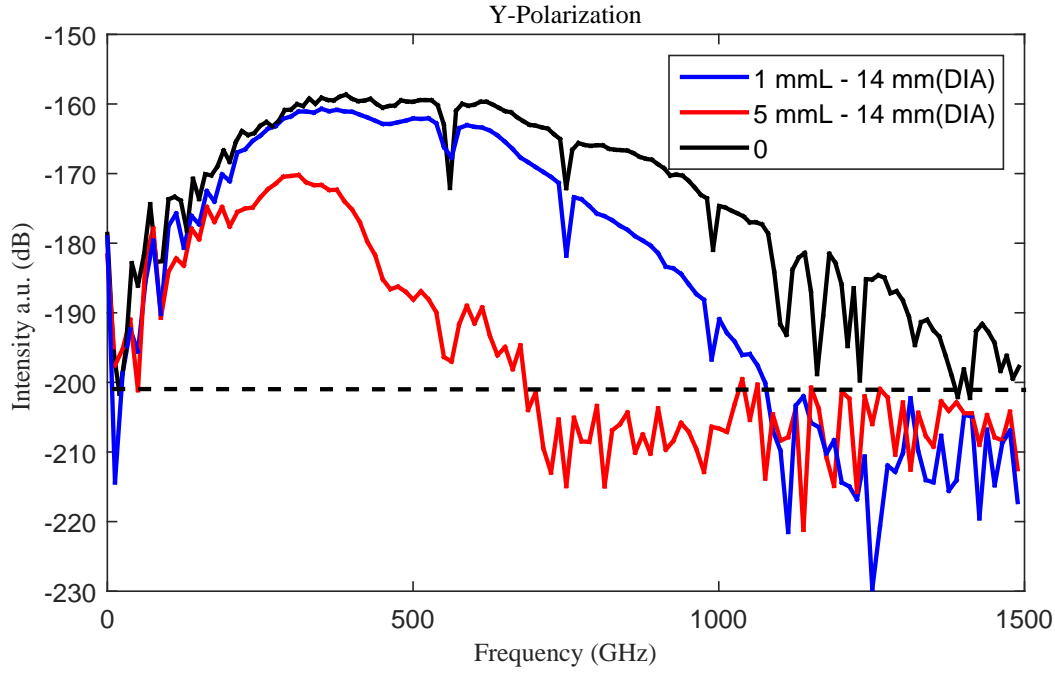


FIGURE 4.14: The spectrum of the THz pulse transmitted by taking the Fourier transform of the time-domain THz waveform for the samples.

The spatial distribution of the scattered THz radiation is expected to vary with both the scattering coefficient and sample thickness. Fig. 4.15 illustrate the expected impact of puck thickness on the spatial distribution of transmitted radiation at 300 GHz, i.e. where the loss coefficients due to scattering and absorption were similar in magnitude. The increased number of scattering events in the thicker puck resulted in a significantly broader spatial distribution of the scattered radiation.

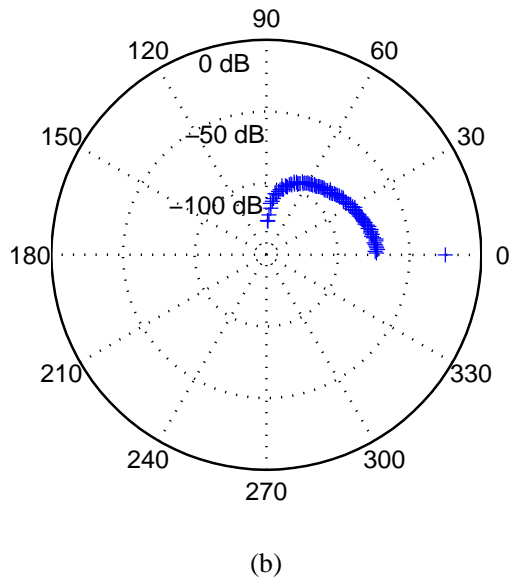
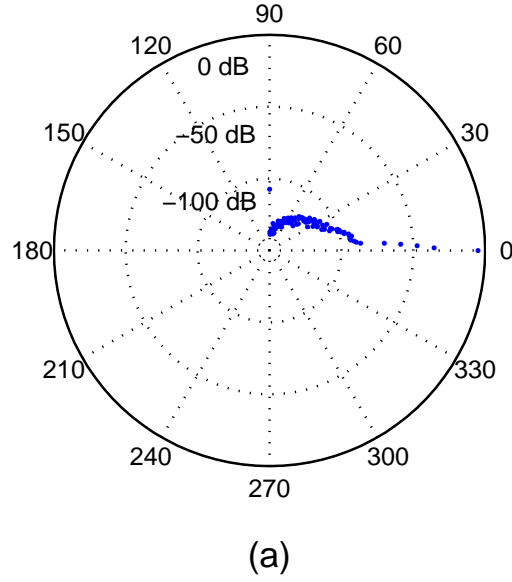


FIGURE 4.15: Simulated radiation pattern at 300 GHz following transmission through (a) 1 mm, and (b) 5 mm thick pucks of air-polymer composite materials, 14 mm in diameter. The radial scale is in decibels.

## 2-D Scatterers:

We represent results of measurements of THz pulses propagating through two-dimensional (2-D) polymer microstructures. We fabricated two different types of polycarbonate microstructures: i) a microstructure made by a suitable stacking pattern of

microtubes, ii) solid rods inserted to randomly distribute the microtubes in size and position. The measurements were taken using a time-domain THz spectrometer with a goniometer, giving both the spectral and the spatial distribution of the THz radiation transmitted through the samples.

#### 4.6.1.2 2-D Diffusers Fabrication Process

An efficient multiply scattering medium requires two conditions: i) structures with subwavelength features at the frequency range of interest from 300 GHz to 1 THz, which corresponds to wavelengths between 1 mm-300  $\mu\text{m}$ , and ii) a weakly absorbing randomly-inhomogeneous structure. Therefore, a fabrication technique is required to provide randomly distributed 2-D scatterers with a size comparable to the wavelength of the THz radiation, which can result in a strong 2-D scattering medium.

The 2-D THz polymer microstructure is fabricated using polycarbonate rods with an outer diameter of 6.5 mm. The fabrication of the randomly distributed polymer microstructures was carried out by capillary stacking in the ANFF fiber-draw tower facilities at the University of Sydney, Australia. First, a polycarbonate tube with an outer diameter of 6.5 mm was pulled down to 300  $\mu\text{m}$  outer diameter and cut into two hundred pieces with a length of 20 cm. An outer jacket was introduced to reduce the inner diameter of the preform and to limit the volume fraction of microtubes to around 30%. Afterwards, the stacked preform was drawn to about 6.5 mm outer diameter, resulting in microtubes with a diameter of 450  $\mu\text{m}$ , shown in Fig. 4.16. During the pulling process low-pressure was applied to prevent the inner microtubes from collapsing. The second sample with 10% polycarbonate solid rods with 400  $\mu\text{m}$  diameter was fabricated to randomise the 2-D scatterers in size and position, resulting in an inhomogeneous microstructure as shown in Fig. 4.17.

In order to model total loss (absorption plus scattering) and the spatial distribution of incident radiation in 2-D scatterers, we extend a numerical model based on a modification to a conventional Monte-Carlo method and applied to polycarbonate 2-D microstructures; the scattering cross-section ( $\sigma_s$ ) associated with a microtube is calculated using the infinite cylinder approximation technique (Appendix B) because the length of the microtubes is much greater than the diameter [194]. As shown in Fig. 4.18, the model deals with a two-layered structure; microtubes distributed in air are surrounded by polycarbonate rod. The sample is described by the following parameters: the thickness of layers, the radius, the refractive index ratio of inclusions to host

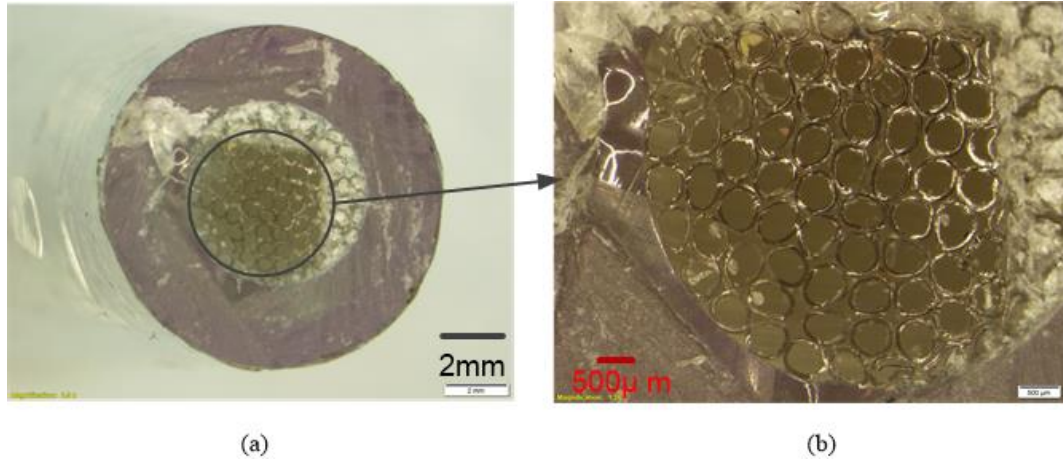


FIGURE 4.16: Optical images of polycarbonate microstructures: (a) microstructure fabricated by stacking microtubes, (b) magnified top view. Scale bars show 500  $\mu\text{m}$  resolution. As a result of cutting, the inner tubes appear closed.

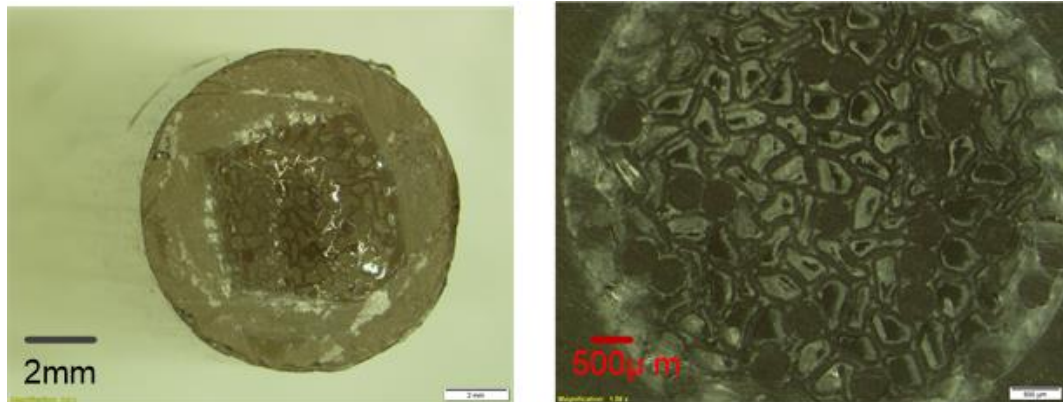


FIGURE 4.17: Optical images of polycarbonate microstructures: (a) stacking solid rods between microtubes, and (b) magnified bottom view. Scale bars show 500  $\mu\text{m}$  resolution. As a result of cutting, the inner tubes appear closed.

(m) the absorption coefficient  $\mu_a$  ( $\text{cm}^{-1}$ ) and the scattering coefficient  $\mu_s$  ( $\text{cm}^{-1}$ ) of the sample. The scattering coefficient of 2-D scatterers can be then expressed by  $\mu_s = \sigma_s N$ . Here  $N$  is the number density which can be determined by the ratio of the number of 2-D scatterers (i.e. the number of stacked microtubes) to the volume.

#### 4.6.1.3 Terahertz Diffuse Scattering

The transmitted signal from a strongly scattering medium can be considered as having two components, a ballistic (i.e. non-scattered), and a diffuse transmittance (i.e. scattered light). Both components are attenuated by absorption, depending on path

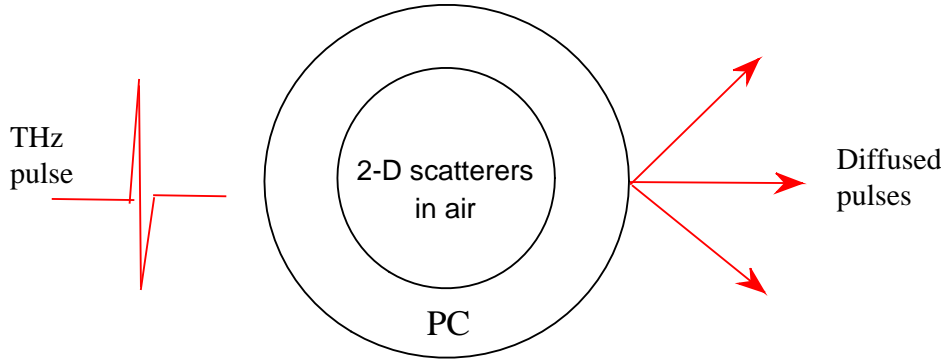


FIGURE 4.18: Monte-Carlo model for polymer microstructures with infinite height, modelled using a Monte-Carlo algorithm.

length. The path length for the ballistic photons equals the sample thickness. However, the diffused photons are also affected by multiple scattering which depends on the scattering length. The scattering length ( $l_s$ ) is related to the transport mean free path by:

$$\frac{l_{tr}}{l_s} = \frac{1}{1 - \langle \cos(\theta) \rangle} \quad (4.34)$$

where  $l_{tr}$  is the transport mean free path which is inversely proportional to the reduced scattering coefficient. The diffusive propagation requires a path length much larger than the scattering length; the photons are completely randomised and only multiply scattered photons are propagated through the sample.

Fig. 4.19 shows the THz electric field received from the samples at on-axis from the incident beam (zero degree). The main amplitude of the received pulse from samples decays by 10% as the path length increases because of multiple scattering events. Consequently, the pulse takes longer to propagate through and/or out of samples, hence its amplitude decreases. THz intensity propagated through polymer microstructures with rods decreases more than that of micro tubes, which indicates that the THz pulse followed a larger number of possible scattering paths. For example, Fig. 4.20 illustrate the intensity for polymer microstructures at  $60^\circ$ .

Fig. 4.21, shows the dependence of the received THz pulses on the angle of arrival. Compared to the microtube structure, the diffuse-scattered signal from the structure with solid rods exhibits a higher intensity at  $|\theta| > 60^\circ$ . This probably is related to solid rods being present, which makes the distribution pattern more inhomogeneous. Therefore, it seems that the diffuse intensity is the dominant factor in determining



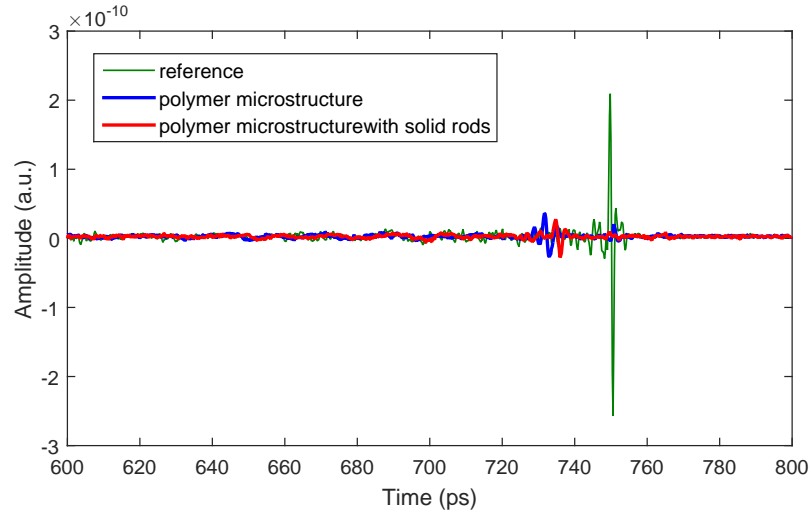


FIGURE 4.19: THz waveforms transmitted through randomly distributed polymer microstructures (blue), and solid rods (red). The reference waveform (green) has been reduced by a factor of 10.

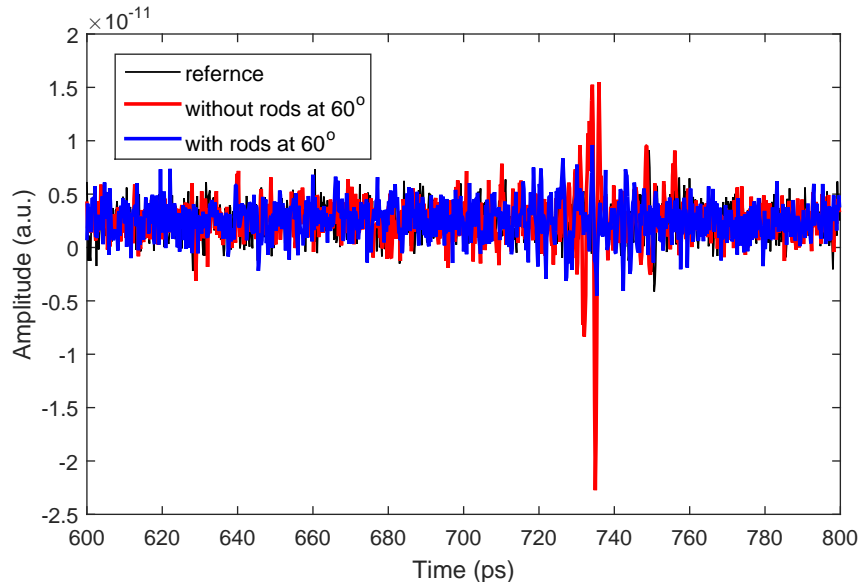


FIGURE 4.20: THz waveforms transmitted through randomly distributed polymer microstructures (red), and solid rods (blue).

the transmitted intensity, due to the random walk. The results are obtained in the frequency domain using a Fast Fourier Transform (FFT) of the time-domain data. Fig. 4.22 demonstrates the effect of the boundaries, and the structures (polymer microstructures with microtubes and/or solid rods) on the transmission spectrum. The

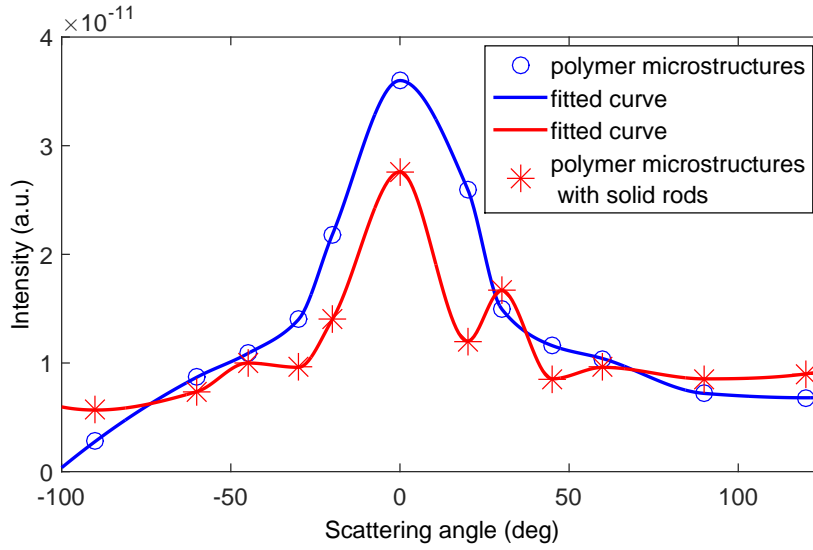


FIGURE 4.21: The amplitude of the received THz pulse as a function of angle of arrival for polymer microstructures with microtubes and with solid rods.

transmission of the beam varies exponentially with scattering and absorption loss according to equation 4.27, here  $l_s$  is related to the scattering cross-section by  $l_s = [N\sigma_s]^{-1}$ , and  $N$  is the number density of 2-D scatterers. For example, the scattering path calculated by Monte-Carlo simulation is 1.9 mm at 500 GHz. The absorption loss is the dominant factor at low frequencies ( $\sim 200$  GHz), consistent with the results shown in Fig. 4.23. At high frequencies ( $> 500$  GHz), the pulse attenuated rapidly, as scattering loss dominates. However, it appears that the presence of solid rods increases the radiation scattered away from the direction of incidence, even at 120 degrees. This can be due to the increased number of scattering events caused by solid rods and to inhomogeneity in size.

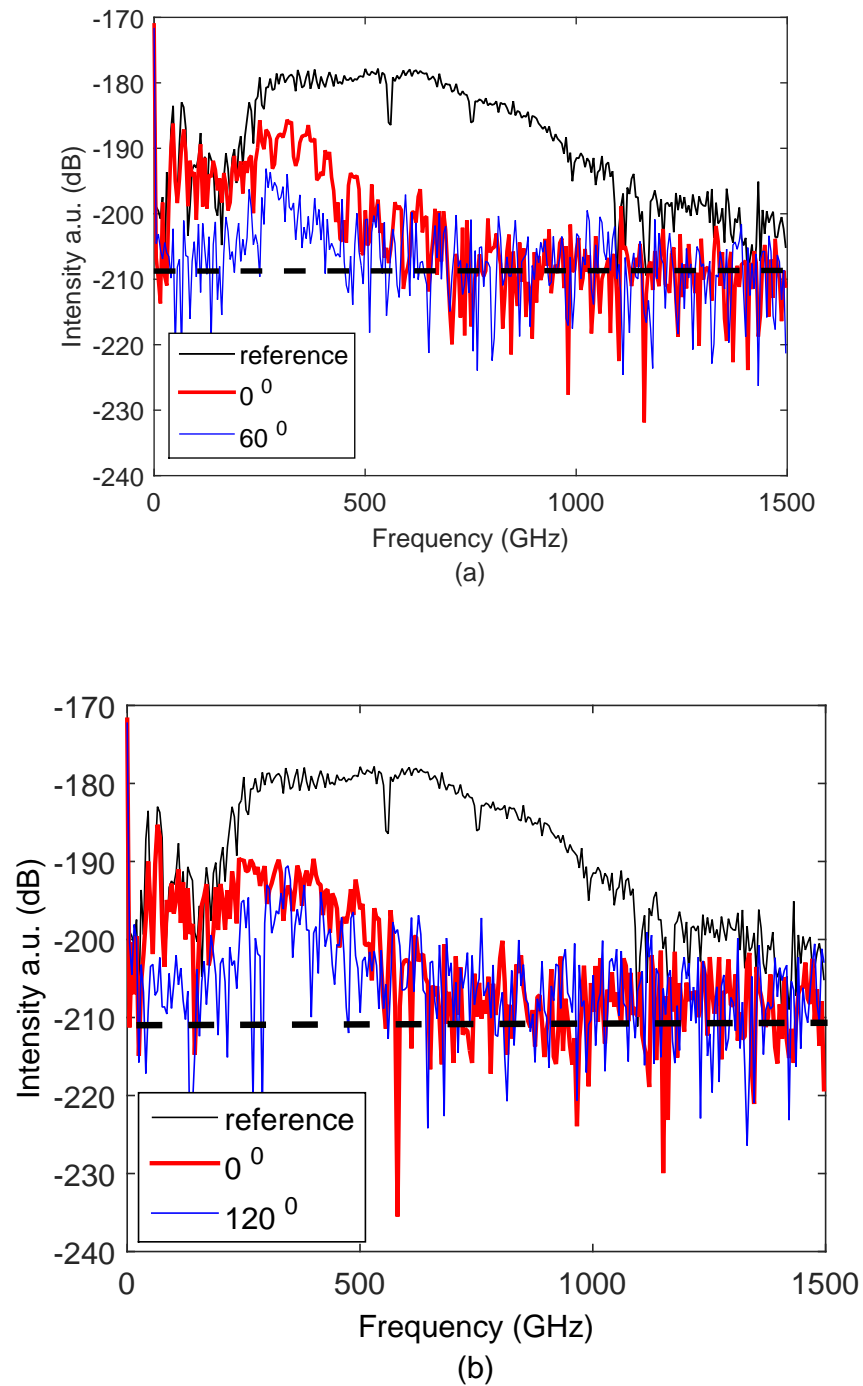


FIGURE 4.22: The spectrum of the THz pulse transmitted by taking the Fourier transform of the time-domain THz waveform for: (a) polymer microstructures without solid rods at 0 and 60 degrees, (b) the structure with solid rods at 0 and 120 degrees. [Note the weak signal transmitted from sample (a) at obtuse angles]. The dashed lines show the noise floor.

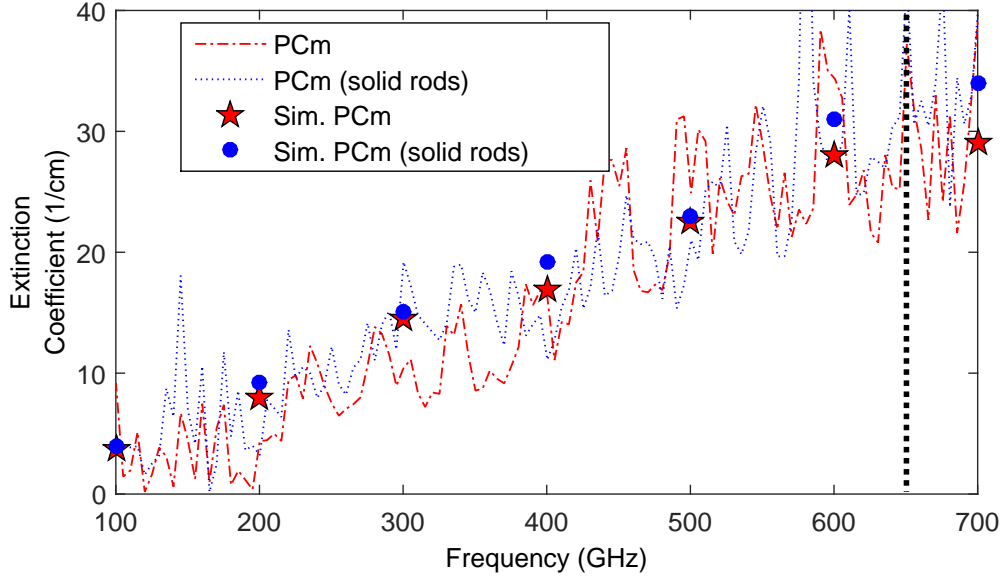


FIGURE 4.23: Experimental and simulated total attenuation coefficient, i.e. absorption plus scattering, for polycarbonate microstructures comprised of microtubes and solid rods.

Figs 4.24 and 4.25 show the radiation patterns of the THz pulse propagated at perpendicular incidence through the 2-D polymer microstructures. The results show strong scattering of the incident wave over approximately  $-90$  to  $120$  degrees (angle off-axis was limited due to insufficient SNR). The high off-axis THz transmittance indicates that most photons have been scattered out of the samples, especially from the inhomogeneous structure (polymer microstructures with rods). Inserting solid rods increases the effective refractive index of the 2-D structures, hence increases the scattering with the incident pulse being scattered away at a wide angles.

For comparison, we modelled the polycarbonate microstructures in a Monte-Carlo algorithm. The results are shown in Fig. 4.26. The simulations demonstrate a relatively good agreement with the trends observed in the angular- and frequency- dependent measurements shown in Figs 4.23, 4.24 and 4.25; most light being scattered out of the sample at large angles for high frequency components. Measurements were also taken for lower frequencies ( $<200$  GHz). Here the scattering is predominantly in the forward

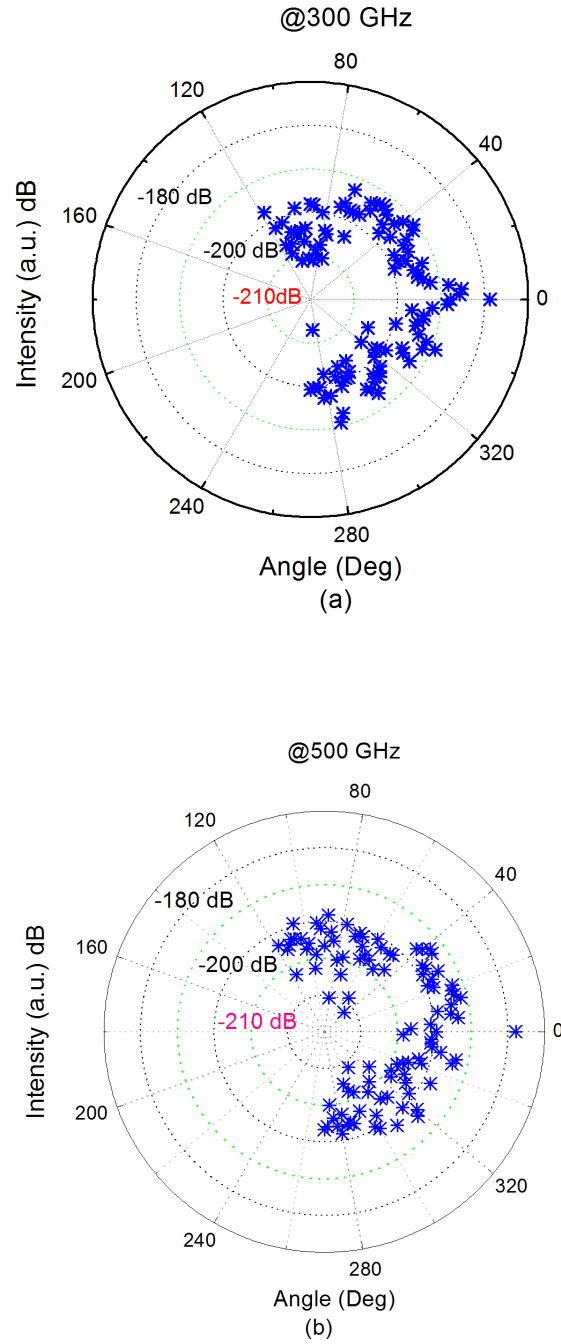


FIGURE 4.24: Measured transmission pattern following propagation of (a) a 300 GHz and (b) a 500 GHz beam through the polymer microstructures without solid rods. The sample was located in the vertical direction. -210 dB shows the noise floor.

direction as the size parameter decreases, and hence the transport paths involve a small number of scattering events; most light is propagated outside of the sample in a narrow angle.

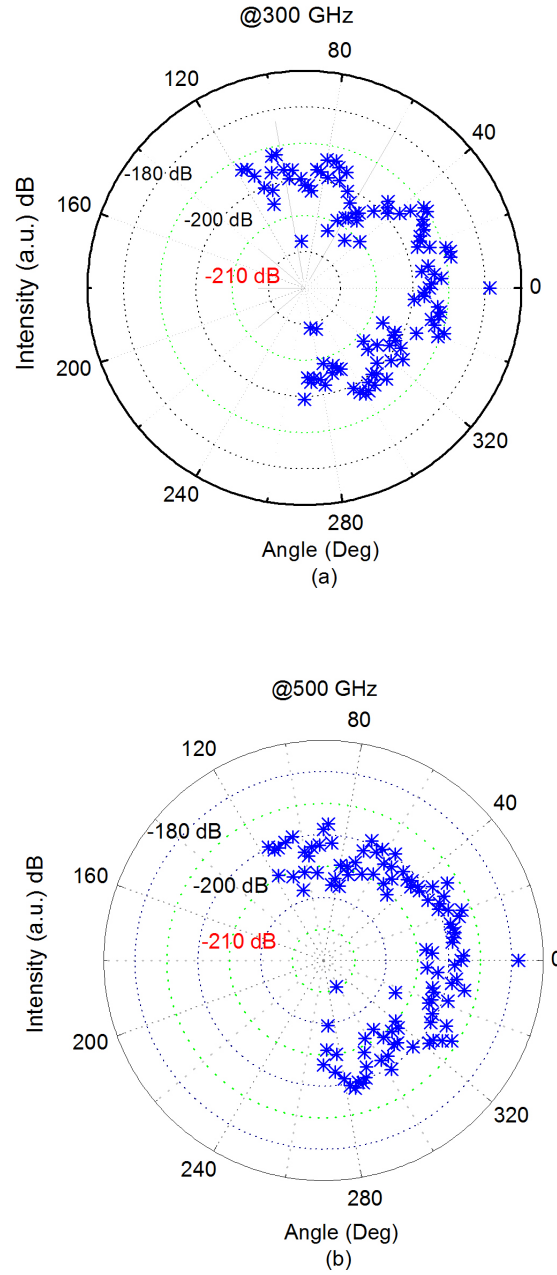


FIGURE 4.25: The scattering radiation of (a) a 300 GHz and (b) a 500 GHz beam by a 2-D polymer microstructure with 10% solid rods. -210 dB shows the noise floor.

## 4.7 Summary

A numerical model based on a Monte-Carlo algorithm has been developed to study the THz scattering in polymer composite materials. The results were in good agreement with experiments which air-polymer composite materials and 2-D polymer microstructures were used as scattering media. Measurements were taken with a THz-TDS to

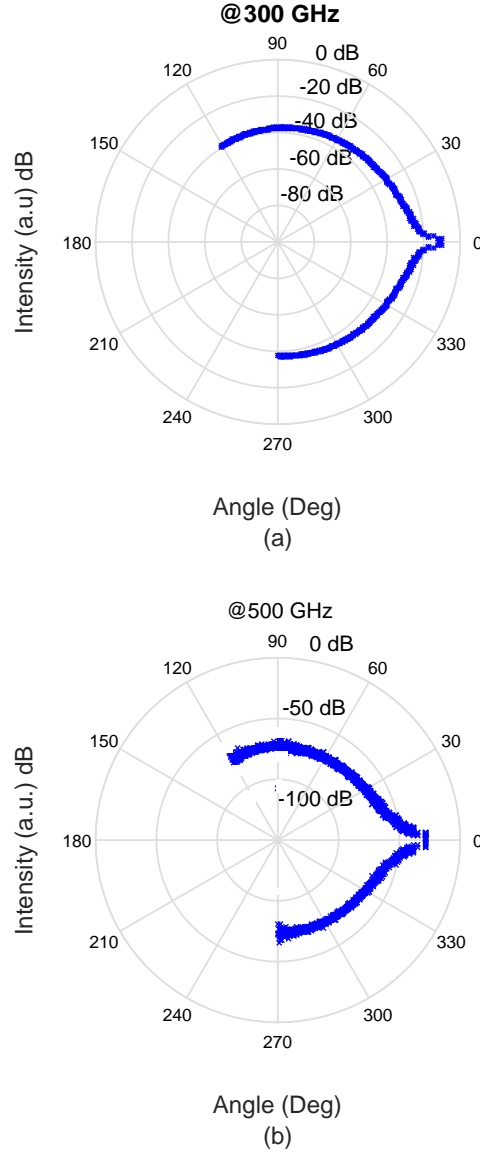


FIGURE 4.26: Simulated transmission pattern after propagation of (a) 300 GHz and (b) 500 GHz beams through polymer microstructures containing solid rods (NB: data are shown between -90 and 120 degrees to be comparable to measurements).

describe the angular- and frequency- dependent regime of THz scattering in highly scattering media.

The results show the dependence of the diffuse transmittance on various parameters, including loss, shape of boundary, reflection and refraction at boundaries. For example, 2-D polymer microstructures distributed a broadband source at a wide range of angles, over -90 to 120 degrees, while the air-polymer composite material was directive. Such a material can be useful as a THz diffuser, applicable in next generation to the short-range THz wireless communication systems. The off-axis THz transmission

in highly scattering media is also important for understanding the ratio of non-diffusive absorption and diffusive scattering length in order to reconstruct the absorption loss in the interior of materials, e.g. applicable in material identification and/or sensing.



# 5

## Polarisation of EM Waves in Strongly Scattering Composite Materials

THz scattering is a key factor affecting the characteristics, i.e. amplitude, phase and depolarisation, of THz pulse propagation in a multiply-scattering medium. We investigate the angle- and frequency-dependent polarised radiation propagated through composite materials. We also extend the numerical method developed in Chapter 4 to properly account for the prediction of the polarisation states of THz pulses in dense media.

### 5.1 Introduction

THz technology has been opening many new and interesting applications in the field of THz communications, sensing, non-destructive testing (NDT), imaging, and medical sciences [17, 195–197]. The benefits of THz radiation help to overcome restrictions of common techniques in terms of power level and bandwidth in strongly scattering media [198]. In such media, observing transmission or reflection of THz pulses can capture the sample features [199]. Scattering of the electromagnetic wave may randomise the polarisation state and direction of the incident beams [134, 200]. The transmitted

energy can be in general regarded as comprised of a ballistic (i.e. non-scattered) component, and a diffuse (i.e. scattered) component [201, 202]. The diffusive propagation depends on the transport mean free path (i.e. the photon travels an average distance  $l_{tr}$  before it is scattered) and the scattering length ( $l_s$ , i.e. the characteristic distance between random scattering events). In the weakly scattering regime,  $l_{tr} \cong l_s$  and hence the ballistic paths involve few scattering events[177]. In a strongly scattering medium, the incident wavefront encounters many scattering events, so the polarisation of the wave can become completely random.

In particular, we present a new experimental technique for studying the frequency-, and angle-dependent depolarisation of THz pulses propagating through polymer composite materials. Our aim is to investigate the impact of multiple scattering on the intensity and polarisation states of the THz pulses which are diffusely propagated out of a strongly scattering medium as a function of direction. We compare experimental results to numerical simulations based on a Monte-Carlo algorithm which incorporates polarisation and the effects of loss on the propagation of THz light through scattering media.

### 5.1.1 Polarisation of Plane Waves

The general form of the polarisation for transverse waves is represented by a Jones vector of the polarised light. The polarisation of the light travelling in the z-direction can be determined by two components of the time-varying behaviour of the electric field with angular frequency ( $\omega$ ) and wavevector ( $k$ ) as follows:

$$E = \begin{pmatrix} E_x \\ E_y \end{pmatrix} = \begin{pmatrix} E_{x0} \cos(kz - \omega t) \\ E_{y0} \cos(kz - \omega t + \delta) \end{pmatrix} \quad (5.1)$$

From equation 5.1,  $E_y$  can be expanded by an elementary transformation:

$$E_y = E_{y0} \cos(kz - \omega t + \delta) = E_{y0} \cos(kz - \omega t) \cos(\delta) - E_{y0} \sin(kz - \omega t) \sin(\delta) \quad (5.2)$$

which leads to the following equation for an ellipse:

$$\left( \frac{E_y}{E_{y0}} \right)^2 + \left( \frac{E_x}{E_{x0}} \right)^2 - 2 \left( \frac{E_y}{E_{y0}} \right) \left( \frac{E_x}{E_{x0}} \right) \cos(\delta) = \sin^2(\delta) \quad (5.3)$$

By grouping equation 5.3, the following equation is obtained:

$$(E_x^2 + E_y^2)^2 - (E_x^2 - E_y^2)^2 - (2E_x E_y \cos \delta)^2 - (2E_x E_y \sin \delta)^2 = 0 \quad (5.4)$$

The four Stokes vectors can be expressed as:

$$S = \begin{pmatrix} E_x^2 + E_y^2 \\ E_x^2 - E_y^2 \\ 2E_x E_y \cos \delta \\ 2E_x E_y \sin \delta \end{pmatrix} \quad (5.5)$$

Hence E is linearly polarised if  $\delta = 0$  or  $\pi$ ; if  $\delta = \frac{\pi}{2}$  or  $\delta = \frac{3\pi}{2}$ , the light is circularly polarised. In an experiment,  $S_0$  corresponds to the sum of the measurements with a horizontal and with a vertical polariser (i.e. the total intensity),  $S_1$  is the difference between the horizontal and vertical polarisation intensities.  $S_2$  defines the difference between the linear polarisation at  $\pm 45^\circ$ , and  $S_3$  is the difference between the left and right circularly polarised light. According to the above equation, it is possible to convert circularly polarised light into linearly and/or elliptically polarised light, if the electric field is redirected, i.e. phase changed, by a strongly scattering medium. The azimuth  $\psi$  and ellipticity  $\chi$  angles in the Poincaré sphere are defined as:

$$\begin{cases} \tan(2\psi) = \frac{2E_x E_y \cos \delta}{E_x^2 - E_y^2} \\ \sin(2\chi) = \frac{2E_x E_y \sin \delta}{E_x^2 - E_y^2} \end{cases} \quad (5.6)$$

Depolarisation refers to the variation of the electric field (E) intensity and the change in the degree of polarisation at a given point in space. The direction of E may differ and/or rotate as the wave passes through a highly scattering medium; any state of polarisation can be represented by various points on the surface of the Poincaré sphere as shown in Fig. 5.1. The coordinates of the points are the last three normalised Stokes vector,  $\{S_1, S_2, S_3\}$ , describing the degree of polarisation (DOP). The degree of polarisation, regardless of whether the light is linearly and/or circularly polarised, is given as:

$$DOP = \frac{\sqrt{(S_1^2 + S_2^2 + S_3^2)}}{S_0} \quad (5.7)$$

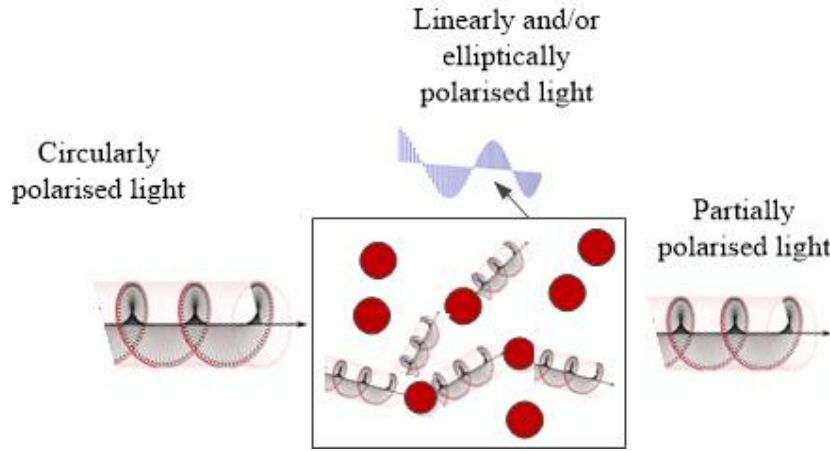


FIGURE 5.1: Helicity of circularly polarised light changes when the photon is scattered. As a possibility, the plane of  $S_1$ - $S_3$  can change to  $S_1$ - $S_2$  (blue signal)

The degree of linear ( $DOP_L$ ) and circular polarisation ( $DOP_C$ ) can be expressed as:

$$DOP_L = \frac{\sqrt{(S_1^2 + S_2^2)}}{S_0}, \quad DOP_C = \frac{S_3}{S_0} \quad (5.8)$$

where  $DOP=1$  indicates completely polarised light;  $DOP<1$  means the light is partially polarised;  $DOP=0$  corresponds to unpolarised light. The number of scattering events and the path length associated with single and/or multiple scattering should be evaluated in order to determine how depolarisation proceeds as the size of the particles varies. For example, the contribution of single scattering is predominant for a medium with a rather small dimension of scattering volume and small particles, i.e. the Rayleigh scattering regime. The angular dependence of single scattering in a highly scattering medium is shown in Fig. 5.2.

The scattering is highly anisotropic for a large size parameter ( $x > 1$ ) and hence the transport mean free path ( $l^*$ ) is much larger than the scattering length ( $l = \frac{1}{\sigma_{sf}}$ ). The distribution of scattering path lengths ( $s$ ) can be obtained using the Green's function of the diffusion equations, and the degree of polarisation can be expressed by [113, 173]:

$$P \approx \frac{\int_0^\infty \rho(s) f(s) ds}{\int_0^\infty \rho(s) ds} \quad (5.9)$$

where  $\rho$  is the probability density of the optical path and  $f(s)$  the dependence of DOP

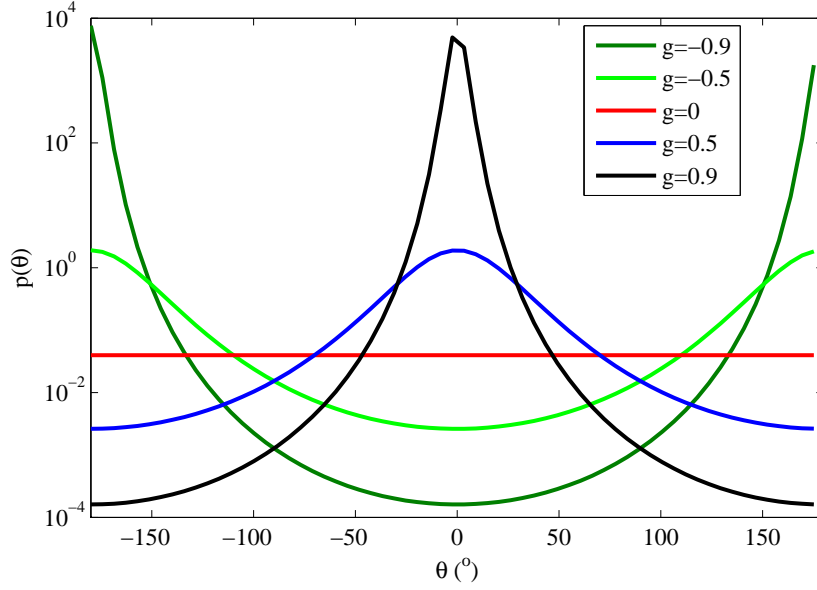


FIGURE 5.2: A series of Henyey-Greenstein functions for different anisotropy factors ( $g$ ).

for a number of scattering ( $n$ ). In the large  $n$ -limit,  $f(s)$  can be expressed as:

$$f_L(n) \cong \frac{3}{2} \exp[-n(l/\zeta)] \quad (5.10)$$

where  $\zeta$  defines the characteristic length of depolarisation for incident linearly polarised light ( $\zeta_L = l/(\ln \frac{10}{7})$ ) and for circularly polarised light ( $\zeta_C = l/(\ln 2)$ ). From equation 5.9 the degree of polarisation of the transmitted light is given by:

$$P_i = \frac{d \sinh \left\{ \frac{l}{\xi_i} \right\}}{l \sinh \left\{ \frac{d}{\xi_i} \right\}} \quad (5.11)$$

where  $d$  is the slab thickness,  $\xi_i = (\zeta_i l/3)^{1/2}$  with  $i=L, C$ . The probability density function is:

$$p(s) = \mu_t \exp(-\mu_t s) \quad (5.12)$$

As Fig. 5.3 shows, in the case of large particles the circularly polarised light exhibits a high degree of polarisation memory compared with linearly polarised light. By decreasing the size parameter, the number of scattering event increases in which an asymmetry between forward and backward scattering directions can appear (i.e. Rayleigh regime); the direction and the helicity of circular polarisation are randomised and hence its characteristic length of depolarisation is greater than that of linearly

polarised light.

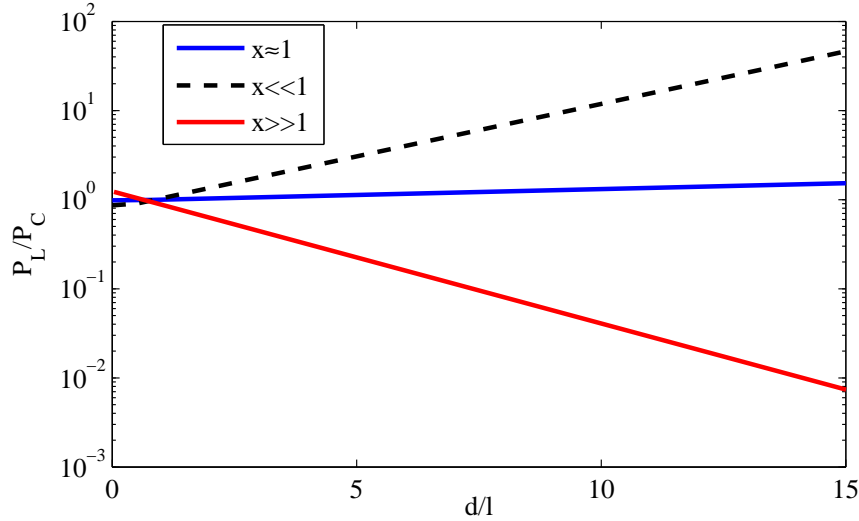


FIGURE 5.3: The ratio of the degree of polarisation as a function of  $d/l$ , for three values of size parameter ( $x$ ).

Although the Jones vector can express the polarisation, it cannot deal with depolarising interaction and partial polarisation because the light cannot be traced due to spatial inhomogeneities. Therefore, it is not suitable for multiply scattering media. In such case, Muller matrix can be used to describe the effect of scattering on the observed polarisation.

## 5.2 Polarisation Model for Monte-Carlo

Hielscher *et al.* introduced a Stokes vector/Mueller matrix approach into the method to calculate the complete polarisation properties of light [203]. Afterwards, several techniques based on the Monte-Carlo technique have been developed to model polarised light propagation in turbid media [204–207]. The Mueller matrix was used to express the effects of a scattering system on the polarisation of light, represented by the Stokes vector [208–210]. Each photon is initially assigned a value of arbitrary polarisation state in the Stokes vector,  $S = [S_0, S_1, S_2, S_3]$ . The Stokes vector is defined by the

components:

$$\begin{aligned}
 S_0 &= I \\
 S_1 &= I \cos 2\theta \cos 2\varphi \\
 S_2 &= I \cos 2\theta \sin 2\varphi \\
 S_3 &= I \sin 2\theta
 \end{aligned}
 \tag{5.13}$$

where  $\theta$  is the polar angle, and  $\varphi$  is the azimuthal angle.  $I$  is total intensity,  $S_1$  polarisation at  $0^\circ$  or  $90^\circ$  to the scattering plane,  $S_2$  polarisation at  $\pm 45^\circ$ , and  $S_3$  left or right circular polarisation. In the case of polarised light:

$$S_0^2 = S_1^2 + S_2^2 + S_3^2 \tag{5.14}$$

Equation (5.14) defines a sphere which is known as the Poincaré sphere (shown in Fig. 5.4).

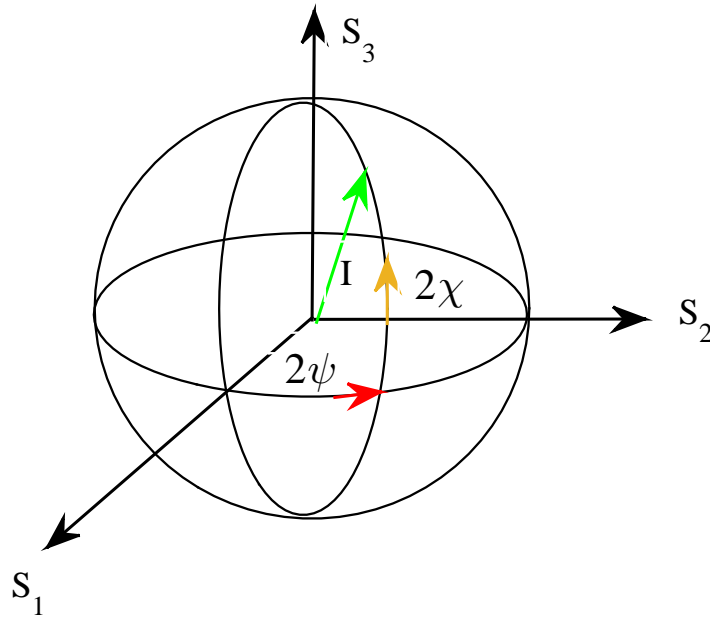


FIGURE 5.4: Poincaré sphere with the three Stokes parameters.

### 5.2.1 Polarisation

A fundamental problem in Monte-Carlo with polarisation information is the choice of the angle of rotation into the scattering plane. In a scattering event, a polar angle ( $\psi$ ) and scattering angle (using equation 4.16 must be determined to calculate the state after scattering. To determine  $\psi$ , the phase function ( $\theta, \psi$ ) of spheres for an incident with a Stokes vector is used:

$$\rho(\psi, \chi) = \frac{a(\psi) + b(\psi) [S_1 \cos(2\chi) + S_2 \sin(2\chi)]}{S_0} \quad (5.15)$$

When the scattering angle ( $\psi$ ) is known, the azimuthal angle ( $\chi$ ) can be calculated using the probability density function (PDF):

$$\rho(\chi) = 1 + \frac{b(\psi)}{a(\psi)} \left[ \frac{S_1 \cos(2\chi) + S_2 \sin(2\chi)}{S_0} \right] \quad (5.16)$$

$\chi$  is calculated by integrating the above PDF from 0 to  $\chi$ :

$$P = \frac{1}{2\pi} \left\{ \chi + \frac{b(\psi)}{a(\psi)} \frac{[S_1 \sin(2\chi) + S_2 (1 - \cos(2\chi))]}{S_0} \right\} \quad (5.17)$$

The Stokes vector of the photon after scattering is then given by:

$$S_{new} = R(-\chi) M(\psi) R(\chi) S_{old} \quad (5.18)$$

where

$$R(\chi) = \begin{bmatrix} 1 & 0 & 0 & 0 \\ 0 & \cos(2\chi) & -\sin(2\chi) & 0 \\ 0 & \sin(2\chi) & \cos(2\chi) & 0 \\ 0 & 0 & 0 & 1 \end{bmatrix} \quad (5.19)$$

and



$$M(\psi) = \begin{bmatrix} a(\psi) & b(\psi) & 0 & 0 \\ b(\psi) & a(\psi) & 0 & 0 \\ 0 & 0 & d(\psi) & -c(\psi) \\ 0 & 0 & c(\psi) & d(\psi) \end{bmatrix} \quad (5.20)$$

where

$$\begin{aligned} a(\psi) &= \frac{1}{2} (|S_2|^2 + |S_1|^2) \\ b(\psi) &= \frac{1}{2} (|S_2|^2 - |S_1|^2) \\ c(\psi) &= \frac{1}{2} (S_2 S_1^* + S_1 S_2^*) \\ d(\psi) &= \frac{i}{2} (S_2 S_1^* - S_1 S_2^*) \end{aligned} \quad (5.21)$$

R is the rotation matrix and M is the single scattering event matrix calculated from Mie theory,  $S_1$  and  $S_2$  can be found in reference [128]. In our Monte-Carlo algorithm,  $S_1$  and  $S_2$  for every scattering event are obtained from Mie scattering theory.  $S_{new}$  and  $S_{old}$  are the Stokes vectors before and after the scattering event, respectively. The Stokes vectors for states of circularly and linearly polarised are as:

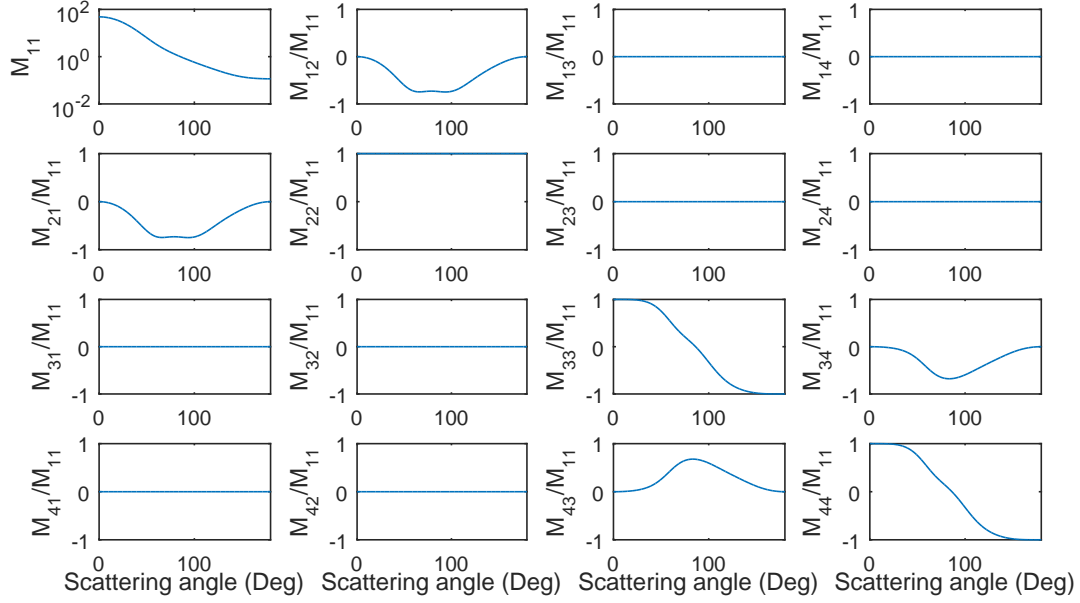
$$S_L = \begin{pmatrix} 1 \\ \pm 1 \\ 0 \\ 0 \end{pmatrix}, S_C = \begin{pmatrix} 1 \\ 0 \\ 0 \\ \pm 1 \end{pmatrix} \quad (5.22)$$

Fig. 5.5 shows the M matrix for an air bubble with a radius of 200  $\mu\text{m}$  in polycarbonate at 500 GHz. The main steps to the simulation shown in Fig. 5.28.

### 5.3 Discussion

The light depolarisation process through the highly scattering medium depends on whether the light is circularly or linearly polarised. Moreover, scattering events can be governed by the geometry of sample, the size of air bubbles, and their volume fraction (e.g. forward scattering dominates as the number of scattering events decreases as the size parameter decreases) [121, 211–213].

The degree of polarisation is calculated using the mean value of the Stokes parameters of photons escaping from boundaries ( $X_1$  and  $Y_1$ ). For example, Fig. 5.6 shows the effect of size parameter,  $x=ka$  where  $k$  is wave number and  $a$  is radius of inclusions,


 FIGURE 5.5: M matrix for an air bubble with radius  $400 \mu\text{m}$  in polycarbonate.

on the polarisation ratio of light transmitted from  $Y_1$ . While the degree of polarisation (DOP) for a circularly polarised (CP) source tends to decrease slowly with increasing size parameter, the DOP from a linearly polarised (LP) source comes mainly from low scattering. So, the circularly polarised light can survive from multiple scattering events as shown in Figs 5.7 and 5.8. The difference between the two types of behaviour corresponding to  $ka > 1.6$  comes from the anisotropy ( $g$ ) property of the scattering. The strong scattering reduces the anisotropy coefficient, so that the circular character is affected by the scattering directions.

The last three components of the normalised Stokes vector ( $S_0, S_1, S_2, S_3$ ) of photons leaving the top and bottom surfaces as calculated by our model are shown in Figs 5.9, 5.10, 5.11, and 5.12 for a 120 GHz circularly and linearly polarised source, respectively, through a  $3 \times 10 \text{ mm}^2$  slab. Degree of polarisation of the transmitted light from the sample is also summarised in Table A.1, which shows the number of scattering events at 120 GHz is insufficient to randomise the direction and helicity of circularly polarised light.

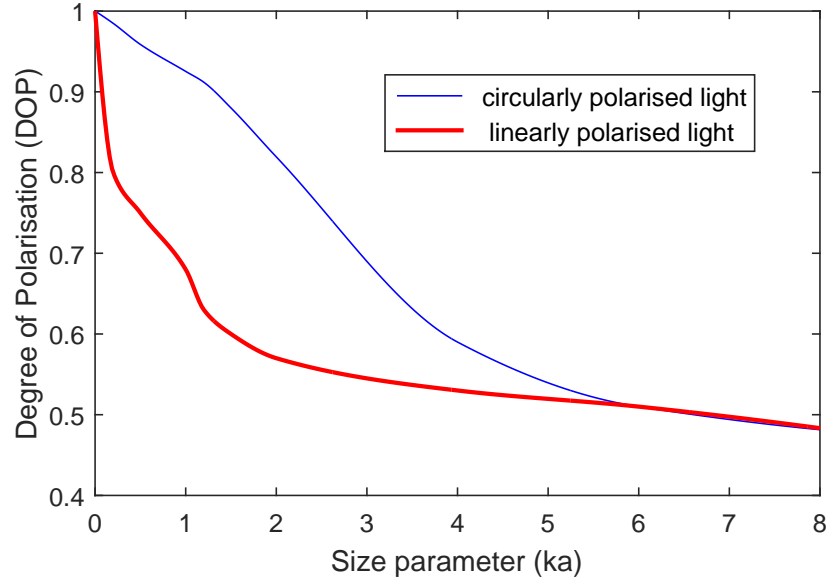


FIGURE 5.6: Effect of size parameter with the same volume fraction in a sample with  $Y \times X = 1 \times 10 \text{ mm}^2$  dimension on DOP of linearly polarised and circularly polarised light transmitted vertically from  $Y_1$ .

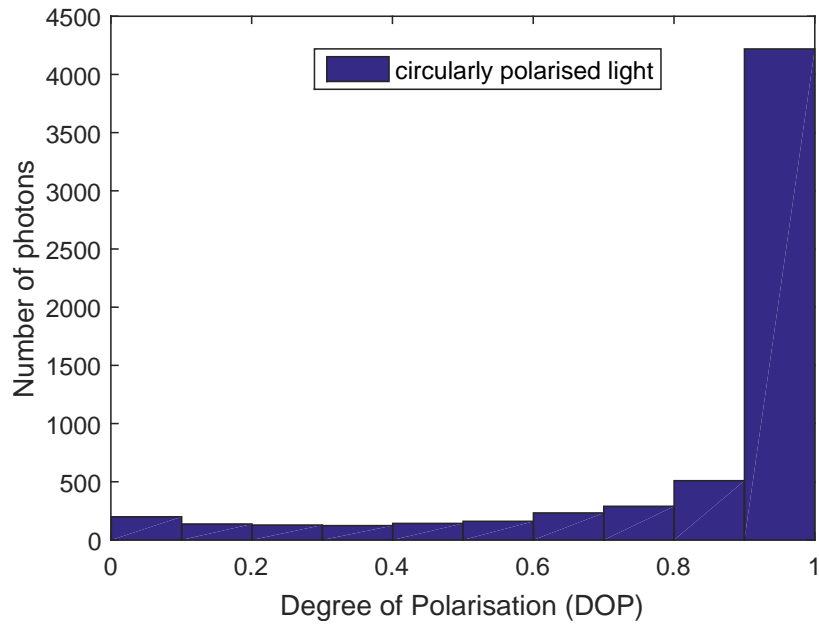


FIGURE 5.7: DOP statistics of the sample described in the text after propagation of circularly polarised light at 120 GHz. The light transmitted from  $Y_1$ .

Fig. 5.9 and 5.10 show that the light remains largely linearly polarised (LP) though the angle of LP source is randomised. However, from equation 5.4 the expression for

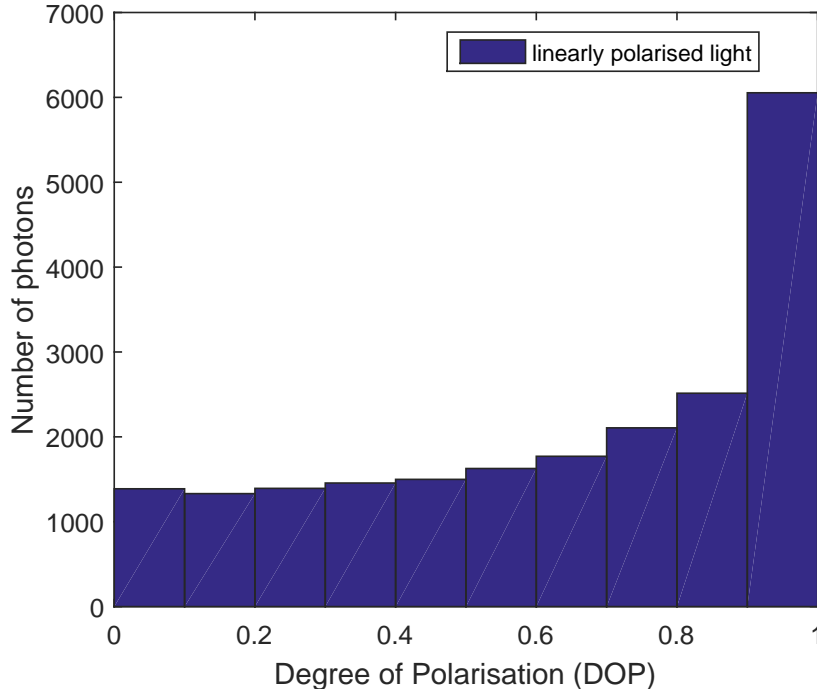


FIGURE 5.8: DOP statistics of the sample described in the text after propagation of linearly polarised light at 120 GHz. The light transmitted from  $Y_1$ .

TABLE 5.1: DOP of linearly and circularly polarised light transmitted at orthogonal boundaries. Their normalized Stokes vectors are Shown in Figs 5.10 to 5.13

Boundaries (Sample dimension: $3 \times 10 \text{ mm}^2$ )	DOP of linearly polarised light at 120 GHz	DOP of circularly polarised light at 120 GHz
$X_1$	0.61	0.985
$Y_1$	0.68	0.95

circularly polarised source is:

$$E = E_0 \left[ \cos(\omega t - kz + \delta) a'_x + \sin(\omega t - kz + \delta) a'_y \right] \quad (5.23)$$

which shows that the circularly polarised light depends on the direction of the field.

Combining equations 5.18, 5.19, 5.20 5.21, and 5.22 shows that for a polar angle

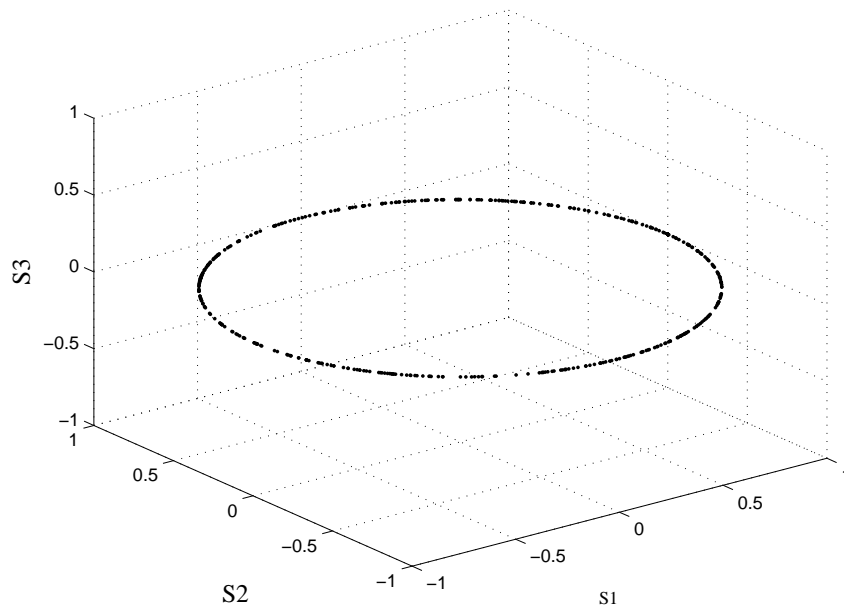


FIGURE 5.9: The Stokes parameters of transmitted light from the surface of  $X_1$  after propagation of a 120 GHz linearly polarised beam through a  $Y \times X = 1 \times 10 \text{ mm}^2$  slab with randomly distributed air bubbles in polycarbonate.

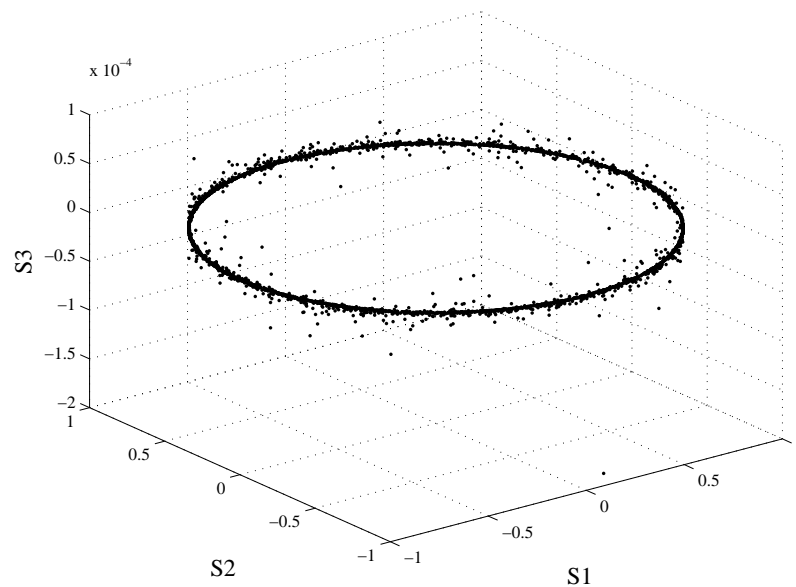


FIGURE 5.10: The Stokes parameters of transmitted light from the surface of  $Y_1$  after propagation of a 120 GHz linearly polarised beam through a  $Y \times X = 3 \times 10 \text{ mm}^2$  slab with randomly distributed air bubbles in polycarbonate.

$\chi = \frac{\pi}{2}$ , the circularly polarised light may change to a linearly polarised wave. This condition can be met by a large number of scattering events as the polar angle depends on the direction of the electric field, hence the Poincaré sphere of circularly polarised light markedly depends on the direction of scattering as shown in Figs 5.11 and 5.12. For example, when circularly polarised, the light that is forward scattered preserves the original polarisation states; the polarisation states of the photons transmitted from  $X_1$  remain clustered around the  $S_3$ -axis as shown in Fig. 5.11. However, Fig. 5.12 illustrates multiple scattering randomly changes the polarisation states at the  $Y_1$  boundary. To further illustrate the changes in circular polarisation induced by multiple scattering; Fig. 5.13 shows the Poincaré sphere for output light from  $Y_1$  at 500 GHz. From

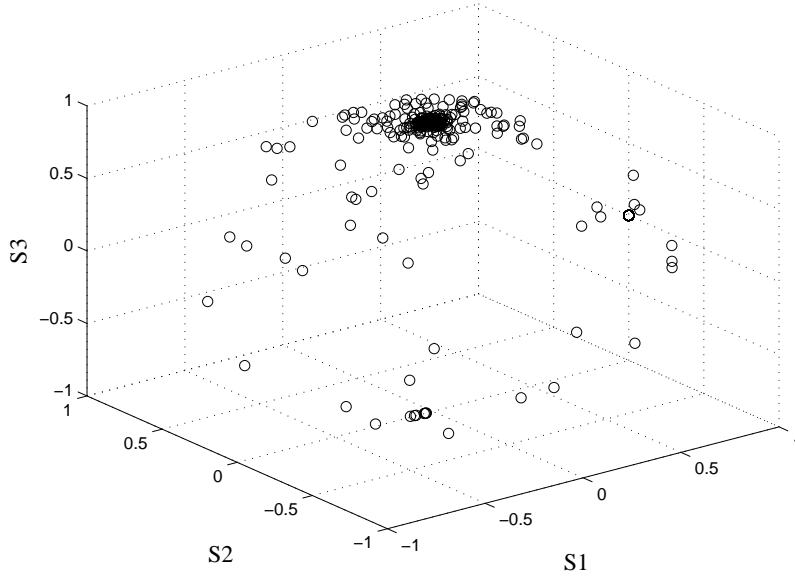


FIGURE 5.11: Dependence of the transmitted light for a circularly polarised beam on the transmission direction from the surface of  $X_1$  after propagation of a 120 GHz circularly polarised beam through a  $Y \times X = 3 \times 10 \text{ mm}^2$  slab with randomly distributed air bubbles in polycarbonate.

this figure the flip in the plane of the circularly polarised light can clearly be seen as the polarisation vectors transit to the  $S_1$ - $S_2$  plane; the degree of polarisation of the transmitted wave is 0.48. Therefore, two mechanisms control the polarisation state of circularly polarised light: the randomisation of the direction and the helicity of the field [207, 212, 213].

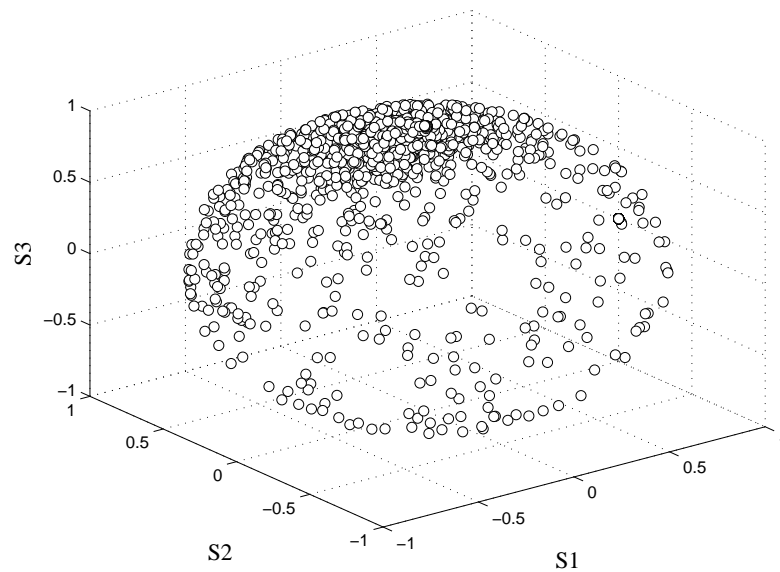


FIGURE 5.12: Dependence of the transmitted light for a circularly polarised beam on the transmission direction from the surface of  $Y_1$  after propagation of a 120 GHz circularly polarised beam through a  $Y \times X = 1 \times 10 \text{ mm}^2$  slab with randomly distributed air bubbles in polycarbonate.

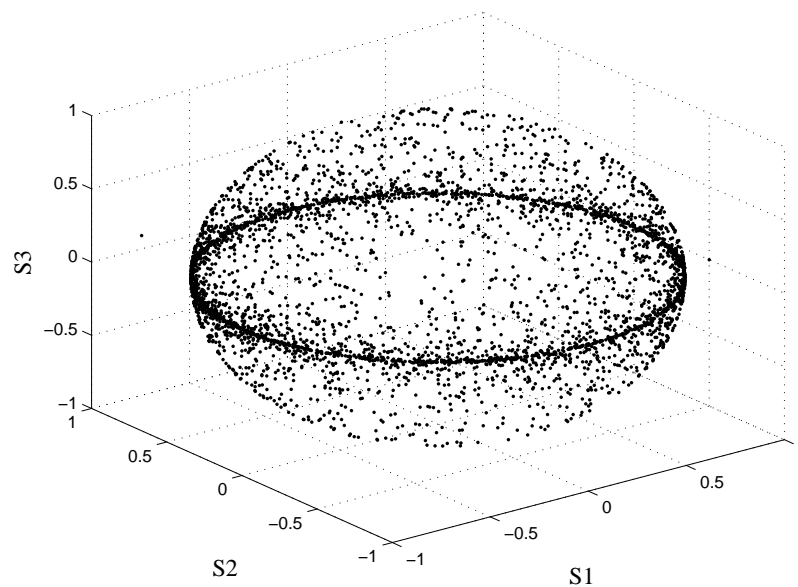


FIGURE 5.13: The Poincaré sphere of transmitted light from the surface of  $Y_1$  for 500 GHz circularly polarised light through a  $Y \times X = 1 \times 10 \text{ mm}^2$  slab with randomly distributed air bubbles in polycarbonate.

### 5.3.1 Polarisation Dependant THz Scattering

#### Air-Polycarbonate Composite Materials:

To evaluate the effect of the polarisation on the THz diffuse scattering time-domain, the THz pulses were recorded with both angle on- and off-axis from the incident beam. The type of polarisation noticeably affects the amplitude of the detected pulses. Fig. 5.14 shows that the amplitude of the diffused THz pulse received from the thin sample (i.e.  $L=1$  mm) for the linearly polarised light. There is an increasing time delay for x polarisation which indicates that the x-polarised light followed a larger number of possible scattering paths than the y-polarised light, and thus the total scattering loss increases by launching x-polarised light into the sample; the main amplitude of the received pulse for the x-polarised light is decayed by 10 than the y-polarised light. As shown in Fig. 5.15, the difference is due to the fact that multiple scattering in

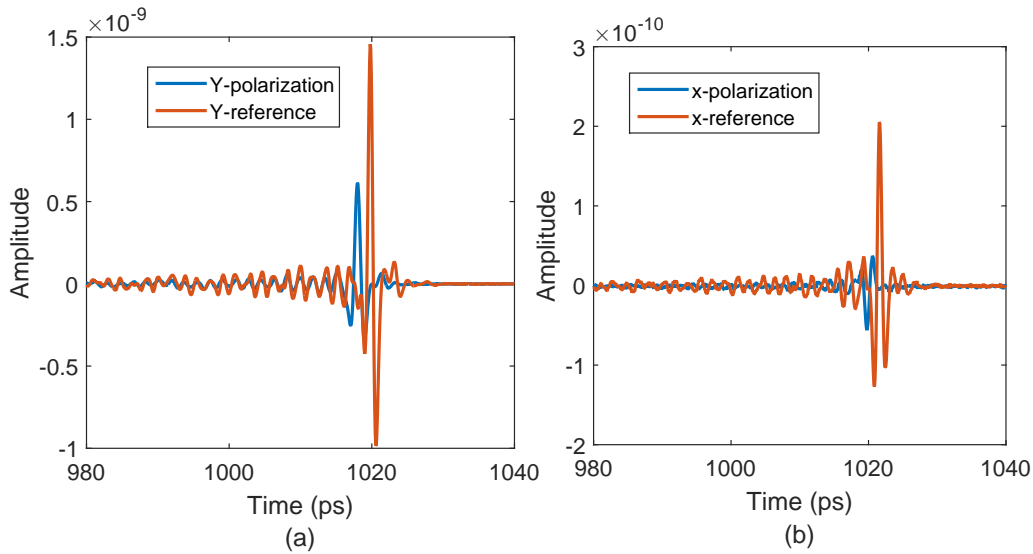


FIGURE 5.14: Time-domain THz waveform measured with THz-TDS for the thin sample,  $L=1$  mm, for the linear polarisation components: (a) y-polarisation, and (b) x-polarisation.

the sample sequences favor the vertical (y) polarisation light, because the scattering angle is mainly restricted to a narrow angle about to the incident light (horizontal) and thus the paths of length contribute differently to each linear polarisation. When the frequency increases, the size parameter increases and thus the scattering becomes highly anisotropic. In this case, the transport path is longer than scattering length, so that the scattering events increases in which multiple scattering leads to a high depolarisation ratio and then reducing the effect of polarisation-dependent scattering.



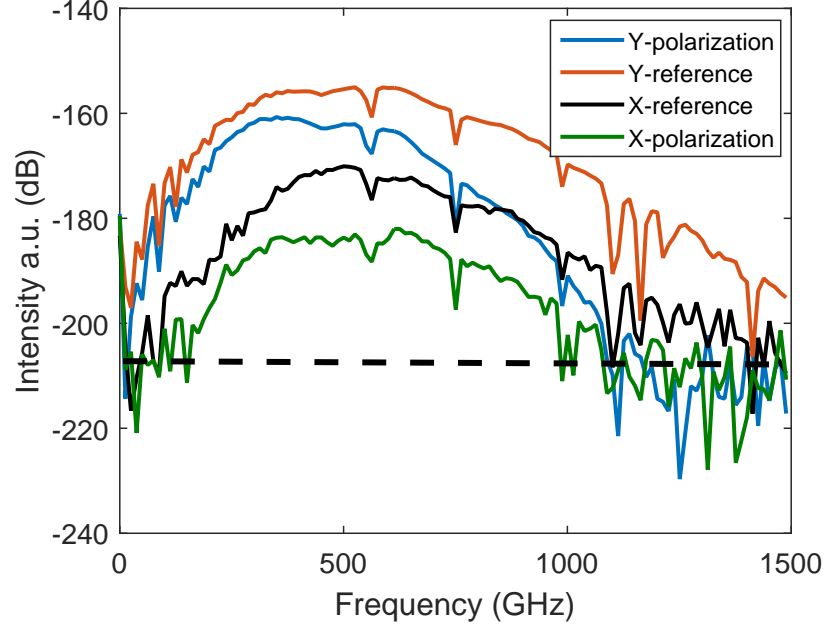


FIGURE 5.15: Intensity for x- and y-polarised light propagating through the sample ( $L=1$  mm).

## 2-D Scatterers:

Measurements were also repeated for different linear polarisation, by rotating the receiver antenna and the corresponding wire-grid polariser by  $90^\circ$  to understand whether the structures give polarisation-dependent THz scattering. To determine the polarisation-dependent scattering in the samples, we also measured the transmission spectra for the orthogonal polarised light. However, the two linear polarisation components propagating through the samples exhibit no received signal, implying no change in polarisation during propagation as shown in Fig. 5.16.

## Gold Coated Silica Microspheres:

In this section, we study angle-dependent measurements of polarised THz radiation, propagated through a gold coated silica-polyethylene composite material. The aim is to show how depolarisation changes with angle off-axis and frequency. The number of scattering events and then path length associated with single and/or multiple scattering

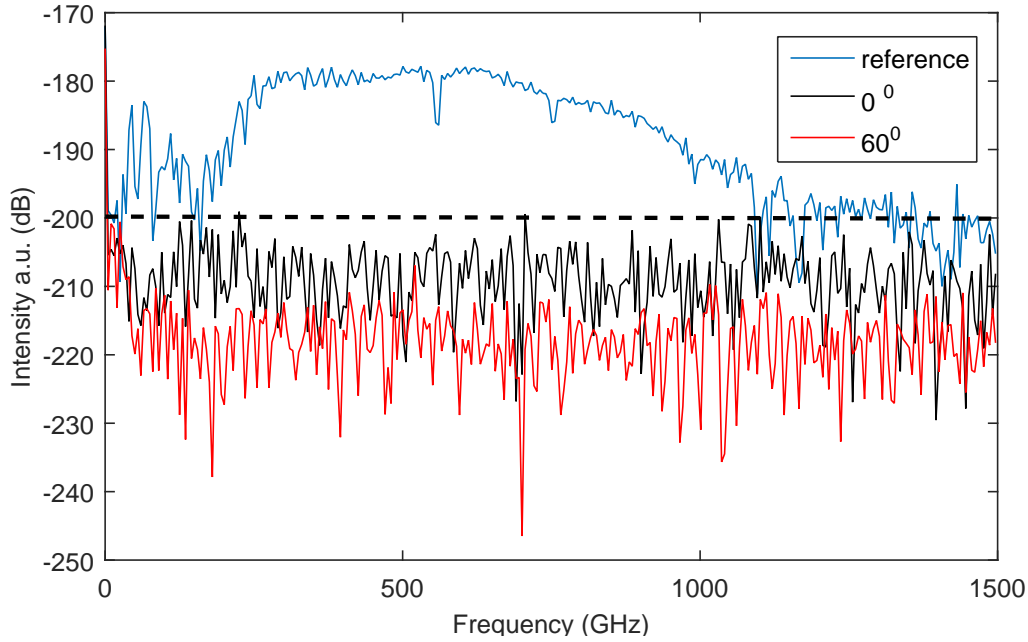


FIGURE 5.16: Depolarisation ratio for linearly polarised light as a function of frequency for angles of  $0^\circ$  and  $60^\circ$ .

should be evaluated in order to determine how depolarisation proceeds as the size parameters varies (i.e.  $x = 2\pi a/\lambda$ ,  $a$  is radius of spheres). For example, the contribution of single scattering is predominant for a medium with low volume fraction of scatterers and small particles, i.e. the Rayleigh scattering regime [200]. Scattering is highly anisotropic for a large size parameter ( $k > 1$ ) and hence the transport mean free path ( $l$ ) is much larger than the scattering length ( $l_s$ ).

### 5.3.1.1 Experimental Method

Gold-coated silica microspheres (provided from Cospheric company) with diameter in the distribution  $30\text{-}300\text{ }\mu\text{m}$  were dispersed with 30 % volume fraction in polyethylene nanopowder. The resulting material was contained in a round polyethylene cuvette with a diameter of 1 cm. Gold and polyethylene are excellent materials for THz scattering studies because of their very low absorption coefficients at terahertz frequencies, resulting in a strongly scattering medium with long transport paths. The experimental set up is illustrated in Fig. 5.17. The THz pulses were focused into the random medium, and the emerging radiation was measured over  $-90$  to  $120$  degrees relative to the incident beam. The THz scattering were detected with a  $2^\circ$  resolution for the sample, empty cuvette and a reference to correct the variation of the transmission as

a result of the cuvette thickness. To suppress the measurement of cross-polarised radiation, wire-grid polarisers were placed in front of the receiver and emitter antennas. To measure the depolarisation ratio, two sets of measurements were taken with the receiver antenna and the corresponding polariser turned by  $90^\circ$  relative to the source.

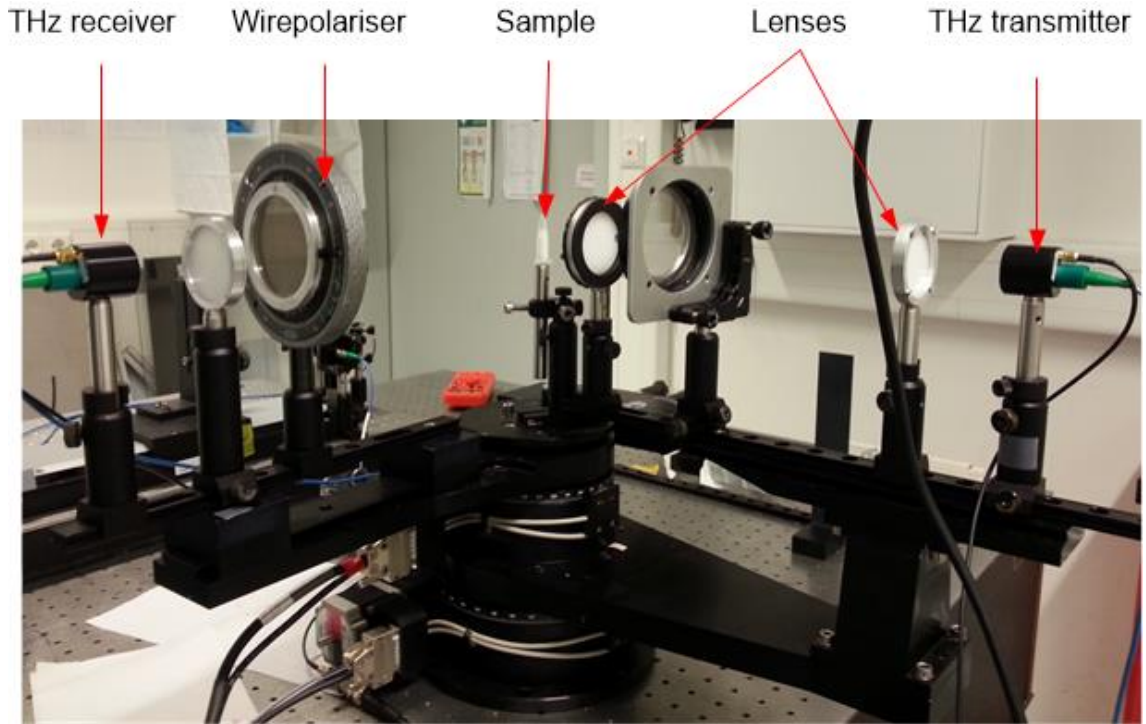


FIGURE 5.17: The experimental arrangement for measurements of angle-dependent THz scattering in strongly scattering media.

### 5.3.2 Results

Fig. 5.18 indicates the diffusion regime in the sample, predicted by the Monte-Carlo algorithm. It shows that the scattering length dramatically decreases with frequencies higher than 500 GHz because of the scattering loss;  $l_s$  is less than 0.1 of the transport length (10 mm).

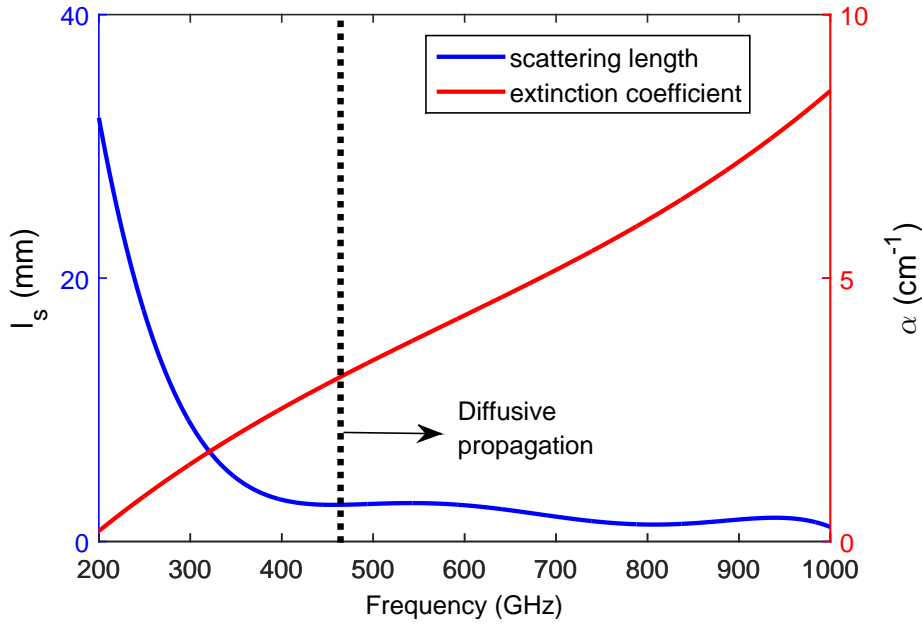


FIGURE 5.18: Scattering length and total loss predicted by the developed Monte-Carlo model. The dashed line shows the diffusion regime.

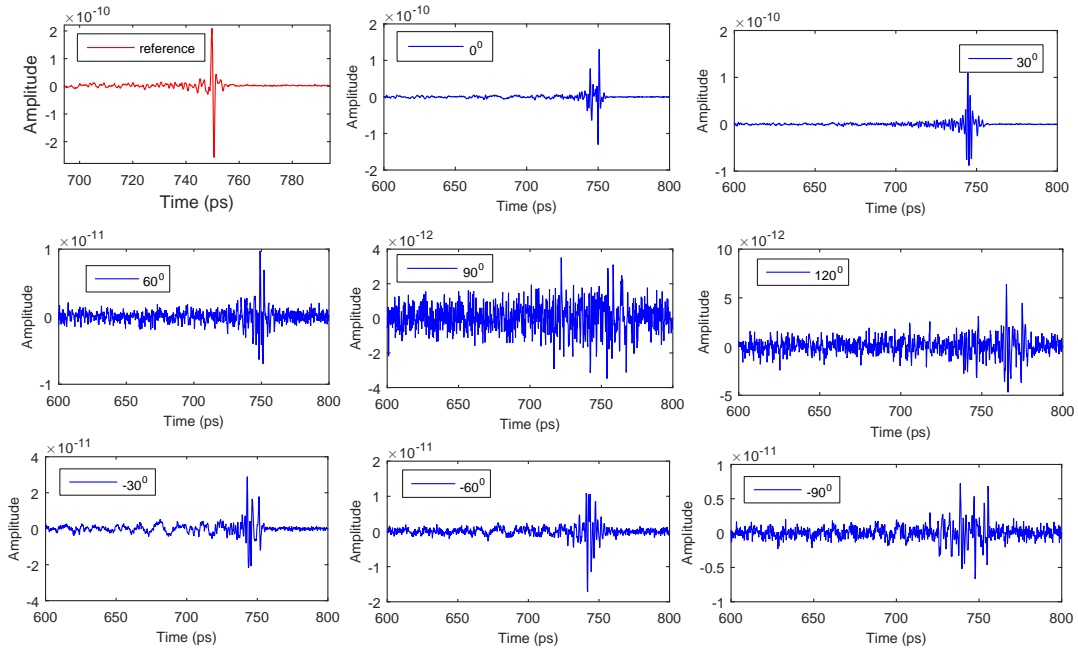


FIGURE 5.19: Time-domain THz waveform measured with THz-TDS for the sample at different angles .

The magnitude of equation 4.27 gives the frequency-dependent THz scattering for different angles as shown in Figs 5.20 and 5.21. At high frequencies (>200 GHz), the scattering loss increases, with most of the short wavelength components of the incident pulse being diffused. The attenuation due to scattering dominates at negative angles relative to the incident beam; the bandwidth of the THz signal is reduced to 800 GHz. This can be due to the inhomogeneity of scatterers in their distribution and size.

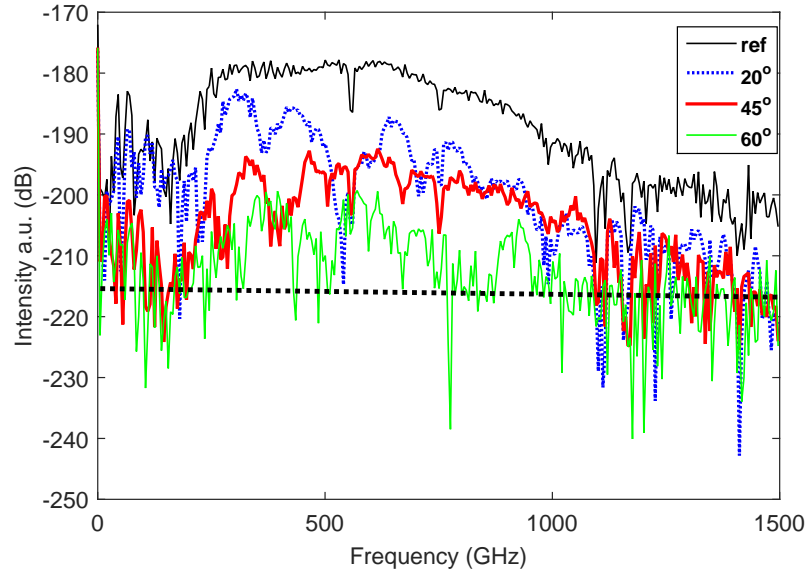


FIGURE 5.20: THz signals transmitted through a random medium consisting of gold coated silica microspheres at positive angles and (b) negative angles from the incident beam. The dashed lines show the noise floor.

We also determine the spectral phase, shown in Fig. 5.22, to extract the refractive index shown in Fig. 5.23. The phase function at on-axis THz transmission shows nonlinear behaviour because the THz pulses experienced more scattering events at narrow angles. Fig. 5.22 also indicates the angle and frequency dependence of the mean free path. For example, the spectral phase at  $-45^\circ$  between 200 to 700 GHz is linear whilst the linear behaviour for  $-20^\circ$  shifts to 300-500 GHz. These measurements allow to distinguish the effects of multiple scattering in the depolarisation and attenuation of the THz signal at the frequency and angle of interest.

At frequencies less than 700 GHz, the refractive index exhibits a high dispersive effect due to multiple scattering. The scattering loss in the medium calculated using equation 4.27 determines the scattering path, according to  $l_s = 1/(\sigma_s N)$ . Here  $N$  is

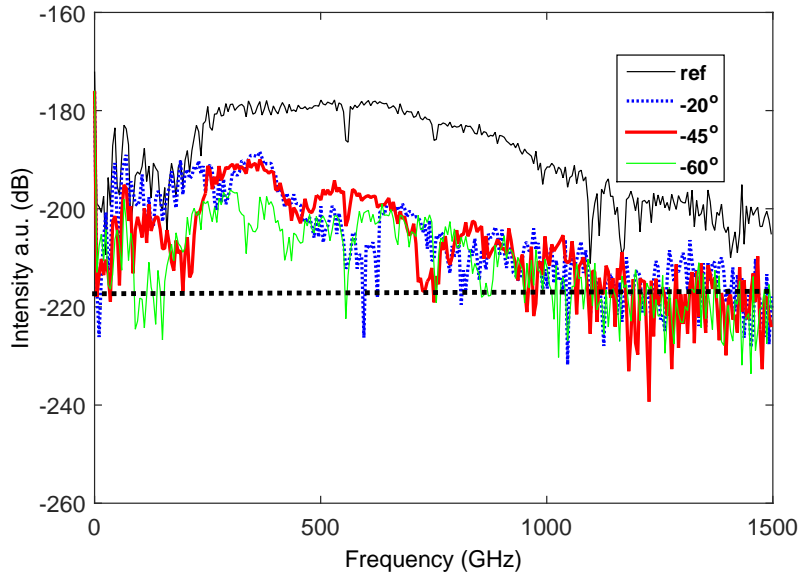


FIGURE 5.21: THz signals transmitted through a random medium consisting of gold coated silica microspheres at negative angles from the incident beam. The dashed lines show the noise floor.

the number density which can be calculated by the volume fraction and mass density of the scatterers. The measured values of the scattering length are shown in Fig. 5.24. The scattering length for the chosen scattering angles are significantly different, the difference being caused by the scattering anisotropy. For on-axis THz transmission,  $l_s$  varies from  $\sim 10$  to  $\sim 1$  mm.  $l_s$  for large angle off-axis ( $>20^\circ$ ) does not vary significantly from its average, i.e. 1-2 mm. The large difference in measured intensity with frequency between  $-20^\circ$  and  $20^\circ$  directions off-axis can be due to the non-uniformity of the sample, resulting from the blending process. The characteristic length of the depolarisation varies between 28-2.8 mm at 0.2-1 THz, indicating that the characteristic length is generally comparable to the scattering length and hence more than one scattering event is required to randomise the polarisation.

Fig. 5.25 shows that the depolarisation ratio increases with the angle off-axis because the average number of the scattering events is increased with these angles, and the mean transport path is significantly greater than the scattering length. Therefore, it is possible to distinguish ballistic (i.e. non scattered) and diffusive photons (scattered) from depolarisation ratio. The depolarisation ratio also varies dramatically within the frequency THz pulses, by a factor of 10. We also compared the numerical simulation with the experimental data. For numerical purpose thousands polarised

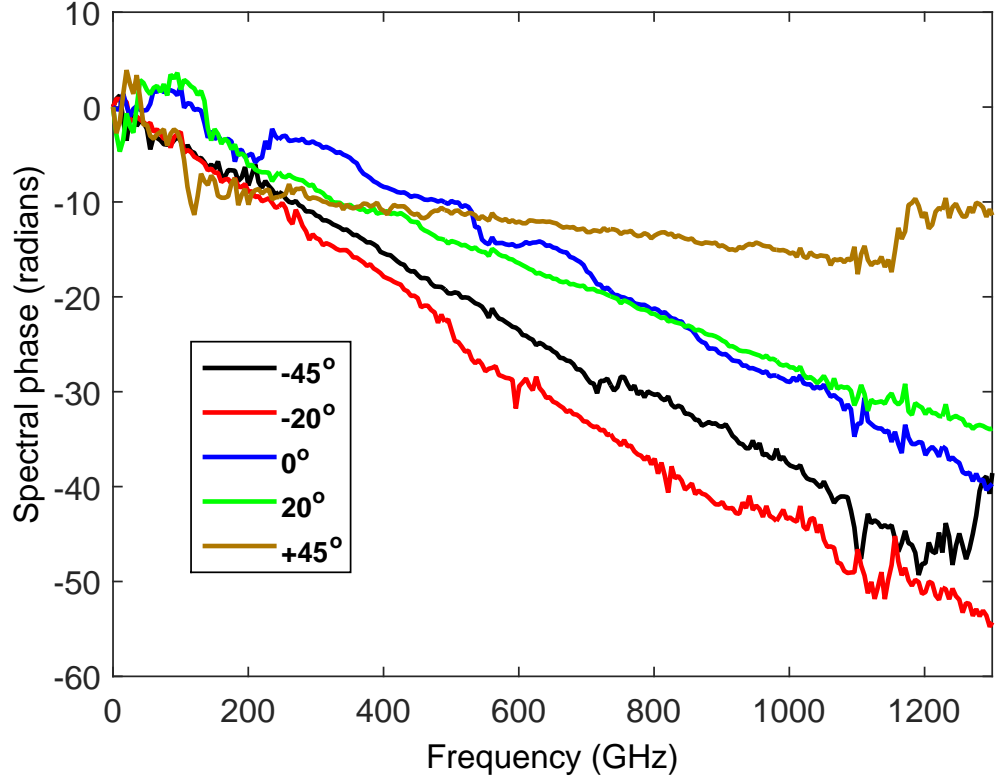


FIGURE 5.22: Phases of the Fourier transforms of the THz transmission at different angles.

photons were launched into the sample and photons transmitted from different boundaries were recorded with their polarisation states. We averaged the depolarisation ratio of the photons at emerging angles. Numerical results are in a good agreement with experimental data. Different values are corresponding to the randomness from the scattering and statistic operation of the program. Figs 5.26 and 5.27 show the spatial distribution of the THz radiation for linearly polarised light at 300 GHz and 500 GHz. The results show a strong scattering of the incident beam over  $-90^\circ$  to  $120^\circ$  for the parallel polarisation; the sample scattered the radiation uniformly with 10-20 dB attenuation. Photons being partially or completely depolarised were detected by the receiver antenna. Fig. 5.27 shows an increased electric field amplitude with the angle off-axis from the incident beam. This is consistent with the fact that the medium scatters more light away from the straight direction because of a lower scattering length

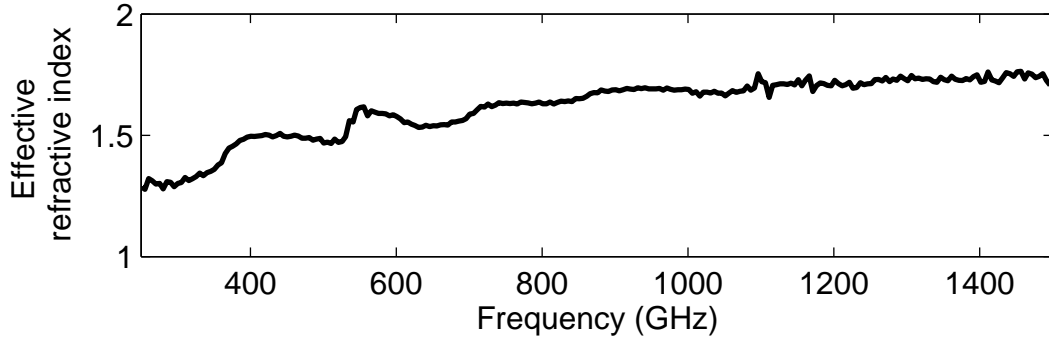


FIGURE 5.23: The effective refractive index of the composite material at 0 degrees.

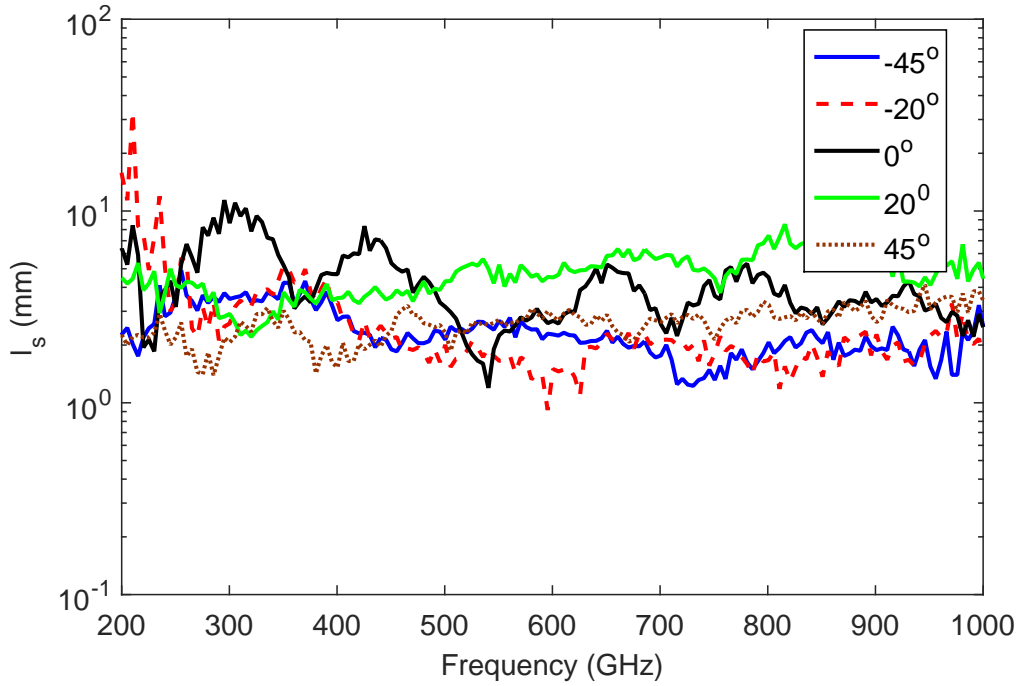


FIGURE 5.24: Scattering length as a function of frequency and angle of arrival.

relative to mean free path, its polarisation being rotated.

## 5.4 Summary

This chapter describes experimental results for the THz scattering in a composite material made by metal particles, namely gold-coated silica-polyethylene. The THz scattering of the proposed materials depends strongly on multiple scattering. The angular



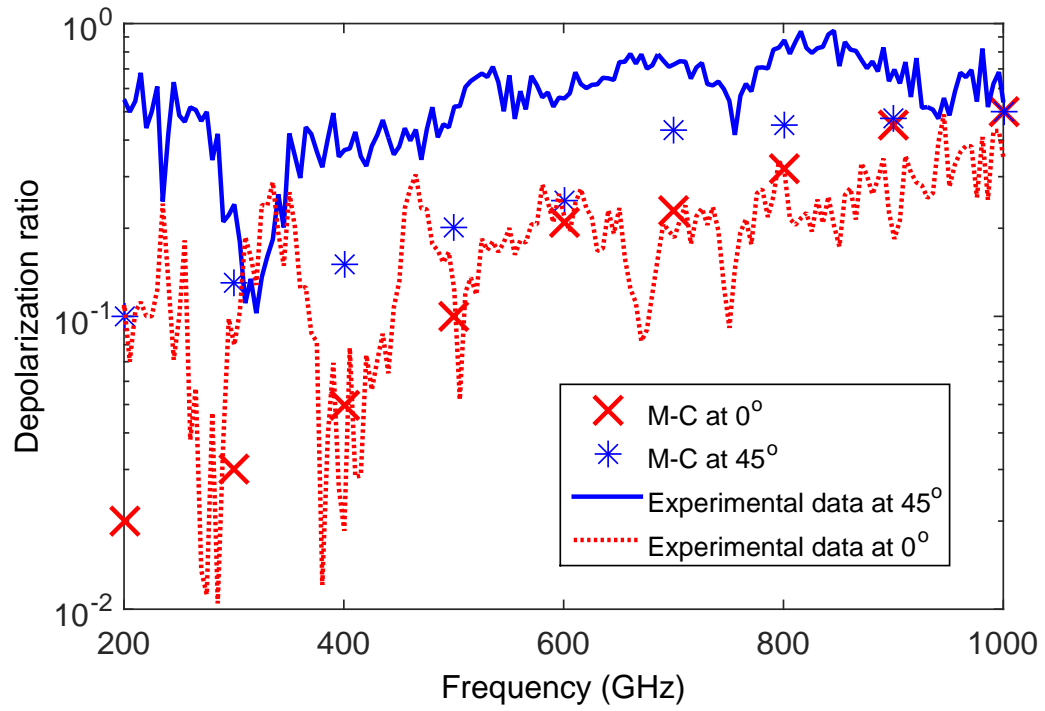
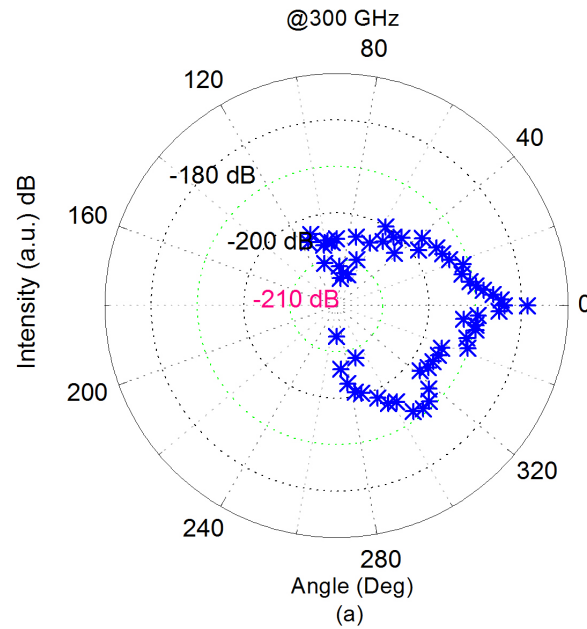


FIGURE 5.25: The depolarisation ratio for linearly polarised light as a function of frequency for different angles,  $0^\circ$  and  $45^\circ$ .



and frequency dependence of the THz scattering were measured to determine multiple scattering effects on the characteristic length of the depolarisation, depolarisation ratio, effective refractive index of the material, and scattering length at off-axis THz

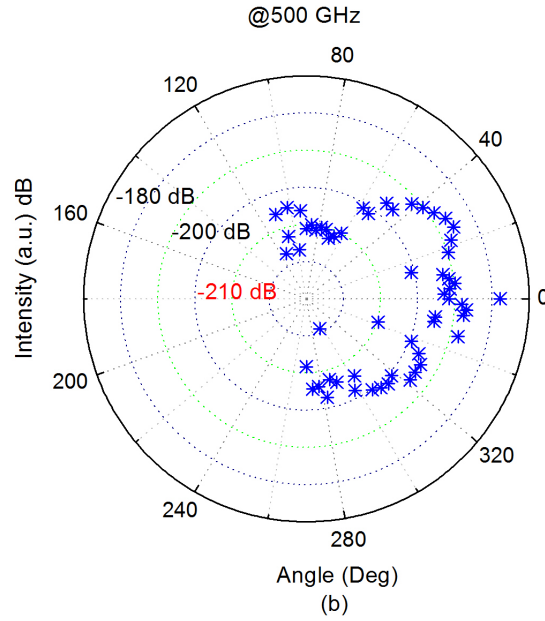
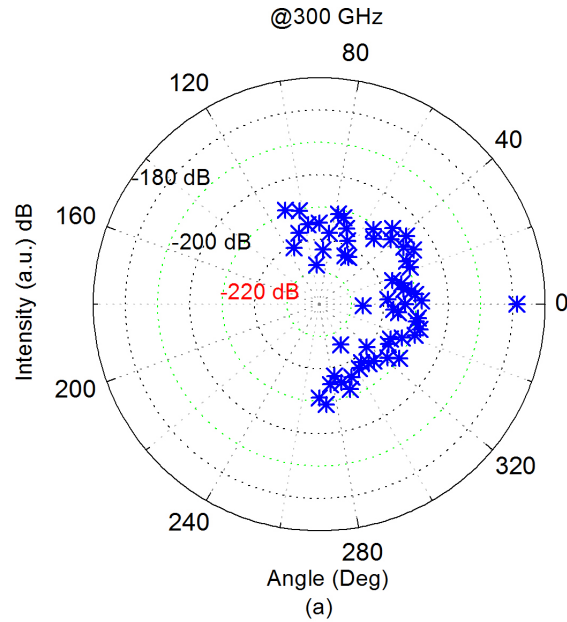


FIGURE 5.26: The THz scattering radiation of (a) 300 and (b) 500 GHz beams by the composite material. -210 dB shows the noise floor.



transmission. The numerical model described in Chapter 4 was also further extended to study the polarisation state of THz pulses propagating through a random medium and determine the degree of polarisation.

The results show that the depolarisation increases with both angle off-axis and frequency, and the proportion of the intensity received by antennas is relatively low

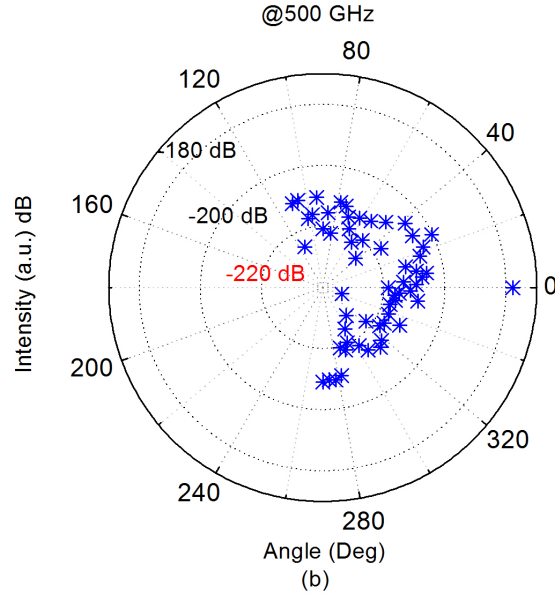


FIGURE 5.27: The THz radiation received in the direction orthogonal to the incident polarised light at (a) 300 and (b) 500 GHz. -220 dB shows the noise floor.

at large scattering angles. However, the received intensity can be compensated using strong enough sources and/or detectors. Consequently, such materials may be useful to increase the availability of a polarised source to the several receivers, e.g. applicable in THz or coherent optical wireless communication systems.

It was also shown that the polarisation state depends on the reflection and refraction at boundaries of finite samples. For example, scattering medium caused the degree of circular polarisation of a 500 GHz wave to decrease from 0.95 to 0.48 at orthogonal boundaries. In contrast, the degree of polarisation of the linearly polarised light transmitted from various directions remained roughly constant. Tailoring of the spatial and spectral distribution of light in the proposed microstructure is possible by varying the size of the scatterers, the length and width of the microstructured materials.

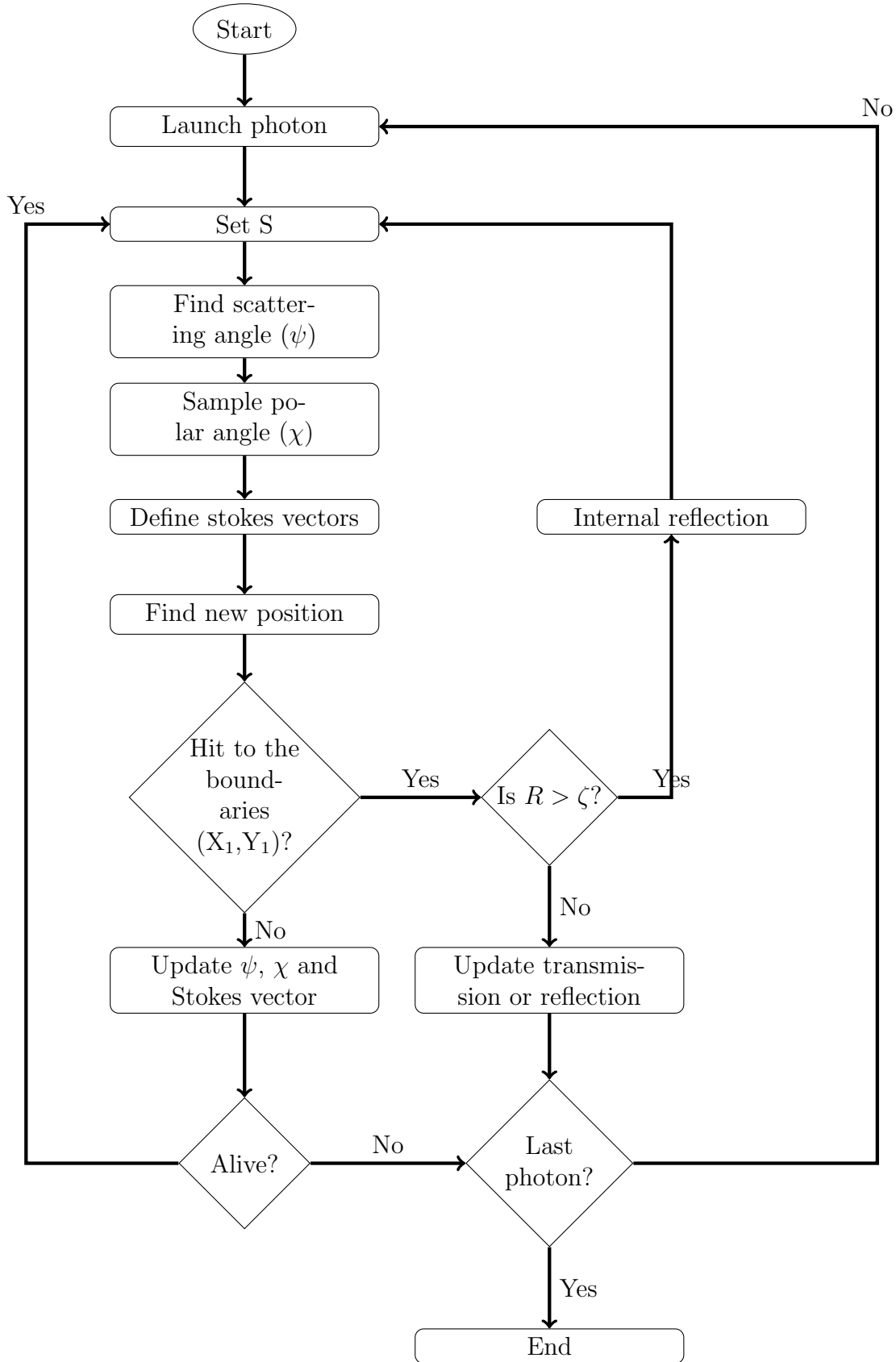


FIGURE 5.28: Flow chart of developed algorithm of the Monte-Carlo program.

# 6

## Conclusion and Future Work

### 6.1 Summary of Results

The focus of this thesis is the optical properties of composite polymer materials, in particular how to deal with or utilise, scattering in such materials. The optical properties of polymer composite materials were modelled using a variety theoretical and numerical techniques. It was predicted that an index change of up to 3% is achievable without excessive loss in the nanocomposites studied, which is relatively large compared to the index change typically achievable in bulk materials, e.g. by UV exposure, stress, etc.

A challenge for polymer optical devices for telecommunication applications in the NIR is loss in the organic host. Here, a novel technique based on polymer nanocomposites was proposed, in which doped nanoparticles (produced top-down) are dispersed into the polymer host, isolating most of the rare-earth ions from the organic host. The question of whether sufficient gain could be achieved to overcome the scattering and absorption losses in such a material was answered through detailed numerical modelling and optimisation. It was shown that an optical gain of 10 dB is feasible at 1.55  $\mu\text{m}$  in a poly(methyl methacrylate) host containing 10% by volume of Er/Yb highly doped phosphate glass nanoparticles 100 nm in diameter when pumped at 980 nm with

intensity  $1 \text{ mW}/\mu\text{m}^2$ .

In many applications scattering is a problem, however a second focus of this research has been to investigate how scattering may be useful, e.g. in randomising the direction and the polarisation of incident EM radiation. A numerical model based on a Monte-Carlo algorithm was developed to properly account for the effect of both loss and boundaries. In microstructured materials, the model was used to study the spatial and spectral distribution of EM waves after propagation through strongly scattering media with boundaries. For example, a thick multiply scattering sample ( $\sim 3 \text{ mm}$ ) comprising of low-index scatterers redirected the radiation into an off-axis direction relative to the incident beam. The thin sample absorption was dominated in the transmission loss due to the path length for the ballistic photons equalling the sample thickness. The model was further extended to also study the effects of multiple scattering on the polarisation of EM waves exiting highly scattering composite materials.

To confirm the model, measurements of the angle-, frequency-, and polarisation-dependent THz scattering were performed using a THz-TDS with goniometer, giving both the spatial and spectral distribution of the THz pulses. It was shown that 2-D polymer microstructures distributed a broadband source at a wide range of angles, from  $-90$  to  $120$  degrees, while the air-polymer composite material was directive. THz scattering at an angle off-axis from the incident beam is important to reconstruct the absorption loss in the interior of materials, particularly applicable in material identification and/or sensing. The results showed that the mean transport path is significantly greater than the scattering length, hence the characteristic length decreases; the depolarisation ratio increases with the angle off-axis due to an increase in scattering events.

Given the good correspondence between the developed model and the experimental results, the model was used to investigate the dependence of circularly polarised light on boundaries and multiple scattering. As an example, it was shown that the degree of a circularly polarised wave emerging from the orthogonal boundaries decreases from  $0.95$  to  $0.48$  as the wave experiences more angle rotation compared with a linearly polarised wave. Such materials may be useful as a depolariser, e.g. to increase the availability of a polarised source to several receivers.

## 6.2 Future Work

Future directions include the application of different polymer nanocomposite materials in polymer microstructured optical fibre to meet requirements of specific applications in

optical components. This may include sensors and optical switches based on polymers. The choice of inclusions has a significant influence on the potential of polymer-based optical devices to improve thermal properties, e.g. PMMA has negative thermo-optic and positive thermo-expansion coefficients, hence the polymer microstructures' behaviour may be designed to be independent of temperature and/or can be tuned thermally at wavelengths of interest.

The feasibility of writing planar waveguides on polymer composite materials with  $\text{P}_2\text{O}_5:\text{Er}^{3+}/\text{Yb}^{3+}$  co-doped nanoparticles, and their characterisation, including measurements of loss and gain are of interest. It could also be interesting to make use of highly scattering materials to create useful optical components. An example is a random laser, where laser action can be generated by the diffusion of light from a strongly scattering medium with powders and porous doped glass inclusions. Highly scattering media can provide many useful practical applications in wireless THz communication systems. They can provide a coherent source to different receivers for short-range THz communication. Another topic could be the study of the polarisation of a coherent depolarised source propagating through a highly scattering medium. Recently it has been shown that a strongly scattering medium can also increase the polarisation of incident depolarised light [214].







# Materials

## A.1 Properties of Materials

### A.1.0.1 PMMA

Organic materials (such as PMMA) have been investigated as an alternative to inorganic materials (such as glasses) for fabricating optical devices such as optical fibers and waveguides. This has been due to their straightforward and cost effective processing. Most organic materials consist of a chromophoric group (such as C-C), C-H, and C-O bonds which cause absorption at short UV and at NIR wavelengths, respectively. Fig. [A.1](#) shows the chemical structure of PMMA.

### A.1.0.2 SiO<sub>2</sub> Nanoparticles

Silicon dioxide nanoparticles are the basis for a great deal of photonic research due to their stability, and ability to be functionalised with a range of monomers and polymers. The silica has an extremely large surface area which can promote strong chemical reactions and physical contact between the inclusions and the polymer matrix. The structure of silica nanoparticles exhibits three different networks including free silanols, hydrogen-bonded and geminal silanols as shown in Fig. [A.2](#). The latter groups on the

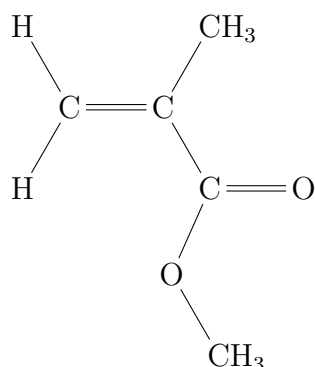


FIGURE A.1: Chemical structure of Poly(methylmethacrylate).

silica surface lead to hydrophilic nature of the particles and thus cause formation of aggregates. Surface modification can be achieved by either chemical modification or physical methods such as a high-energy ball-milling process.

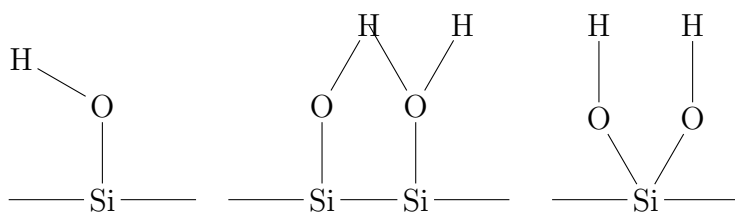


FIGURE A.2: Schematic illustration of three types of Silanol groups on the surface of silica nanoparticles.

### A.1.0.3 3-(Trimethoxysilyl)Propyl Methacrylate (MPTS)

Fig. A.3 shows the chemical structure of MPTS as a modifier agents. The structure can be represented as  $\text{RSiX}_3$  in which R is a hydrolyzable group such as methacryloxy and X is an organofunctional group such as methoxy groups. The hydroxyl groups on the silica surface reacts with organo group and the alkyl chain reacts with the polymer and thus hydrophobic silica can be obtained.

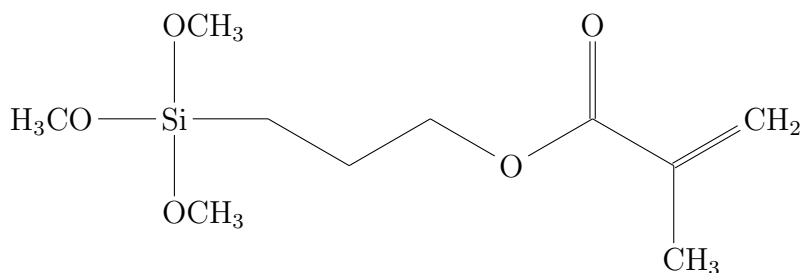


FIGURE A.3: Molecular structure of 3-(Trimethoxysilyl)Propyl Methacrylate (MPTS).

#### A.1.0.4 2,2-Dimethoxy-2-phenylacetophenone (BDK)

Various kinds of polymers can be synthesised by light-induced chemical processes. Radical polymerization can be photoinitiated, provided that suitable photoinitiator is employed. Photoinitiators such as BDK are compounds that are thermally stable with relatively high absorption coefficients in the UV and/or visible regions and thus exhibit a large photo-induced change in optical properties of polymers. Under UV exposure, BDK molecules are decomposed into two radicals, so the decomposition molecules can attach to methacrylate groups and/or to the decomposed radicals. The chemical structure and bond cleavage of BDK are shown in Fig. A.4.

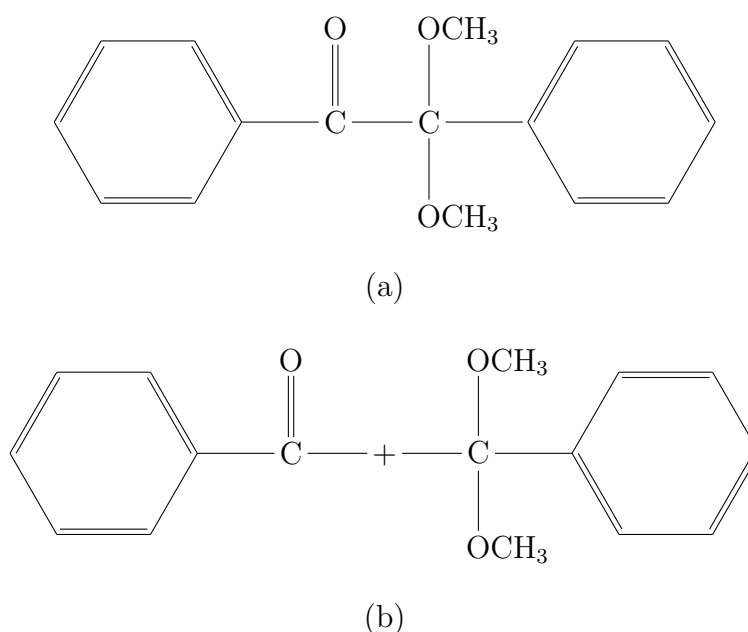


FIGURE A.4: Molecular structures of BDK: (a) before, and (b) after UV illumination.

#### A.1.0.5 Azobisisobutyronitrile (AIBN)

The polymerization of MMA can be initiated by thermal initiators such as AIBN. Thermally initiated polymerization of AIBN are usually performed for emulsion, solution and bulk polymerizations. The chemical structure of AIBN is shown in Fig. A.5.

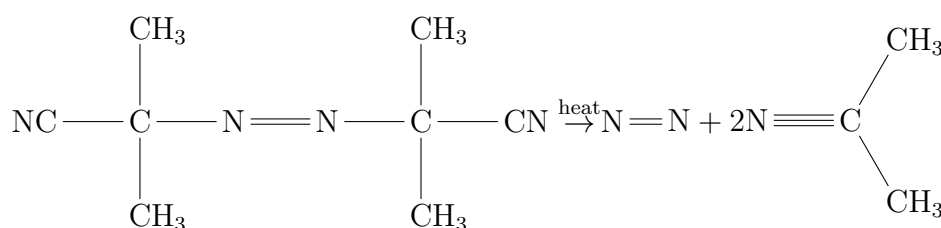


FIGURE A.5: Decomposition formula of AIBN upon heating.

#### A.1.0.6 9-Vinylanthracene (9-VA)

There are substances, such as anthracene groups, that are transformed from one form into another form upon irradiation with particular wavelength of light and that return to the initial state either by the absorption of light or thermally. This phenomenon is termed photochromism. In order to enhance the photosensitivity of polymers, we use anthracene derivatives as photosensitisers that absorb light strongly at UV/Vis wavelength. During the photopolymerisation of monomers, the sensitiser is co-polymerised with the main monomer. Fig. A.6 shows the molecular structure of 9-VA. Upon light exposure, anthracene photodimerisation takes place, forming the carbon-carbon bonds which can be co-polymerised with methyl methacrylate. Photodimerisation results in a variety of products in which molecules can align head-to-tail or head-to-head, depending on the proximity of the alkenes. Moreover, 9-VA is also thermally active which may promote the thermal stability of polymers.

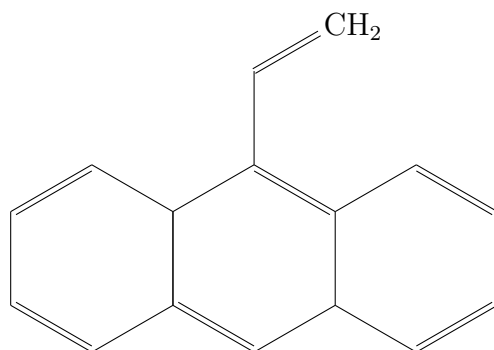


FIGURE A.6: Molecular structures of 9-Vinylanthracene (9-VA).

### A.1.1 Surface Modification of Silica Nanoparticles

The surfaces of the silica nanoparticles are typically terminated with silanol groups (Si-OH), leading to hydrophilic particles and hence formation of aggregates in a disperse medium. A good dispersion can be achieved by surface modification of the nanoparticles using a chemical reaction and/or a physical process such as high energy ball-milling. The surface of the silica nanoparticles, with a diameter of 7 nm and the phosphate glass particles was modified with MPTS, as the silanol coupling agents of MPTS result in increasing the hydrophobicity of the silica nanoparticles and thus a strong covalent bonding between the particles and the monomer. As shown in Fig. A.7, MPTS reacts with the hydroxide groups on the surface of silica nanoparticles and then provides methacrylate terminal groups for polymer grafting. First, 300 mg silica nanoparticles were dispersed in 10 mL ethanol into a round-bottom flask by ultrasonic bath for 30 min, then 240  $\mu$ L MPTS was added drop-wise to the solution and sonicated for 2 hours [215]. The resulting suspension was centrifuged at 4100 g-force for 80 min and the precipitates were redispersed into 10 mL ethanol. Purification with ethanol was repeated three times. Finally, the product was dried at 70 °C for 24 hours in an oven.

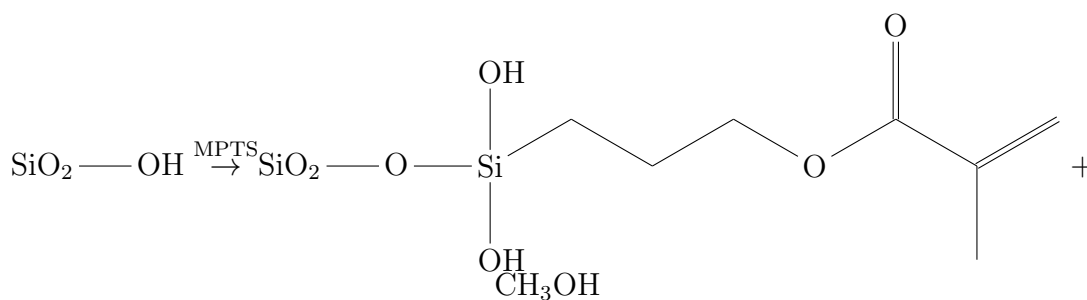


FIGURE A.7: Surface modification of silica with MPTS.

Fig. A.8 shows the FTIR of unmodified silica nanoparticles and functionalised silica nanoparticles. The carbonyl vibration band at 1700  $\text{cm}^{-1}$  clearly suggests the presence of methacrylate groups on the silica surface. Moreover, it indicates that the O-H groups were removed from the surface of bare silica, as the intensity of their absorption in the range 3200-3700  $\text{cm}^{-1}$  have been removed by functional group.

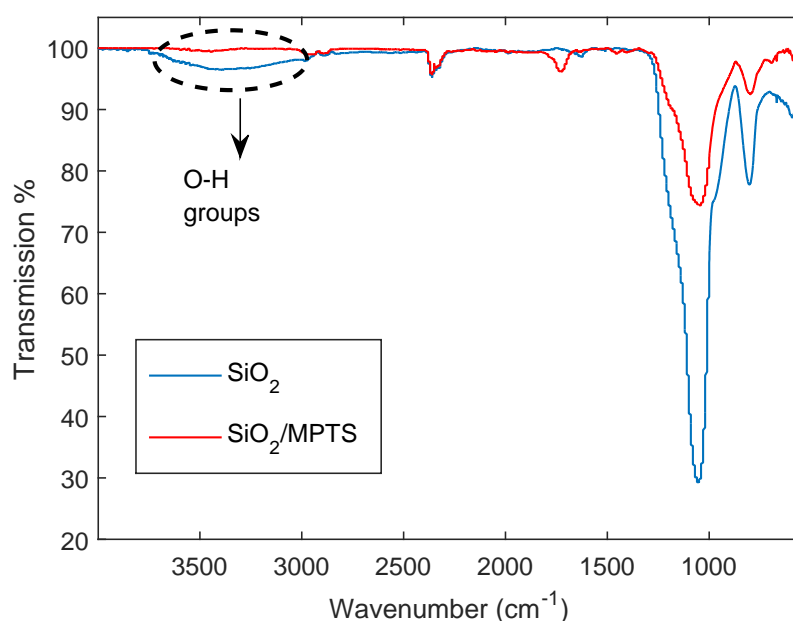


FIGURE A.8: FTIR of unmodified and functionalised silica nanoparticles.

## A.1.2 In Situ Polymerisation

### A.1.2.1 Removal of Inhibitor

MMA is highly reactive and can form polymer during storage and/or transportation. Therefore, the monomer is maintained in an inhibited condition. To initiate polymerisation, the monomers should be purified either by the distillation process or by running the monomers through the small column containing Alumina. The diagram of the distillation of MMA is shown in Fig. A.9. The vacuum flask was placed into an preheated hot water at  $55^\circ\text{C}$ . Then, the vacuum was increased until the monomer began to boil gently. Afterwards, the vapor passed through the condenser. The heat level and vacuum were adjusted to the point where one drop per second was falling into the collection flask in order to obtain a highly purified monomer. The distillation process was continued until the inhibitor (yellowish substance) was left in the boiling flask, shown in Fig. A.10.

### A.1.2.2 Thermal Polymerisation

The modified silica nanoparticles were dispersed in MMA using a high energy ball milling for 20 h. The ratios of silica to MMA were 2, 5, and 10 percent. The AIBN was

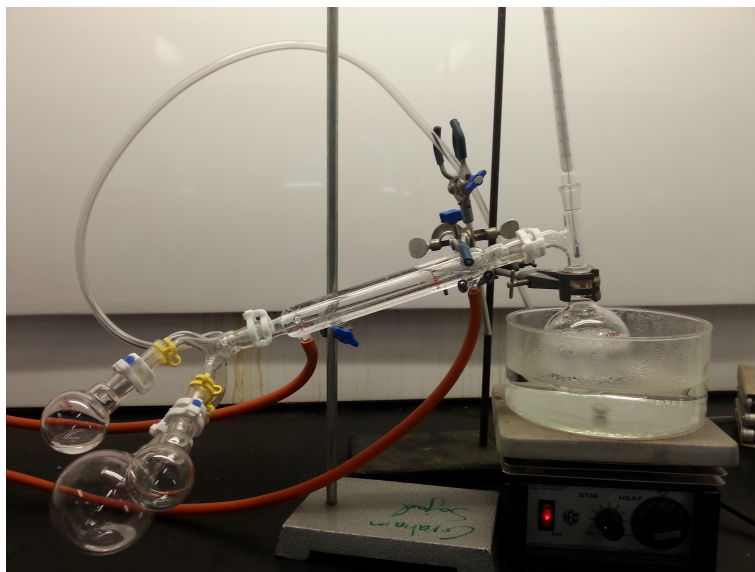


FIGURE A.9: Purifying methyl methacrylate using a vacuum distillation.

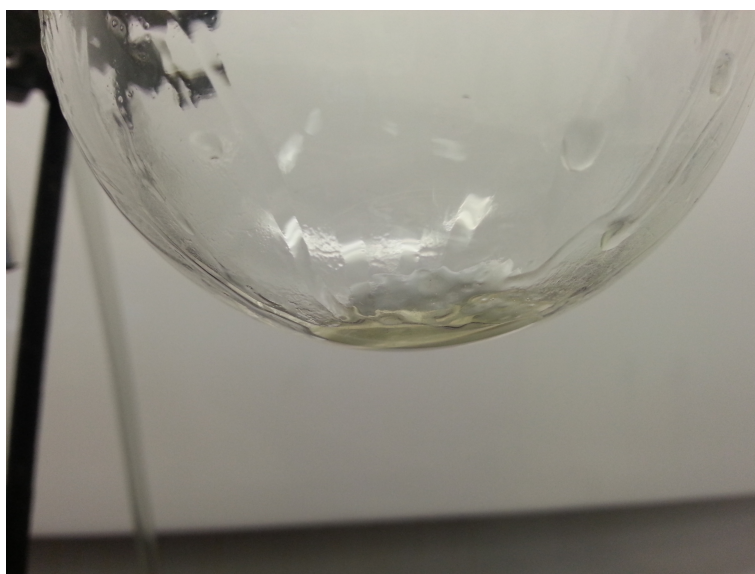


FIGURE A.10: Inhibitor remaining in the bottom of the flask.

added to MMA in a molar ratio of 1:100 and the reaction flasks then fitted with rubber septum and stirred for 2 hours to obtain homogeneous solutions. As the presence of molecular oxygen could act as an inhibitor, the solutions were degassed using nitrogen in which the needle connected by tubing to the nitrogen line was inserted to the solution.

Nitrogen was then bubbled through the solution for 20 min. Another needle was inserted through the septum to purge oxygen. The flask was placed in a constant temperature bath maintained at 70°C. The MMA monomer was co-polymerised with MPTS on the surface of silica nanoparticles in the presence of the initiator. The polymer were precipitated out as a white fluffy solid by dropping into methanol. They then filtered with suction, washed with methanol and dried at 40 °C.

### A.1.2.3 Photo-Polymerisation

The main advantage of photo polymerisation over thermal polymerisation is the control of initiation in terms of photo-induced refractive index changes. Although a major problem with photo polymerisation is the penetration of light through a thickness of material, it is well suited for thin-layer applications. The appropriate amount of modified silica nanoparticles was added to 100 g MMA and ultrasonically dispersed. Then, the required amount of photoinitiator (BDK:MMA:0.1:1) were dissolved in the solution. The polymerisation was conducted for the different exposure times to the UV source (i.e. 1000 W high intensity mercury lamp). We tried to increase the photosensitivity of PMMA/SiO<sub>2</sub> by doping 9-Vinylanthracene (9-VA) as the photosensitive species. A key advantage of anthrance components is that they are optically active in which enables 9-VA to become photodimer under UV/vis radiation. 9-VA also has C-C groups which are thermally active and thus 9-VA can be copolymerised with MMA and may enhance thermal stability of PMMA/Silica nanocomposite. The images of polymer nanocomposites after exposing to UV lamp are shown in Fig.A.11. During the polymerisation process, the volume deforms due to material shrinkage and the refractive index changes.

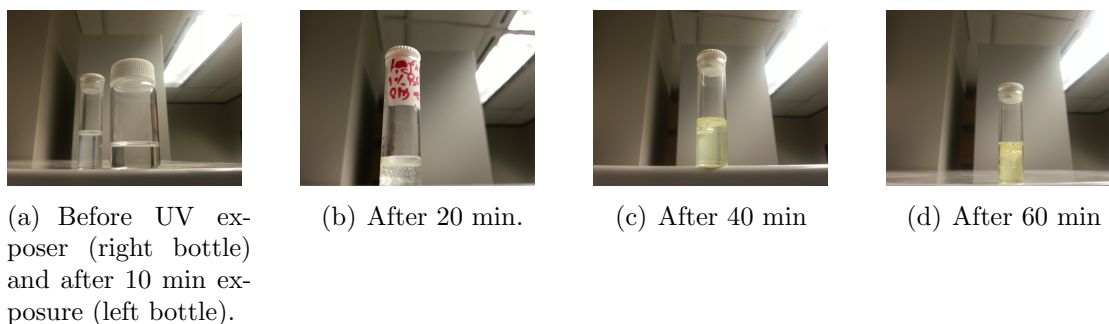


FIGURE A.11: Changes in the refractive index of polymer doped with BDK under UV irradiation at various exposure times.

Fig. A.12 shows the FTIR of a PMMA-silica nanocomposite with 5% silica. The



vibration absorption of the Si-O-Si groups at  $1140\text{ cm}^{-1}$ , CH, and CO stretching vibration indicates that PMMA has been grafted onto the surface of  $\text{SiO}_2$  successfully.

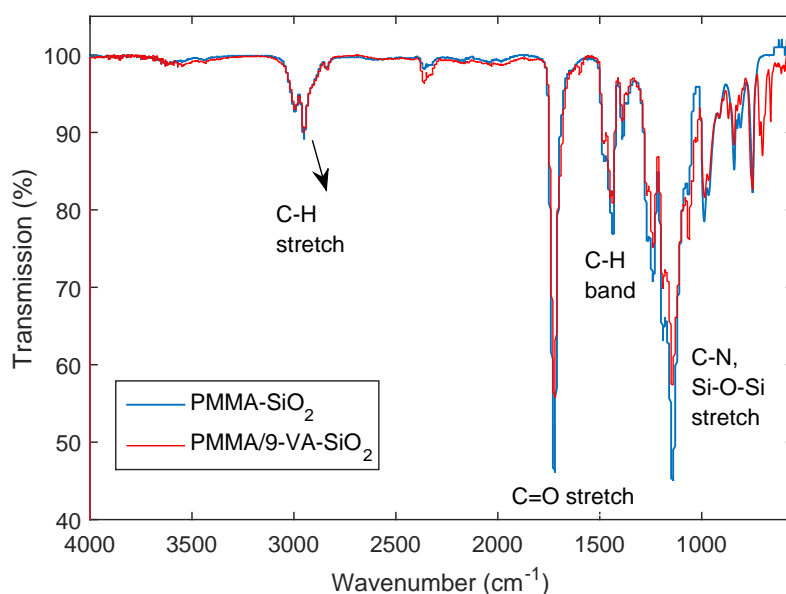


FIGURE A.12: FTIR of PMMA-silica nanocomposite with 5% silica.

### A.1.3 Solution Blending

Solution mixing is the most common method for preparing polymer nanocomposites in which the components (host and nanoparticles) are dissolved and/or dispersed in a suitable solvent. Since the dispersion depends on the solvent and its recovery, the main difficulty is to properly disperse the nanoparticles into the polymer. Different polymer/silica nanocomposites were prepared as follows. One gram of PMMA pellets was dissolved in 3 mL of toluene under stirring at  $40^\circ\text{C}$ . Depending on the required mass fraction of silica nanoparticles in the polymer, the particles were suspended in toluene by sonication for 1 hour. The particles suspension was drop wise added to the polymer solution and the mixture was sonicated for another 2 hours. The mixture was placed in a vacuum oven for 24 h to evaporate the solvent.

### A.1.4 Polymer Nanocomposite Thin Films

Thin films of polymer nanocomposites were prepared by spin-coating of the solution onto quartz slides. The polymer nanocomposites with different solution concentrations

were spun at speeds ranging from 500 to 5000 rpm to form the most uniform ultra-thin film. Acceleration times were less than 5 s and spin times were 30 s. The roughness and thickness of the thin layers were measured by Tencor.

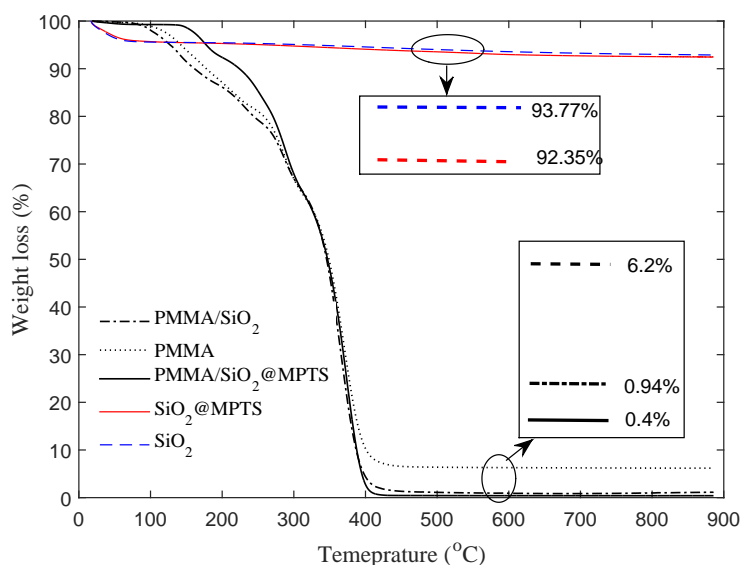


FIGURE A.13: Thermo gravimetric analysis (TGA) of SiO<sub>2</sub>, SiO<sub>2</sub>-MPTS, PMMA, PMMA/SiO<sub>2</sub>, and PMMA/SiO<sub>2</sub>-MPTS; TGA was performed in nitrogen at a heating rate of 10°C/min.

To validate the hypothesis that a chemical reaction occurs we performed thermo-gravimetric analysis (TGA) with a heating ramp of 10 °C/min up to 900 °C under nitrogen, as shown in Fig. A.13. The weight loss observed for SiO<sub>2</sub>-MPTS is attributed to the MPTS attached to the surface of the particles. The initial weight loss at around 100 °C correlates with the evaporation of solvent and/or water in the sample. As for PMMA/SiO<sub>2</sub>, a rapid weight loss at around 270 °C corresponds to the degradation of PMMA grafted onto the surface of the silica nanoparticles. By contrast, PMMA/SiO<sub>2</sub>-MPTS shows a higher degradation temperature, so the thermal stability of the nanocomposite is improved.

Table A.1 shows the thickness, the average surface roughness (Ra) and the root-mean-square roughness (Rq) of the thin films. Embedding untreated silica nanoparticles in the polymer matrix significantly changed the morphology of the thin films, implying the formation of aggregates of nanoparticles in the polymer matrix. However, pretreatment of the silica with MPTS resulted in lower cluster formation, and consequently the surface roughness decreased substantially compared to bare silica in

TABLE A.1: Tencor Data of the Prepared PMMA, PMMA/SiO<sub>2</sub>, and PMMA/SiO<sub>2</sub>-MPTS thin films spin-coated at 2000 rpm for 30 sec.

Sample	Thickness ( $\mu\text{m}$ )	Ra (nm)	Rq (nm)
PMMA	1.75	1.38	1.05
PMMA/SiO <sub>2</sub> - MPTS	1.044	3.2	3.8
PMMA/SiO <sub>2</sub>	1.418	34.3	16.2

PMMA.

The optical loss of PMMA/SiO<sub>2</sub>-MPTS was approximately 25% lower than that of PMMA/SiO<sub>2</sub> at visible wavelengths, as shown in Fig. A.14. The reduction in loss is attributed to the improved dispersion of the SiO<sub>2</sub>-MPTS nanoparticles in the PMMA matrix, resulting in less aggregation and hence lower scattering loss.

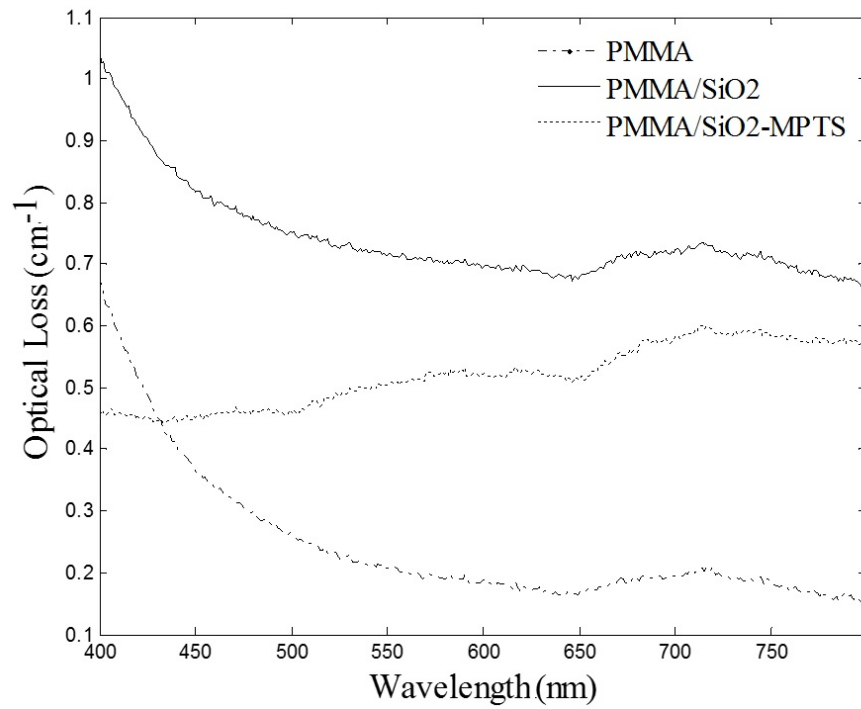


FIGURE A.14: Optical loss spectra of PMMA, PMMA/SiO<sub>2</sub>, and PMMA/SiO<sub>2</sub>-MPTS.



# B

## Mie Scattering for Infinite Cylinder

The Mie equation solves Maxwell's equations with boundary conditions for the scattering of a infinite cylinder is as follow [194]:

$$\sigma_s = \frac{2\pi}{k^2} \sum_{n=1}^{\infty} (2n+1) (|a_n|^2 + |b_n|^2) \quad (\text{B.1})$$

The coefficient of scattering series are:

$$a_n = \frac{C_n D_n - E_n F_n}{G_n D_n + i F_n^2} \quad (\text{B.2})$$

$$b_n = \frac{G_n D_n + i F_n C_n}{G_n D_n + i F_n^2} \quad (\text{B.3})$$

$$C_n = n \cos \theta \eta J_n(\eta) J_n(\beta) \left( \frac{\beta^2}{\eta^2} - 1 \right) \quad (\text{B.4})$$

$$D_n = \beta \left[ m^2 \beta J'_n(\eta) H_n^{(1)}(\beta) - \eta J_n(\eta) H_n^{(1)'}(\beta) \right] \quad (\text{B.5})$$

$$E_n = \beta \left[ m^2 \beta J'_n(\eta) J_n(\beta) - \eta J_n(\eta) J'_n(\beta) \right] \quad (\text{B.6})$$

$$F_n = n \cos\theta \eta J_n(\eta) H_n^{(1)}(\beta) \left( \frac{\beta^2}{\eta^2} - 1 \right) \quad (\text{B.7})$$

$$G_n = i\beta \left[ \eta J_n(\eta) H_n^{(1)'}(\beta) - \eta J_n'(\eta) H_n^{(1)}(\beta) \right] \quad (\text{B.8})$$

$$\beta = x \sin(\theta) \quad (\text{B.9})$$

$$\eta = x \sqrt{m^2 - \cos^2(\theta)} \quad (\text{B.10})$$

where  $J_n$  and  $H_n^{(1)}$  are Bessel functions of the first and the third kind of  $n$  order, respectively.  $m$  is the relative refractive index,  $x$  the size parameter,  $a$  the radius of the infinite cylinder, and  $\theta$  the angle formed between the incident beam and the axis of cylinder [194].

# List of Acronyms/Abbreviations

AIBN	Azo-bisisobutyronitrile
Ag	Silver
Au	Gold
BDK	2,2-Dimethoxy-2-phenylacetophenone
C	Circularly Polarised Light
CdS	Cadmium Sulfide
CdSe	Cadmium Selenide
Cu	Cooper
D	Diffusion Length
DOP	Degree of Polarisation
dB	Decibels
EO	Electro-Optic
Er	Erbium
Fe	Iron
FFT	Fast Fourier Transform
f	Volume Fraction
G	Green's Fraction
Ge	Germanium
g	Anisotropy Factor
g	Gain Function
k	Wavenumber
I	Intensity
$I_p$	Pump Intensity
$I_s$	Signal Intensity
L	Linearly Polarised Light
l	Optical Length Path
M	Muller Matrix
MMA	Methyl methacrylate
MPTS	3-(Trimethoxysilyl)Propyl Methacrylate
MS	Multiple Scattering
m	Refractive Index of Particle to Host
N	Concentration
NDT	Nondestructive Testing
Nd	Neodymium

NLO	Nonlinear Optical
NP	Nanoparticles
Od	Optical Depth
SNR	Signal to Noise Ratio
PbS	Lead Sulfide
Pc	Polycarbonate
PDF	Probability Density Function
PMMA	Poly(methyl methacrylate)
$P_p$	Pump Power
$P_s$	Signal Power
Ps	Polystyrene
Pt	Platinum
QD	Quantum Dot
R	Reflection
RI	Refractive Index
S	Stokes Vector
SiO <sub>2</sub>	Silica
T	Transmittance
TDS	Time Domain Spectroscopy
THz	Terahertz
TiO <sub>2</sub>	Titanium Dioxide
W	Photon Weight
x	Size Parameter
Yb	Ytterbium
ZnO	Zinc Oxide



# Symbols

$a$	Particle Radius
$B$	Bose-Einstein Occupation Number
$\alpha$	Absorption Coefficient
$C_{cr}$	Cross Relaxation
$C_{up}$	Upconversion Coefficient
$\chi$	Azimuth Angle
$dn/dT$	Thermo-Optic Coefficient
$\gamma$	Coupling Constant
$H_n^{(1)}(x)$	Hankel Function of the First Kind of Order n
$J_n(x)$	Bessel Function of the First Kind of Order n
$K$	Boltzman Constant
$k_{ext}$	Extinction Coefficient
$l_s$	Scattering Length
$l^*$	Transport Mean Free Path
$\lambda$	Wavelength
$n_h$	Refractive Index of Host
$n_i$	Population Levels
$n_p$	Refractive Index of Nanoparticle
$\Omega$	Solid Angle
$P_n^1 \cos\theta$	Legendre Polynomial
$\psi$	Polar Angle
$\psi_n$	Spherical Riccati-Bessel Function
$S_{1,2}$	Scattering Amplitude Functions
$\sigma_s$	Scattering Cross-Section
$\sigma_a$	Absorption Cross-Section
$\sigma_{ext}$	Total Attenuation
$T_d$	Diffuse Transmittance
$\tau$	Life Time
$\theta$	Scattering Angle
$W_{ij}$	Transition Rate
$\zeta$	Characteristic Length
$\zeta$	Spherical Riccati-Bessel Function
$9 - VA$	9-Vinylanthracene



## References

- [1] H. Ma, A. K.-Y. Jen, and L. R. Dalton. *Polymer-based optical waveguides: materials, processing, and devices*. Advanced Materials **14**(19), 1339 (2002). [1](#)
- [2] L. Eldada and L. W. Shacklette. *Advances in polymer integrated optics*. Selected Topics in Quantum Electronics, IEEE Journal of **6**(1), 54 (2000). [1](#)
- [3] X. C. Tong. *Advanced materials for integrated optical waveguides* (New York, Springer, 2014). [1](#)
- [4] E. Van Tomme, P. Van Deale, R. G. Baets, and P. E. Lagasse. *Integrated optic devices based on nonlinear optical polymers*. IEEE Journal of Quantum Electronics **27**(3), 778 (1991).
- [5] S. Xiao, F. Wang, X. Wang, Y. Hao, X. Jiang, M. Wang, and J. Yang. *Electro-optic polymer assisted optical switch based on silicon slot structure*. Optics Communications **282**(13), 2506 (2009).
- [6] Z. Xiong, G. Peng, B. Wu, and P. Chu. *Highly tunable Bragg gratings in single-mode polymer optical fibers*. IEEE Photonics Technology Letters **11**(3), 352 (1999). [1](#), [2](#)
- [7] P. M. Ajayan, L. S. Schadler, and P. V. Braun. *Nanocomposite science and technology* (Weinheim, Germany, John Wiley & Sons, 2006). [7](#)
- [8] A. C. Balazs, T. Emrick, and T. P. Russell. *Nanoparticle polymer composites: where two small worlds meet*. Science **314**(5802), 1107 (2006). [6](#)
- [9] C. Sanchez, B. Lebeau, F. Chaput, and J.-P. Boilot. *Optical properties of functional hybrid organic-inorganic nanocomposites*. Functional Hybrid Material pp. 122–168 (2004). [2](#)

- [10] M. J. Digonnet. *Rare-earth-doped fiber lasers and amplifiers, revised and expanded* (New York, CRC press, 2001). [2](#), [9](#), [41](#), [44](#)
- [11] L. Slooff, A. Van Blaaderen, A. Polman, G. Hebbink, S. Klink, F. Van Veggel, D. Reinhoudt, and J. Hofstraat. *Rare-earth doped polymers for planar optical amplifiers*. *Journal of Applied Physics* **91**(7), 3955 (2002). [2](#), [11](#), [40](#)
- [12] T. Kaino and Y. Katayama. *Polymers for optoelectronics*. *Polymer Engineering & Science* **29**(17), 1209 (1989). [2](#)
- [13] B. Robinson, L. Dalton, A. Harper, A. Ren, F. Wang, C. Zhang, G. Todorova, M. Lee, R. Aniszfeld, S. Garner, *et al.* *The molecular and supramolecular engineering of polymeric electro-optic materials*. *Chemical Physics* **245**(1), 35 (1999). [2](#)
- [14] B. Ferguson and X.-C. Zhang. *Materials for terahertz science and technology*. *Nature Materials* **1**(1), 26 (2002). [3](#)
- [15] D. Zimdars, J. S. White, G. Stuk, A. Chernovsky, G. Fichter, and S. Williamson. *Large area terahertz imaging and non-destructive evaluation applications*. *Insight-Non-Destructive Testing and Condition Monitoring* **48**(9), 537 (2006).
- [16] M. Tonouchi. *Cutting-edge terahertz technology*. *Nature Photonics* **1**(2), 97 (2007).
- [17] M. J. Fitch and R. Osiander. *Terahertz waves for communications and sensing*. *Johns Hopkins APL Technical Digest* **25**(4), 348 (2004). [3](#), [91](#)
- [18] A. Doronin, C. Macdonald, and I. Meglinski. *Propagation of coherent polarized light in turbid highly scattering medium*. *Journal of Biomedical Optics* **19**(2), 025005 (2014). [3](#)
- [19] K. Meerholz, B. Volodin, B. Kippelen, N. Peyghambarian, *et al.* *A photorefractive polymer with high optical gain and diffraction efficiency near 100%*. *Nature* **371**, 497 (1994). [4](#)
- [20] K. Hill, Y. Fujii, D. C. Johnson, and B. Kawasaki. *Photosensitivity in optical fiber waveguides: Application to reflection filter fabrication*. *Applied Physics Letters* **32**(10), 647 (1978). [4](#)

- [21] I. Alexeev, K. Cvecek, J. Genser, and M. Schmidt. *Direct waveguide writing with high energy high repetition rate picosecond laser pulses*. Physics Procedia **39**, 621 (2012). [4](#)
- [22] L. W. Carter, J. G. Hendricks, and D. S. Bolley. *Elastomer reinforced with a modified clay* (1950). US Patent 2,531,396. [6](#)
- [23] R. P. Feynman. *There's plenty of room at the bottom*. Engineering and Science **23**(5), 22 (1960). [6](#)
- [24] P. G. Nahin and B. P. Stanley. *Organoclay-polyolefin compositions* (1963). US Patent 3,084,117. [6](#)
- [25] A. Blumstein. *Polymerization of adsorbed monolayers. II. thermal degradation of the inserted polymer*. Journal of Polymer Science Part A: General Papers **3**(7), 2665 (1965). [6](#)
- [26] S. Fujiwara and T. Sakamoto. *Kokai patent application*. Sho **51**(109998), 1976 (1976). [6](#)
- [27] A. Ekimov, A. L. Efros, and A. Onushchenko. *Quantum size effect in semiconductor microcrystals*. Solid State Communications **56**(11), 921 (1985). [6](#)
- [28] W. Caseri. *Inorganic nanoparticles as optically effective additives for polymers*. Chemical Engineering Communications **196**(5), 549 (2008). [6](#)
- [29] M. Gao, Y. Yang, B. Yang, F. Bian, and J. Shen. *Synthesis of PbS nanoparticles in polymer matrices*. Journal of the Chemical Society, Chemical Communications (24), 2779 (1994). [6](#)
- [30] R. Hong, J. Qian, and J. Cao. *Synthesis and characterization of PMMA grafted ZnO nanoparticles*. Powder Technology **163**(3), 160 (2006).
- [31] S. Porel, N. Venkatram, D. Narayana Rao, and T. Radhakrishnan. *In situ synthesis of metal nanoparticles in polymer matrix and their optical limiting applications*. Journal of Nanoscience and Nanotechnology **7**(6), 1887 (2007).
- [32] C. Sciancalepore, T. Cassano, M. Curri, D. Mecerreyes, A. Valentini, A. Agostiano, R. Tommasi, and M. Striccoli. *TiO<sub>2</sub> nanorods/PMMA copolymer-based nanocomposites: highly homogeneous linear and nonlinear optical material*. Nanotechnology **19**(20), 205705 (2008).

- [33] J. Zhang, N. Liu, M. Wang, X. Ge, M. Wu, J. Yang, Q. Wu, and Z. Jin. *Preparation and characterization of polymer/silica nanocomposites via double in situ miniemulsion polymerization*. Journal of Polymer Science Part A: Polymer Chemistry **48**(14), 3128 (2010).
- [34] N. G. Sahoo, S. Rana, J. W. Cho, L. Li, and S. H. Chan. *Polymer nanocomposites based on functionalized carbon nanotubes*. Progress in Polymer Science **35**(7), 837 (2010). [6](#)
- [35] T. Ramanathan, A. Abdala, S. Stankovich, D. Dikin, M. Herrera-Alonso, R. Piner, D. Adamson, H. Schniepp, X. Chen, R. Ruoff, *et al.* *Functionalized graphene sheets for polymer nanocomposites*. Nature Nanotechnology **3**(6), 327 (2008).
- [36] X. Lu, W. Zhang, C. Wang, T.-C. Wen, and Y. Wei. *One-dimensional conducting polymer nanocomposites: synthesis, properties and applications*. Progress in Polymer Science **36**(5), 671 (2011). [6](#)
- [37] L. E. Kreno, K. Leong, O. K. Farha, M. Allendorf, R. P. Van Duyne, and J. T. Hupp. *Metal-organic framework materials as chemical sensors*. Chemical Reviews **112**(2), 1105 (2011). [6](#)
- [38] J. K. Oh and J. M. Park. *Iron oxide-based superparamagnetic polymeric nanomaterials: design, preparation, and biomedical application*. Progress in Polymer Science **36**(1), 168 (2011). [6](#)
- [39] C. Lü and B. Yang. *High refractive index organic-inorganic nanocomposites: design, synthesis and application*. Journal of Materials Chemistry **19**(19), 2884 (2009). [7](#), [23](#)
- [40] J.-H. Kim, K. Park, H. Y. Nam, S. Lee, K. Kim, and I. C. Kwon. *Polymers for bioimaging*. Progress in Polymer Science **32**(8), 1031 (2007). [7](#), [24](#)
- [41] H. Yang, S. Zhu, and N. Pan. *Studying the mechanisms of titanium dioxide as ultraviolet-blocking additive for films and fabrics by an improved scheme*. Journal of Applied Polymer Science **92**(5), 3201 (2004). [7](#)
- [42] G. G. Yordanov, G. D. Gicheva, and C. D. Dushkin. *Optical memory based on photo-activated fluorescence of core/shell CdSe/CdS quantum dots embedded in poly (butylmethacrylate)*. Materials Chemistry and Physics **113**(2), 507 (2009). [7](#)

- [43] B. Rozenberg and R. Tenne. *Polymer-assisted fabrication of nanoparticles and nanocomposites*. Progress in Polymer Science **33**(1), 40 (2008). [8](#)
- [44] T. Hanemann and D. V. Szabó. *Polymer-nanoparticle composites: from synthesis to modern applications*. Materials **3**(6), 3468 (2010). [8](#)
- [45] H. Mataki, S. Yamaki, and T. Fukui. *Nanostructured organic/inorganic composites as transparent materials for optical components*. Japanese Journal of Applied Physics **43**(8S), 5819 (2004). [8](#)
- [46] C. Lü, Z. Cui, Y. Wang, Z. Li, C. Guan, B. Yang, and J. Shen. *Preparation and characterization of ZnS-polymer nanocomposite films with high refractive index*. Journal of Materials Chemistry **13**(9), 2189 (2003).
- [47] Y. Imai, A. Terahara, Y. Hakuta, K. Matsui, H. Hayashi, and N. Ueno. *Synthesis and characterization of high refractive index nanoparticle/poly (arylene ether ketone) nanocomposites*. Polymer Journal **42**(2), 179 (2010). [8](#)
- [48] H.-M. Xiong, Z.-D. Wang, D.-P. Liu, J.-S. Chen, Y.-G. Wang, and Y.-Y. Xia. *Bonding polyether onto ZnO nanoparticles: an effective method for preparing polymer nanocomposites with tunable luminescence and stable conductivity*. Advanced Functional Materials **15**(11), 1751 (2005).
- [49] K. Roy Choudhury, Y. Sahoo, and P. N. Prasad. *Hybrid quantum-dot-polymer nanocomposites for infrared photorefractivity at an optical communication wavelength*. Advanced Materials **17**(23), 2877 (2005). [8](#)
- [50] R. Elghanian, J. J. Storhoff, R. C. Mucic, R. L. Letsinger, and C. A. Mirkin. *Selective colorimetric detection of polynucleotides based on the distance-dependent optical properties of gold nanoparticles*. Science **277**(5329), 1078 (1997). [8](#)
- [51] D. Li and R. B. Kaner. *Shape and aggregation control of nanoparticles: not shaken, not stirred*. Journal of the American Chemical Society **128**(3), 968 (2006). [8](#)
- [52] C. Zeng and L. J. Lee. *Poly (methyl methacrylate) and polystyrene/clay nanocomposites prepared by in-situ polymerization*. Macromolecules **34**(12), 4098 (2001). [8](#)
- [53] D. Kim, J. S. Lee, C. M. Barry, and J. L. Mead. *Effect of fill factor and validation of characterizing the degree of mixing in polymer nanocomposites*. Polymer Engineering and Science **47**(12), 2049 (2007). [8](#)

- [54] S. K. Kumar, N. Jouault, B. Benicewicz, and T. Neely. *Nanocomposites with polymer grafted nanoparticles*. *Macromolecules* **46**(9), 3199 (2013). [8](#)
- [55] H. Zou, S. Wu, and J. Shen. *Polymer/silica nanocomposites: preparation, characterization, properties, and applications*. *Chemical Reviews* **108**(9), 3893 (2008). [8](#)
- [56] A. Yeniay, R. Gao, K. Takayama, R. Gao, and A. F. Garito. *Ultra-low-loss polymer waveguides*. *Journal of Lightwave Technology* **22**(1), 154 (2004). [9](#)
- [57] K. A. Gschneidner and J. Capellen. *1787-1987, Two hundred years of rare earths* (Rare-earth Information Center, 1987). [9](#)
- [58] F. Szabadváry. *Handbook of the chemistry and physics of the rare earths vol. 11* (Amsterdam, Netherlands, 1998). [10](#)
- [59] D. R. Lide. *CRC handbook of chemistry and physics* (Florida, CRC press, 2004). [10](#)
- [60] N. Bloembergen. *Solid state infrared quantum counters*. *Physical Review Letters* **2**(3), 84 (1959). [10](#)
- [61] C. J. Koester and E. Snitzer. *Amplification in a fiber laser*. *Applied Optics* **3**(10), 1182 (1964). [10](#)
- [62] J. P. Dakin and R. G. Brown. *Handbook of optoelectronics (two-volume set)* (Florida, CRC Press, 2006). [10](#)
- [63] R. J. Mears, L. Reekie, S. Poole, and D. N. Payne. *Neodymium-doped silica single-mode fibre lasers*. *Electronics Letters* **21**(17), 738 (1985). [10](#)
- [64] R. J. Mears, L. Reekie, I. Jauncey, and D. N. Payne. *Low-noise erbium-doped fibre amplifier operating at 1.54  $\mu\text{m}$* . *Electronics Letters* **23**(19), 1026 (1987). [10](#)
- [65] S. E. Miller. *Integrated optics: an introduction*. *Bell System Technical Journal* **48**(7), 2059 (1969). [10](#)
- [66] H. Yajima, S. Kawase, and Y. Sekimoto. *Amplification at 1.06  $\mu\text{m}$  using a Nd: glass thin-film waveguide*. *Applied Physics Letters* **21**(9), 407 (1972). [10](#)
- [67] T. Kitagawa, K. Hattori, M. Shimizu, Y. Ohmori, and M. Kobayashi. *Guided-wave laser based on erbium-doped silica planar lightwave circuit*. *Electronics Letters* **27**(4), 334 (1991). [11](#)



- [68] T. Kitagawa, K. Hattori, K. Shuto, M. Yasu, M. Kobayashi, and M. Horiguchi. *Amplification in erbium-doped silica-based planar lightwave circuits*. Electronics Letters **28**(19), 1818 (1992).
- [69] J. Shmulovich, Y. Wong, P. Becker, A. Bruce, R. Adar, and A. Wong. *Er<sup>3+</sup> glass waveguide amplifier at 1.5  $\mu$ m on silicon*. Electronics Letters **28**(13), 1181 (1992). [11](#)
- [70] R. Paschotta, J. Nilsson, A. C. Tropper, and D. C. Hanna. *Ytterbium-doped fibre amplifiers*. IEEE Journal of Quantum Electronics **33**(7), 1049 (1997). [12](#)
- [71] J. Palm, F. Gan, B. Zheng, J. Michel, and L. Kimerling. *Electroluminescence of erbium-doped silicon*. Physical Review B **54**(24), 17603 (1996). [12](#)
- [72] P. Reece, M. Gal, H. Tan, and C. Jagadish. *Optical properties of erbium-implanted porous silicon microcavities*. Applied Physics Letters **85**(16), 3363 (2004). [12](#)
- [73] S.-Y. Chen, W.-F. Hsieh, and C.-C. Ting. *Titanium dioxide film co-doped with yttrium and erbium and method for producing the same* (2003). US Patent 6,602,338. [12](#)
- [74] R. Dahal, C. Ugolini, J. Lin, H. Jiang, and J. Zavada. *Erbium-doped GaN optical amplifiers operating at 1.54  $\mu$ m*. Applied Physics Letters **95**(11), 111109 (2009). [12](#)
- [75] P. Whitney, K. Uwai, H. Nakagome, and K. Takahei. *Erbium-doped GaAs light-emitting diodes emitting erbium f-shell luminescence at 1.54  $\mu$ m*. Electronics Letters **24**(12), 740 (1988). [12](#)
- [76] T.-Y. Tsai, Y.-C. Fang, H.-X. Tsao, S.-T. Lin, and C. Hu. *Passively cascade-pulsed erbium zblan all-fiber laser*. Optics Express **20**(12), 12787 (2012). [12](#)
- [77] A. Jha, S. Shen, and M. Naftaly. *Structural origin of spectral broadening of 1.5- $\mu$ m emission in Er<sup>3+</sup>-doped tellurite glasses*. Physical Review B **62**(10), 6215 (2000). [12](#)
- [78] K. Shuto, K. Hattori, T. Kitagawa, Y. Ohmori, and M. Horiguchi. *Erbium-doped phosphosilicate glass waveguide amplifier fabricated by pecvd*. Electronics Letters **29**(2), 139 (1993). [12](#)

- [79] G. Van den Hoven, R. Koper, A. Polman, C. Van Dam, J. Van Uffelen, and M. Smit. *Net optical gain at 1.53  $\mu\text{m}$  in Er-doped  $\text{Al}_2\text{O}_3$  waveguides on silicon*. Applied Physics Letters **68**(14), 1886 (1996). [12](#)
- [80] R. Brinkmann, W. Sohler, and H. Suche. *Continuous-wave erbium-diffused  $\text{LiNbO}_3$  waveguide laser*. Electronics Letters **27**(5), 415 (1991). [12](#)
- [81] J. Zhou, W. Zhang, T. Huang, L. Wang, J. Li, W. Liu, B. Jiang, Y. Pan, and J. Guo. *Optical properties of Er, Yb co-doped YAG transparent ceramics*. Ceramics International **37**(2), 513 (2011). [12](#)
- [82] S. Liu, X. Guo, X. Zhai, D. Zhao, K. Zheng, G. Qin, and W. Qin. *Oleic acid-modified  $\text{LiYF}_4$ : Er, Yb nanocrystals for potential optical-amplification applications*. Journal of Nanoscience and Nanotechnology **14**(5), 3718 (2014). [12](#)
- [83] X. Zhai, S. Liu, X. Liu, F. Wang, D. Zhang, G. Qin, and W. Qin. *Sub-10 nm  $\text{BaYF}_5$ :  $\text{Yb}^{3+}$ ,  $\text{Er}^{3+}$  core-shell nanoparticles with intense 1.53  $\mu\text{m}$  fluorescence for polymer-based waveguide amplifiers*. Journal of Materials Chemistry C **1**(7), 1525 (2013). [12](#)
- [84] X. Zhai, J. Li, S. Liu, X. Liu, D. Zhao, F. Wang, D. Zhang, G. Qin, and W. Qin. *Enhancement of 1.53  $\mu\text{m}$  emission band in  $\text{NaYF}_4$ :  $\text{Er}^{3+}$ ,  $\text{Yb}^{3+}$ ,  $\text{Ce}^{3+}$  nanocrystals for polymer-based optical waveguide amplifiers*. Optical Materials Express **3**(2), 270 (2013). [12](#), [40](#)
- [85] G.-S. Yi and G.-M. Chow. *Water-soluble  $\text{NaYF}_4$ : Yb, Er (Tm)/ $\text{NaYF}_4$ /polymer core/shell/shell nanoparticles with significant enhancement of upconversion fluorescence*. Chemistry of Materials **19**(3), 341 (2007). [12](#)
- [86] V. M. Lojpur, P. S. Ahrenkiel, and M. D. Dramićanin. *Color-tunable up-conversion emission in  $\text{Y}_2\text{O}_3$ :  $\text{Yb}^{3+}$ ,  $\text{Er}^{3+}$  nanoparticles prepared by polymer complex solution method*. Nanoscale Research Letters **8**(1), 1 (2013). [12](#)
- [87] D. Zhang, C. Chen, C. Chen, C. Ma, D. Zhang, S. Bo, and Z. Zhen. *Optical gain at 1535 nm in  $\text{LaF}_3$ : Er, Yb nanoparticle-doped organic-inorganic hybrid material waveguide*. Applied Physics Letters **91**(16), 1109 (2007). [12](#), [40](#)
- [88] J. S. Chang, K. Suh, M.-S. Yang, and J. H. Shin. *Development and application of Er doped silicon-rich silicon nitrides and Er silicates for on-chip light sources*. Silicon Photonics II, Topics in Applied Physics **119**, 95 (2011). [11](#), [39](#)

- [89] X. Orignac, D. Barbier, X. M. Du, R. M. Almeida, O. McCarthy, and E. Yeatman. *Sol-gel silica/titania-on-silicon Er/Yb-doped waveguides for optical amplification at 1.5  $\mu\text{m}$* . Optical Materials **12**(1), 1 (1999).
- [90] F. D. Pasquale and M. Federighi. *Improved gain characteristics in high-concentration  $\text{Er}^{3+}/\text{Yb}^{3+}$  codoped glass waveguide amplifiers*. IEEE Journal of Quantum Electronics **30**(9), 2127 (1994).
- [91] V. Nazabal, P. N mec, A.-M. Jurduc, S. Zhang, F. Charpentier, H. Lhermite, J. Charrier, J.-P. Guin, A. Mor ac, M. Frumar, *et al.* *Optical waveguide based on amorphous  $\text{Er}^{3+}$ -doped Ga-Ge-Sb-S(Se) pulsed laser deposited thin films*. Thin Solid Films **518**(17), 4941 (2010).
- [92] A. Caricato, A. Fazzi, A. Jha, A. Kar, G. Leggieri, A. Luches, M. Martino, F. Romano, S. Shen, M. Taghizadeh, *et al.* *Er-doped oxyfluoride silicate thin films prepared by pulsed laser deposition*. Optical Materials **29**(9), 1166 (2007).
- [93] A. Mori, Y. Ohishi, and S. Sudo. *Erbium-doped tellurite glass fibre laser and amplifier*. Electronics Letters **33**(10), 863 (1997). [11](#)
- [94] G. Kumar, C. Chen, R. Riman, S. Chen, D. Smith, and J. Ballato. *Optical properties of a transparent  $\text{CaF}_2$ :  $\text{Er}^{3+}$  fluoropolymer nanocomposite*. Applied Physics Letters **86**(24), 241105 (2005). [11](#)
- [95] R. Dekker, D. Klunder, A. Borreman, M. Diemeer, K. Worhoff, A. Driessen, J. Stouwdam, and F. Van Veggel. *Stimulated emission and optical gain in  $\text{LaF}_3$ : Nd nanoparticle-doped polymer-based waveguides*. Applied Physics Letters **85**(25), 6104 (2004). [40](#)
- [96] W. Wong, K. Chan, and E. Pun. *Ultraviolet direct printing of rare-earth-doped polymer waveguide amplifiers*. Applied Physics Letters **87**(1) (2005). [40](#)
- [97] R. Ferreira, P. Andr , and L. Carlos. *Organic-inorganic hybrid materials towards passive and active architectures for the next generation of optical networks*. Optical Materials **32**(11), 1397 (2010). [11](#), [40](#)
- [98] J. Lawrence, G. Turnbull, and I. Samuel. *Broadband optical amplifier based on a conjugated polymer*. Applied Physics Letters **80**(17), 3036 (2002). [11](#)
- [99] H. Rubens and B. W. Snow. *II. on the refraction of rays of great wave-length in rock-salt, sylvite, and fluorite*. The London, Edinburgh, and Dublin Philosophical Magazine and Journal of Science **35**(212), 35 (1893). [13](#)

- 
- [100] H. Gebbie, N. Stone, and F. Findlay. *A stimulated emission source at 0.34 millimetre wave-length*. Nature **202**, 685 (1964). [13](#)
- [101] T. Hartwick, D. Hodges, D. Barker, and F. Foote. *Far infrared imagery*. Applied Optics **15**(8), 1919 (1976). [13](#)
- [102] G. Mourou, C. Stancampiano, A. Antonetti, and A. Orszag. *Picosecond microwave pulses generated with a subpicosecond laser-driven semiconductor switch*. Applied Physics Letters **39**(4), 295 (1981). [14](#)
- [103] D. Auston, K. Cheung, J. Valdmanis, and D. Kleinman. *Cherenkov radiation from femtosecond optical pulses in electro-optic media*. Physical Review Letters **53**(16), 1555 (1984). [14](#)
- [104] A. Nahata, D. H. Auston, T. F. Heinz, and C. Wu. *Coherent detection of freely propagating terahertz radiation by electro-optic sampling*. Applied Physics Letters **68**(2), 150 (1996). [14](#)
- [105] K. Yang, P. Richards, and Y. Shen. *Generation of far-infrared radiation by picosecond light pulses in LiNbO<sub>3</sub>*. Applied Physics Letters **19**(9), 320 (1971). [15](#)
- [106] K. Yeh, M. Hoffmann, J. Hebling, and K. A. Nelson. *Generation of 10 J ultrashort terahertz pulses by optical rectification*. Applied Physics Letters **90**(171121), 1 (2007). [15](#)
- [107] J. Dai, X. Xie, and X.-C. Zhang. *Detection of broadband terahertz waves with a laser-induced plasma in gases*. Physical Review Letters **97**(10), 103903 (2006). [15](#)
- [108] J. Dai, J. Liu, and X.-C. Zhang. *Terahertz wave air photonics: terahertz wave generation and detection with laser-induced gas plasma*. Selected Topics in Quantum Electronics, IEEE Journal of **17**(1), 183 (2011). [15](#)
- [109] M. Clerici, D. Faccio, L. Caspani, M. Peccianti, E. Rubino, L. Razzari, F. Légaré, T. Ozaki, and R. Morandotti. *CCD-based imaging and 3D space-time mapping of terahertz fields via Kerr frequency conversion*. Optics Letters **38**(11), 1899 (2013). [15](#)
- [110] J. Zhang. *Polarization-dependent study of THz air-biased coherent detection*. Optics Letters **39**(14), 4096 (2014). [15](#)

- [111] W. L. Chan, J. Deibel, and D. M. Mittleman. *Imaging with terahertz radiation*. Reports on Progress in Physics **70**(8), 1325 (2007). [16](#)
- [112] S. Koenig, D. Lopez-Diaz, J. Antes, F. Boes, R. Henneberger, A. Leuther, A. Tessmann, R. Schmogrow, D. Hillerkuss, R. Palmer, *et al.* *Wireless sub-THz communication system with high data rate*. Nature Photonics **7**(12), 977 (2013). [16](#)
- [113] N. Ghosh, A. Pradhan, P. K. Gupta, S. Gupta, V. Jaiswal, and R. Singh. *Depolarization of light in a multiply scattering medium: effect of the refractive index of a scatterer*. Physical Review E **70**(6), 066607 (2004). [17](#), [60](#), [94](#)
- [114] M. Nixon, O. Katz, E. Small, Y. Bromberg, A. A. Friesem, Y. Silberberg, and N. Davidson. *Real-time wavefront shaping through scattering media by all-optical feedback*. Nature Photonics **7**(11), 919 (2013).
- [115] A. P. Mosk, A. Lagendijk, G. Lerosey, and M. Fink. *Controlling waves in space and time for imaging and focusing in complex media*. Nature Photonics **6**(5), 283 (2012).
- [116] B. Redding, S. F. Liew, R. Sarma, and H. Cao. *Compact spectrometer based on a disordered photonic chip*. Nature Photonics **7**(9), 746 (2013). [17](#)
- [117] S. Tseng, A. Tafflove, D. Maitland, V. Backman, J. Walsh Jr, *et al.* *Investigation of the noise-like structures of the total scattering cross-section of random media*. Optics Express **13**(16), 6127 (2005). [17](#)
- [118] P. M. Johnson, B. P. Bret, J. G. Rivas, J. J. Kelly, and A. Lagendijk. *Anisotropic diffusion of light in a strongly scattering material*. Physical Review Letters **89**(24), 243901 (2002). [59](#)
- [119] M. Kaushik, B. W.-H. Ng, B. M. Fischer, and D. Abbott. *Terahertz scattering by two phased media with optically soft scatterers*. Journal of Applied Physics **112**(11), 113112 (2012). [17](#), [59](#), [60](#)
- [120] D. S. Wiersma. *The physics and applications of random lasers*. Nature Physics **4**(5), 359 (2008). [17](#)
- [121] Y. Guan, O. Katz, E. Small, J. Zhou, and Y. Silberberg. *Polarization control of multiply scattered light through random media by wavefront shaping*. Optics Letters **37**(22), 4663 (2012). [17](#), [99](#)

- [122] X. Guo, M. F. Wood, N. Ghosh, and I. A. Vitkin. *Depolarization of light in turbid media: a scattering event resolved Monte Carlo study*. Applied Optics **49**(2), 153 (2010). [19](#)
- [123] G. Jarry, E. Steimer, V. Damaschini, M. Epifanie, M. Jurczak, and R. Kaiser. *Coherence and polarization of light propagating through scattering media and biological tissues*. Applied Optics **37**(31), 7357 (1998). [19](#)
- [124] A. Chatterjee. *Properties improvement of PMMA using nano TiO<sub>2</sub>*. Journal of Applied Polymer Science **118**(5), 2890 (2010). [23](#), [24](#)
- [125] G. E. Town, R. M. Chaplin, M. J. Withford, and D. Baer. *Randomly microstructured polymer optical fibre*. In *ACOFT/AOS 2006-Australian Conference on Optical Fibre Technology/Australian Optical Society* (2006). [23](#)
- [126] W. Zhuang, T. Hayashi, and S. Mukamel. *Coherent multidimensional vibrational spectroscopy of biomolecules: concepts, simulations, and challenges*. Angewandte Chemie International Edition **48**(21), 3750 (2009). [24](#)
- [127] C.-H. Lee and W.-C. Chen. *Synthesis and optical characteristics of trialkoxy-capped poly (methyl methacrylate)-silica hybrid films*. Tamkang Journal of Science and Engineering **6**(2), 73 (2003). [24](#)
- [128] M. Born and E. Wolf. *Principles of optics: electromagnetic theory of propagation, interference and diffraction of light* (London, Cambridge University Press, 1999). [25](#), [99](#)
- [129] C. F. Bohren and D. R. Huffman. *Absorption and scattering of light by small particles* (Weinheim, Germany, John Wiley & Sons, 2008). [25](#), [46](#)
- [130] H. C. Hulst and H. Van De Hulst. *Light scattering by small particles* (New York, Wiley, 1957). [25](#)
- [131] M. Quinten. *Optical properties of nanoparticle systems: Mie and beyond* (Weinheim, Germany, John Wiley & Sons, 2010). [26](#)
- [132] D. S. Wiersma, P. Bartolini, A. Lagendijk, and R. Righini. *Localization of light in a disordered medium*. Nature **390**(6661), 671 (1997). [27](#)
- [133] P. Robinson. *Wave propagation in disordered media*. Philosophical Magazine B **80**(12), 2087 (2000).

- [134] A. Ishimaru. *Wave propagation and scattering in random media*, vol. 2 (New York, Academic Press, 1978). [91](#)
- [135] X. Li, D. N. Pattanayak, T. Durduran, J. P. Culver, B. Chance, and A. G. Yodh. *Near-field diffraction tomography with diffuse photon density waves*. *Physical Review E* **61**(4), 4295 (2000). [27](#)
- [136] R. Graaff and J. Ten Bosch. *Diffusion coefficient in photon diffusion theory*. *Optics Letters* **25**(1), 43 (2000). [27](#)
- [137] M. B. van der Mark. *Propagation of light in disordered media: a search for Anderson localization*. Ph.D. Thesis, University of Amsterdam, Netherlands (1990). [27](#)
- [138] M. v. van Rossum and T. M. Nieuwenhuizen. *Multiple scattering of classical waves: Microscopy, mesoscopy, and diffusion*. *Reviews of Modern Physics* **71**(1), 313 (1999). [29](#)
- [139] G. A. Niklasson, C. Granqvist, and O. Hunderi. *Effective medium models for the optical properties of inhomogeneous materials*. *Applied Optics* **20**(1), 26 (1981). [29](#)
- [140] D. I. Johnson and G. E. Town. *Refractive index and thermo-optic coefficient of composite polymers at 1.55  $\mu\text{m}$* . In *Microelectronics, MEMS, and Nanotechnology*, pp. 603821–603821 (International Society for Optics and Photonics, 2005). [31](#)
- [141] J. L. H. Chau, Y.-M. Lin, A.-K. Li, W.-F. Su, K.-S. Chang, S. L.-C. Hsu, and T.-L. Li. *Transparent high refractive index nanocomposite thin films*. *Materials Letters* **61**(14), 2908 (2007). [33](#)
- [142] Q. Chen, L. S. Schadler, R. W. Siegel, and G. C. Irvin Jr. *ZnO/PMMA thin film nanocomposites for optical coatings*. In *Optical Science and Technology, SPIE's 48th Annual Meeting*, pp. 158–162 (International Society for Optics and Photonics, 2003). [33](#)
- [143] Q. Chen, L. S. Schadler, R. W. Siegel, and G. C. Irvin Jr. *ZnO/PMMA thin film nanocomposites for optical coatings*. In *Optical Science and Technology, SPIE's 48th Annual Meeting*, pp. 158–162 (International Society for Optics and Photonics, 2003). [34](#)



- [144] J. L. H. Chau, Y.-M. Lin, A.-K. Li, W.-F. Su, K.-S. Chang, S. L.-C. Hsu, and T.-L. Li. *Transparent high refractive index nanocomposite thin films*. Materials Letters **61**(14), 2908 (2007). [34](#)
- [145] A. H. Yuwono, J. Xue, J. Wang, H. I. Elim, W. Ji, Y. Li, and T. J. White. *Transparent nanohybrids of nanocrystalline  $\text{TiO}_2$  in PMMA with unique nonlinear optical behavior*. Journal of Materials Chemistry **13**(6), 1475 (2003). [35](#)
- [146] J. Clark and G. Lanzani. *Organic photonics for communications*. Nature Photonics **4**(7), 438 (2010). [39](#)
- [147] Y. Yunlong, S. Zhifa, C. Daqin, H. Ping, L. Hang, and W. Yuansheng. *Improving  $\text{Er}^{3+}$  1.53  $\mu\text{m}$  luminescence by  $\text{CeF}_3$  nanocrystallization in aluminosilicate glass*. Journal of Applied Physics **108**(12) (2010). [39](#)
- [148] D. Chen, Y. Wang, Y. Yu, E. Ma, F. Bao, Z. Hu, and Y. Cheng. *Luminescence at 1.53  $\mu\text{m}$  for a new  $\text{Er}^{3+}$ -doped transparent oxyfluoride glass ceramic*. Materials Research Bulletin **41**(6), 1112 (2006).
- [149] A. Kenyon. *Recent developments in rare-earth doped materials for optoelectronics*. Progress in Quantum Electronics **26**(4), 225 (2002). [39](#), [40](#)
- [150] L. Slooff, A. Polman, M. O. Wolbers, F. Van Veggel, D. Reinhoudt, and J. Hofstraet. *Optical properties of erbium-doped organic polydentate cage complexes*. Journal of Applied Physics **83**(1), 497 (1998). [40](#)
- [151] P. Etienne, P. Coudray, J. Porque, and Y. Moreau. *Active erbium-doped organic-inorganic waveguide*. Optics Communications **174**(5), 413 (2000). [40](#)
- [152] S. Bo, J. Wang, H. Zhao, H. Ren, Q. Wang, G. Xu, X. Zhang, X. Liu, and Z. Zhen.  *$\text{LaF}_3$ : Er, Yb doped sol-gel polymeric optical waveguide amplifiers*. Applied Physics B **91**(1), 79 (2008). [40](#)
- [153] C. Chen, D. Zhang, T. Li, D. Zhang, L. Song, and Z. Zhen. *Erbium-ytterbium codoped waveguide amplifier fabricated with solution-processable complex*. Applied Physics Letters **94**(4), 041119 (2009). [40](#)
- [154] W. Wong, E. Pun, and K. Chan.  *$\text{Er}^{3+}$ - $\text{Yb}^{3+}$  codoped polymeric optical waveguide amplifiers*. Applied Physics Letters **84**, 176 (2004). [40](#)



- [155] G. Kumar, C. Chen, J. Ballato, and R. Riman. *Optical characterization of infrared emitting rare-earth-doped fluoride nanocrystals and their transparent nanocomposites*. Chemistry of Materials **19**(6), 1523 (2007). [40](#)
- [156] S. Bo, J. Hu, Z. Chen, Q. Wang, G. Xu, X. Liu, and Z. Zhen. *Core-shell  $\text{LaF}_3$ : Er, Yb nanocrystal doped sol-gel materials as waveguide amplifiers*. Applied Physics B **97**(3), 665 (2009).
- [157] K.-L. Lei, C.-F. Chow, K.-C. Tsang, E. N. Lei, V. Roy, M. H. Lam, C. S. Lee, E. Pun, and J. Li. *Long aliphatic chain coated rare-earth nanocrystal as polymer-based optical waveguide amplifiers*. Journal of Materials Chemistry **20**(35), 7526 (2010).
- [158] J. Wang, J. Hu, D. Tang, X. Liu, and Z. Zhen. *Oleic acid (OA)-modified  $\text{LaF}_3$ : Er, Yb nanocrystals and their polymer hybrid materials for potential optical-amplification applications*. Journal of Materials Chemistry **17**(16), 1597 (2007). [40](#)
- [159] E. Desurvire, C. R. Giles, J. R. Simpson, and J. L. Zyskind. *Erbium-doped fiber amplifier* (1991). US Patent 5,005,175. [41](#)
- [160] B. Judd. *Optical absorption intensities of rare-earth ions*. Physical Review **127**(3), 750 (1962). [43](#)
- [161] G. Ofelt. *Intensities of crystal spectra of rare-earth ions*. The Journal of Chemical Physics **37**(3), 511 (1962). [43](#)
- [162] T. Schweizer. *Rare-earth-doped gallium lanthanum sulphide glasses for mid-infrared fibre lasers*. Ph.D. thesis, University of Southampton, Faculty of Engineering and Applied Science, United Kingdom (2000). [43](#)
- [163] Z. Zhao. *Pulsed laser deposition and characterisation of rare earth doped glass-polymer optical materials*. Ph.D. thesis, University of Leeds, School of Process, Environmental and Materials Engineering, United Kingdom (2012). [43](#)
- [164] M. J. Weber. *Probabilities for radiative and nonradiative decay of  $\text{Er}^{3+}$  in  $\text{LaF}_3$* . Physical Review **157**(2), 262 (1967). [43](#)
- [165] W. Carnall, P. Fields, and K. Rajnak. *Electronic energy levels in the trivalent lanthanide aquo ions. I.  $\text{Pr}^{3+}$ ,  $\text{Nd}^{3+}$ ,  $\text{Pm}^{3+}$ ,  $\text{Sm}^{3+}$ ,  $\text{Dy}^{3+}$ ,  $\text{Ho}^{3+}$ ,  $\text{Er}^{3+}$ , and  $\text{Tm}^{3+}$* . The Journal of Chemical Physics **49**(10), 4424 (1968). [43](#)

- [166] M. Federighi and F. D. Pasquale. *The effect of pair-induced energy transfer on the performance of silica waveguide amplifiers with high  $Er^{3+}/Yb^{3+}$  concentrations*. IEEE Photonics Technology Letters **7**(3), 303 (1995). 48
- [167] E. Yahel and A. Hardy. *Modeling high-power  $Er^{3+}$ - $Yb^{3+}$  codoped fiber lasers*. Journal of Lightwave Technology **21**(9), 2044 (2003).
- [168] J. Li, K. Duan, Y. Wang, W. Zhao, Y. Guo, and X. Lin. *Modeling and optimizing of high-concentration erbium-doped fiber amplifiers with consideration of ion-clusters*. Optics Communications **277**(1), 143 (2007).
- [169] Y. Hu, S. Jiang, G. Sorbello, T. Luo, Y. Ding, B.-C. Hwang, J.-H. Kim, H.-J. Seo, and N. Peyghambarian. *Numerical analyses of the population dynamics and determination of the upconversion coefficients in a new high erbium-doped tellurite glass*. Journal of the Optical Society of America B **18**(12), 1928 (2001). 48
- [170] C. Jiang and Q. Zeng. *Optimization of erbium-doped waveguide amplifier*. Optics & Laser Technology **36**(2), 167 (2004). 48
- [171] A. Shooshtari, T. Touam, and S. I. Najafi.  *$Yb^{3+}$ -sensitized  $Er^{3+}$ -doped waveguide amplifiers: a theoretical approach* (1998). 48
- [172] Kigre. *MM-2 and QX/ErSP*. URL <http://www.kigre.com/glass.html>. 50, 54
- [173] M. Xu and R. Alfano. *Random walk of polarized light in turbid media*. Physical Review Letters **95**(21), 213901 (2005). 59, 60, 94
- [174] M. B. Van Der Mark, M. P. van Albada, and A. Lagendijk. *Light scattering in strongly scattering media: Multiple scattering and weak localization*. Physical Review B **37**(7), 3575 (1988). 59
- [175] J. Fletcher, G. Swift, J. Levitt, J. Chamberlain, et al. *Propagation of terahertz radiation through random structures: an alternative theoretical approach and experimental validation*. Journal of Applied Physics **101**(1), 013102 (2007). 59, 60
- [176] S. Mujumdar, K. Chau, and A. Elezzabi. *Experimental and numerical investigation of terahertz transmission through strongly scattering sub-wavelength size spheres*. Applied Physics Letters **85**(25), 6284 (2004). 59

- [177] D. Bicout, C. Brosseau, A. Martinez, and J. Schmitt. *Depolarization of multiply scattered waves by spherical diffusers: influence of the size parameter*. Physical Review E **49**(2), 1767 (1994). [60](#), [92](#)
- [178] I. M. Stockford, S. P. Morgan, P. Chang, and J. G. Walker. *Analysis of the spatial distribution of polarized light backscattered from layered scattering media*. Journal of Biomedical Optics **7**(3), 313 (2002). [60](#)
- [179] B. Wilson and G. Adam. *A Monte Carlo model for the absorption and flux distributions of light in tissue*. Medical Physics **10**(6), 824 (1983). [60](#)
- [180] L. Wang, S. L. Jacques, and L. Zheng. *MCML—Monte Carlo modeling of light transport in multi-layered tissues*. Computer Methods and Programs in Biomedicine **47**(2), 131 (1995). [60](#)
- [181] J. Pearce and D. M. Mittleman. *Using terahertz pulses to study light scattering*. Physica B: Condensed Matter **338**(1), 92 (2003). [60](#)
- [182] J. Pearce and D. M. Mittleman. *Scale model experimentation: Using terahertz pulses to study light scattering*. Physics in Medicine and Biology **47**(21), 3823 (2002).
- [183] J. Pearce and D. M. Mittleman. *Propagation of single-cycle terahertz pulses in random media*. Optics Letters **26**(24), 2002 (2001).
- [184] O. Katz, E. Small, Y. Bromberg, and Y. Silberberg. *Focusing and compression of ultrashort pulses through scattering media*. Nature Photonics **5**(6), 372 (2011). [60](#)
- [185] J. Pearce, Z. Jian, and D. M. Mittleman. *Statistics of multiply scattered broadband terahertz pulses*. Physical Review Letters **91**(4), 043903 (2003). [60](#)
- [186] C. Jansen, S. Priebe, C. Möller, M. Jacob, H. Dierke, M. Koch, and T. Kürner. *Diffuse scattering from rough surfaces in THz communication channels*. IEEE Transactions on Terahertz Science and Technology **1**(2), 462 (2011). [60](#)
- [187] S. Priebe and T. Kurner. *Stochastic modeling of THz indoor radio channels*. IEEE Transactions on Wireless Communications **12**(9), 4445 (2013). [60](#)
- [188] S. Schecklman, L. M. Zurk, S. Henry, and G. P. Kniffin. *Terahertz material detection from diffuse surface scattering*. Journal of Applied Physics **109**(9), 094902 (2011).

- [189] R. Piesiewicz, C. Jansen, D. Mittleman, T. Kleine-Ostmann, M. Koch, and T. Kürner. *Scattering analysis for the modeling of THz communication systems*. IEEE Transactions on Antennas and Propagation **55**(11), 3002 (2007). [60](#)
- [190] J. Aulbach, B. Gjonaj, P. M. Johnson, A. P. Mosk, and A. Lagendijk. *Control of light transmission through opaque scattering media in space and time*. Physical Review Letters **106**(10), 103901 (2011). [60](#)
- [191] S. A. Prahl, M. J. van Gemert, and A. J. Welch. *Determining the optical properties of turbid media by using the adding–doubling method*. Applied Optics **32**(4), 559 (1993). [63](#)
- [192] M. H. Niemz. *Laser-tissue interactions: fundamentals and applications* (Berlin, Germany, Springer Science & Business Media, 2013). [63](#)
- [193] P. U. Jepsen and B. M. Fischer. *Dynamic range in terahertz time-domain transmission and reflection spectroscopy*. Optics Letters **30**(1), 29 (2005). [72](#)
- [194] J. Schäfer, S.-C. Lee, and A. Kienle. *Calculation of the near fields for the scattering of electromagnetic waves by multiple infinite cylinders at perpendicular incidence*. Journal of Quantitative Spectroscopy and Radiative Transfer **113**(16), 2113 (2012). [80](#), [135](#), [136](#)
- [195] D. M. Mittleman, S. Hunsche, L. Boivin, and M. C. Nuss. *T-ray tomography*. Optics Letters **22**(12), 904 (1997). [91](#)
- [196] D. M. Mittleman, R. H. Jacobsen, R. Neelamani, R. G. Baraniuk, and M. C. Nuss. *Gas sensing using terahertz time-domain spectroscopy*. Applied Physics B: Lasers and Optics **67**(3), 379 (1998).
- [197] P. H. Siegel. *Terahertz technology in biology and medicine*. In *Microwave Symposium Digest, 2004 IEEE MTT-S International*, vol. 3, pp. 1575–1578 (IEEE, 2004). [91](#)
- [198] P. Han, M. Tani, M. Usami, S. Kono, R. Kersting, and X.-C. Zhang. *A direct comparison between terahertz time-domain spectroscopy and far-infrared Fourier transform spectroscopy*. Journal of Applied Physics **89**(4), 2357 (2001). [91](#)
- [199] R. M. Smith and M. A. Arnold. *Terahertz time-domain spectroscopy of solid samples: principles, applications, and challenges*. Applied Spectroscopy Reviews **46**(8), 636 (2011). [91](#)

- [200] F. MacKintosh, J. Zhu, D. Pine, and D. Weitz. *Polarization memory of multiply scattered light*. Physical Review B **40**(13), 9342 (1989). [91](#), [108](#)
- [201] A. Chabanov and A. Genack. *Field distributions in the crossover from ballistic to diffusive wave propagation*. Physical Review E **56**(2), R1338 (1997). [92](#)
- [202] Z. Zhang, I. Jones, H. Schriemer, J. Page, D. Weitz, and P. Sheng. *Wave transport in random media: The ballistic to diffusive transition*. Physical Review E **60**(4), 4843 (1999). [92](#)
- [203] A. H. Hielscher, J. R. Mourant, and I. J. Bigio. *Influence of particle size and concentration on the diffuse backscattering of polarized light from tissue phantoms and biological cell suspensions*. Applied Optics **36**(1), 125 (1997). [96](#)
- [204] S. Morgan and M. Ridgway. *Polarization properties of light backscattered from a two layer scattering medium*. Optics Express **7**(12), 395 (2000). [96](#)
- [205] B. Kaplan, G. Ledanois, and B. Dré villon. *Mueller matrix of dense polystyrene latex sphere suspensions: measurements and Monte Carlo simulation*. Applied Optics **40**(16), 2769 (2001).
- [206] J. Ramella-Roman, S. Prahl, and S. Jacques. *Three Monte Carlo programs of polarized light transport into scattering media: Part I*. Optics Express **13**(12), 4420 (2005).
- [207] T. Yun, N. Zeng, W. Li, D. Li, X. Jiang, and H. Ma. *Monte Carlo simulation of polarized photon scattering in anisotropic media*. Optics Express **17**(19), 16590 (2009). [96](#), [104](#)
- [208] S. G. Adie, T. R. Hillman, and D. D. Sampson. *Detection of multiple scattering in optical coherence tomography using the spatial distribution of Stokes vectors*. Optics Express **15**(26), 18033 (2007). [96](#)
- [209] X. Wang and L. V. Wang. *Propagation of polarized light in birefringent turbid media: A Monte Carlo study*. Journal of Biomedical Optics **7**(3), 279 (2002).
- [210] X. Guo, M. F. Wood, and I. A. Vitkin. *Stokes polarimetry in multiply scattering chiral media: effects of experimental geometry*. Applied Optics **46**(20), 4491 (2007). [96](#)
- [211] M. Xu and R. Alfano. *Circular polarization memory of light*. Physical Review E **72**(6), 065601 (2005). [99](#)

- 
- [212] C. Macdonald and I. Meglinski. *Backscattering of circular polarized light from a disperse random medium influenced by optical clearing*. Laser Physics Letters **8**(4), 324 (2011). [104](#)
- [213] E. Small, O. Katz, Y. Guan, and Y. Silberberg. *Spectral control of broadband light through random media by wavefront shaping*. Optics Letters **37**(16), 3429 (2012). [99](#), [104](#)
- [214] J. Sorrentini, M. Zerrad, G. Soriano, and C. Amra. *Enpolarization of light by scattering media*. Optics Express **19**(22), 21313 (2011). [121](#)
- [215] H. Zhang, C. Li, J. Guo, L. Zang, and J. Luo. *In situ synthesis of poly (methyl methacrylate)/SiO<sub>2</sub> hybrid nanocomposites via Grafting Onto strategy based on UV irradiation in the presence of iron aqueous solution*. Journal of Nanomaterials **2012**, 3 (2012). [127](#)